UNIVERSITY OF CALGARY

SiPM-based Fiber Photometry and EIS for Cortisol Detection:

Common Electronics, Distinct Applications

by

Mahrokh Namazi

A THESIS
SUBMITTED TO THE FACULTY OF GRADUATE STUDIES
IN PARTIAL FULFILLMENT OF THE REQUIREMENTS FOR THE
DEGREE OF MASTER OF SCIENCE

GRADUATE PROGRAM IN ELECTRICAL ENGINEERING

CALGARY, ALBERTA
JANUARY, 2024

Abstract

This thesis introduces two biomedical measurement systems utilizing the AD5934 impedance converter: a silicon photomultiplier (SiPM)-based low-light fiber photometry system for neural recordings in mice and a wireless electrochemical impedance spectroscopy (EIS) device designed for cortisol detection in human sweat. Despite their apparent differences, both systems share a common foundation—the AD5934 impedance converter chip, generating sinusoidal excitation signals and measuring corresponding system responses.

Our fiber photometry system utilizes an SiPM as an alternative photodetector, addressing the power and sensitivity limitations of conventional counterparts. Additional optical excitation at an isosbestic point, often used for mitigating motion artifacts, was also used to correct for SiPM gain variations. Employing two impedance converters enables amplitude modulation with two carriers, which allows for distinguishing the main signal from the isosbestic control signal. Characterization tests confirmed the system's robustness to motion artifacts and temperature variations. In-vivo experiments demonstrated the system's functionality at significantly lower optical excitation powers comparing to commercial fiber photometry systems.

In the EIS device, the AD5934 was used for its originally intended purpose of impedance spectroscopy. When used with a cortisol immunosensor, it can determine the concentration of cortisol in a sample by measuring its impedance at a range of frequencies. The device has a compact form-factor, and is wireless and battery-powered. Adaptive gain control was implemented to enhance the device's dynamic range. Characterization tests on resistors, capacitors, and electrochemical samples, and comparative experiments against a commercial potentiostat validated the system's suitability for cortisol concentration measurement. The device showed promise for adaptation into a wearable device for daily semi-continuous cortisol monitoring.

The SiPM-based fiber photometry system and the compact EIS device stand as successful implementations of two biomedical measurement systems that benefit from the use of the AD5934 impedance converter chip. These two projects demonstrate the versatility of the AD5934 impedance converter, and meet their individual aims.

Acknowledgements

I would like to express my sincere gratitude to Dr. Kartikeya Murari, my supervisor, whose unwavering support, expertise, and patience have been invaluable throughout my research journey. His mentorship and support have been truly inspiring. I extend my appreciation to Dr. Amir Sanati Nezhad, my co-supervisor, for his oversight and guidance that contributed to the successful completion of my research.

Special thanks to Govind Peringod, Anupam Bisht, and Fereshteh Vajhadin for their assistance with the presented experiments, and to Fatemeh Haghayegh, Razieh Salahandish, Hirmand Hasanvand, and Mohsen Hassani for their their assistance in the earlier stages of testing. To my labmates and colleagues, your camaraderie and positive attitude in the lab made every day enjoyable.

I am grateful to my parents for their unwavering support, always prioritizing my education and ensuring I had the best opportunities to thrive academically. I am thankful to my brother for always being a friend and a source of emotional support.

Heartfelt appreciation goes to my friends, whose companionship has enriched my experience and helped my personal growth over the past three years. Your friendship made this academic journey truly memorable.

Lastly, I want to acknowledge the unspoken support of a dear friend who has made the past year more enjoyable. Your presence has been a source of motivation, and I am thankful for your patience and always being there for me.

Table of Contents

List of Figures

List of Tables

Chapter 1

Introduction

A fundamental approach for studying a system involves applying an excitation signal and measuring the system's response. This basic idea is the core of various widely used measurement techniques in very disparate fields including Magnetic Resonance Imaging (MRI), fluorescence spectroscopy, and resistance measurement with a multimeter.

In some cases, an oscillating excitation signal at a specific frequency is employed, and the response signal component at the same frequency is extracted. In such cases, the system's information is encoded as the amplitude and/or phase of this signal component. The use of an oscillating signal serves purposes such as extracting information at a specific frequency or a range of frequencies or improving signal quality by associating it with a single frequency enabling rejection of broadband and offset noise. Electrochemical Impedance Spectroscopy (EIS) and fiber photometry are examples of important measurement tools in biomedical research that often rely on this technique.

EIS is a method that can reveal valuable information about the content of a sample by measuring its impedance at a range of frequencies. For example, it can determine the concentration of biomarkers in a sample. In a typical EIS experiment, to measure impedance at a specific frequency, a sinusoidal voltage is applied across a sample, and the resulting current is measured. The ratio of voltage amplitude to current amplitude represents the magnitude of impedance, while the phase difference denotes the phase of the impedance.

Fiber photometry is an optical method for recording neural activity. Fiber photometry detects neural activity by measuring changes in the concentration of fluorescent neural activity indicators in a targeted region of animals' brains. Fluorescence measurement is done by directing excitation light to brain tissue and measuring the resulting fluorescent emission. Amplitude modulation is often used in fiber photometry. That

is, the excitation light has oscillating intensity. Therefore, a change in fluorescence appears as a change in the amplitude of the fluorescent emission light.

As described above, both methods follow the same concept. The applied voltage and measured current in EIS correspond to the excitation and emission light in fiber photometry. For the latter, optoelectronic devices such as light-emitting diodes and photodiodes enable conversion between electrical and optical quantities. Given the shared principle, employing similar electronics for their implementation becomes a logical choice. A practical solution is using commercially available integrated circuits designed for impedance spectroscopy. Particularly, AD5933 and AD5934 (Analog Device, USA), are electronic parts that are widely used for impedance measurements in various applications. AD5933 and AD5934 are impedance converters that can excite a sample, measure the resulting current, and calculate its Fourier transform.

1.1 Aims

The aims of this thesis are to develop two systems with the AD5934 impedance converter at the core of their electronics.

1. A silicon photomultiplier-based low-light fiber photometry system for recording neural activity in mice
2. An EIS device for detecting cortisol in human sweat

This thesis is divided into three parts. The present chapter provides background information on the AD5934 chip which is crucial to both projects. This includes a description of the device's hardware and operation, considerations for accuracy, and some notable work using the device. In Chapters 2 and 3, the fiber photometry and EIS projects are described in detail. Each of the two chapters includes fundamental concepts, related work, system design, characterization, and experimental results for its respective project.

1.2 The AD5934 Impedance Converter

The AD5934 is a specialized integrated circuit (IC) designed by Analog Devices, Inc [1]. It is an impedance converter system designed for impedance spectroscopy. Figure 1.1 shows the functional diagram and the simplest configuration for measuring impedance as recommended by the AD5934 datasheet. The unknown impedance to be measured is connected between the VOUT and VIN pins of the chip. The device operates by applying a known excitation voltage signal at a specified frequency to the target system, between the VOUT and VIN pins, to cause a current in it. With VIN being a high-impedance node, current flows from VOUT to the RFB pin. So, the resulting response current flowing into the RFB pin is converted to a voltage, and then

sampled and processed to determine the impedance characteristics of the tested element or material across the specified frequency range. The hardware and the measurement process are described in this section.

1.2.1 Hardware

The hardware consists of two blocks: the transmit stage and the receive stage (Figure 1.1). The transmit stage of the IC can provide an excitation voltage with controllable amplitude and frequency. The receive stage can measure a current, sample it, and calculate the Fourier transform to extract the signal's magnitude and phase.

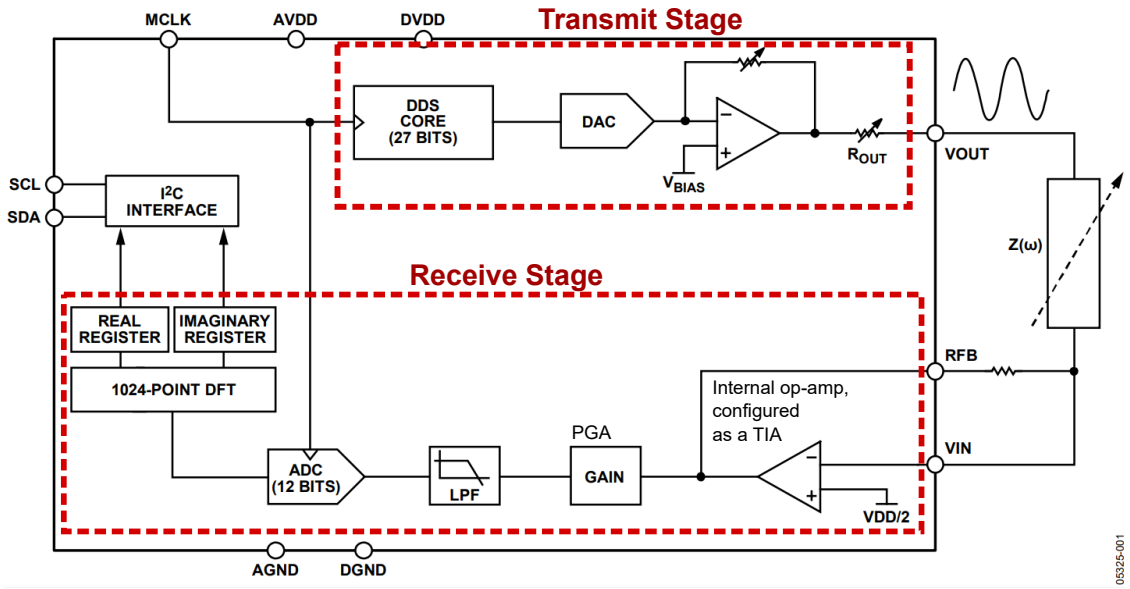

Figure 1.1: The transmit and receive stage, shown on the AD5934 block diagram adapted from the datasheet [1].

1.2.1.1 Transmit Stage

The transmit stage within the AD5934 incorporates a 27-bit Direct Digital Synthesis (DDS) core followed by a digital-to-analog converter (DAC) that generates a sinusoidal signal at a specific frequency. This signal is conditioned by an amplifier with variable gain that can set the excitation voltage to four different levels which can be selected by configuring the control register (Table 1.1).

Table 1.1: Excitation voltage levels with a supply voltage of 3.3 V

No.	Amplitude (V_{p-p})	DC Bias (V)
1	1.98	1.48
2	0.99	0.74
3	0.383	0.31
4	0.198	0.179

Measurements begin at the start frequency and then are repeated with a specified frequency increment. The start frequency is based on the start frequency register, which the user can write to the AD5934's random access memory (RAM) via the I2C interface. Although the DDS provides 27 bits of resolution, only the lower 24 bits of the start frequency register can be programmed. The start frequency is set using equation 1.1. Users can also set the frequency increment using a 24-bit register (equation 1.2). The number of increments is determined by a configurable 9-bit word. The chip returns to standby mode after measurements are made at all the specified frequencies.

$$\text{Start Frequency Code} = \left\lfloor \frac{\text{Start Frequency}}{MCLK} \times 2^{31} \right\rfloor \tag{1.1}$$

$$\text{Increment Frequency Code} = \left\lfloor \frac{\text{Increment Frequency}}{MCLK} \times 2^{31} \right\rfloor \tag{1.2}$$

$MCLK$ indicates the frequency that the chip is clocked at externally and $\lfloor\rfloor$ indicates the floor function. Based on these equations, the start and increment frequencies can range between $\frac{MCLK}{2^{31}}$ and $\frac{MCLK \times (2^{24}-1)}{2^{27}}$. However, this range will be limited based on the sampling limitations described in the Receive Stage section. The maximum number of increments is 511. The chip can also be programmed to wait a certain number of periods before the receive stage is activated.

1.2.1.2 Receive Stage

The role of the receive stage within the AD5934 is the conversion of the current in the unknown impedance into digital data, and extracting its amplitude and phase. It is composed of an op-amp followed by a programmable gain amplifier (PGA), an anti-aliasing filter, and a 12-bit analog-to-digital converter (ADC). The inverting input and the output of the internal op-amp are accessible while the non-inverting input is fixed at VDD/2. In the simplest impedance measurement setup, the internal op-amp is configured as a transimpedance amplifier (TIA) that converts the current through the unknown impedance to a voltage that can be sampled by the ADC. Following the TIA, the PGA's gain can be set to 1 or 5 by the control register. Then, the signal undergoes low-pass filtering before entering the 12-bit ADC. The digital output from the ADC is fed into the digital signal processing (DSP) core of the AD5934, where the single-point Discrete Fourier Transform (DFT) is calculated for the sampled data. The DFT result at the excitation frequency is stored as two 16-bit numbers representing the real and imaginary part of the current which corresponds to the admittance of the unknown impedance. These data can be read via the I2C interface.

To calculate the unknown impedance, data from a reference impedance is required. For simplicity, a known resistor can be first measured. Then, the impedance is calculated based on the following equations,

where R and and I are the real and imaginary numbers stored in the AD5934 RAM, and the ref subscripts indicate data for the known resistor. R_{known} is the known resistance value and Z is the unknown impedance.

$$|Z| = \frac{\sqrt{{R_{ref}}^2 + {I_{ref}}^2}}{\sqrt{R^2 + I^2}} \times R_{known} \tag{1.3}$$

$$\angle Z = \arctan\left(\frac{I_{ref}}{R_{ref}}\right) - \arctan\left(\frac{I}{R}\right) \tag{1.4}$$

1.2.2 Measurement Process

The process of performing a frequency sweep with the AD5934 involves several steps that are triggered by commands sent to the chip via the I2C interface. The process is as follows:

1. **Set Frequency Sweep Parameters:** The start and increment frequencies, number of increments, and settling cycles are first programmed into the appropriate AD5934 registers.

2. **Enter Standby Mode:** Before starting a frequency sweep, the device must be transitioned into standby mode. In standby mode, the VOUT and VIN pins are internally connected to ground. The excitation voltage level and the PGA gain are also set as part of the operating mode register.

3. **Enter Initialization Mode:** In this mode, the excitation signal is applied, and the VOUT and VIN pins are set to their intended level. However, the ADC does not sample the voltage. This stage can be prolonged for the system to reach steady state.

4. **Enter Frequency Sweep Mode:** The ADC begins sampling after the programmed settling time cycles elapse. This settling time is predetermined by the user.

5. **Polling the Status Register for DFT Completion:** DFT completion and the availability of impedance data are indicated by a bit in the status register. When this bit is set, the impedance data can be read.

6. **Polling the Status Register for Sweep Completion:** The status register also signals the end of a sweep. This step is only required if the increment frequency feature is being used. In this step, the user may choose to put the AD5934 in shut-down or stand-by mode or trigger measurement at the next frequency.

1.2.3 DFT calculation

An excitation voltage v_{ex} and a sample admittance Y leads to a current of $Y \cdot v_{ex}$. With a system current-to-voltage gain of α, the voltage sampled by the ADC (v_i) is $\alpha \cdot Y \cdot v_{ex}$. For simplicity, α was assumed to be a real number here. Let G and B represent the conductance and susceptance of the sample, respectively, i.e. $Y = G + jB$. A, f, T_s, and n are the excitation voltage amplitude, excitation frequency, sampling period, and sample index, respectively. V_{EX} and V_I are phasor representations of v_{ex} and v_i.

$$v_{ex}(n) = A\cos\left(2\pi f T_s n\right) = \mathrm{Re}\{Ae^{j2\pi f T_s n}\} \tag{1.5}$$

$$V_I = \alpha Y V_{EX} = \alpha Y A = \alpha(G + jB)A \tag{1.6}$$

$$= \alpha GA + j\alpha BA \tag{1.7}$$

$$= \alpha GA + \alpha BAe^{j\pi/2} \tag{1.8}$$

$$v_i(n) = \mathrm{Re}\{V_I e^{j2\pi f T_s n}\} = \alpha GA\cos\left(2\pi f T_s n\right) + \alpha BA\cos\left(2\pi f T_s n + \pi/2\right) \tag{1.9}$$

$$= \alpha GA\cos\left(2\pi f T_s n\right) - \alpha BA\sin\left(2\pi f T_s n\right) \tag{1.10}$$

The AD5934 calculates the single-point DFT ($V_i(f)$) of its sampled signal ($v_i(n)$) in order to estimate G and B (equation 1.11). The real and imaginary part of the single-point DFT, are extracted as two quadrature components, one in-phase with the excitation signal, and one orthogonal to it [2]. The admittance is calculated by dividing these two components by the system gain (α) which is determined by a calibration measurement. G_M and B_M indicate the estimates for G and B are calculated by the AD5934 (equations 1.12-1.13).

$$V_i(f) = F\left\{v_i(n)\right\} = \sum_{n=0}^{N-1} v_i(n) \cdot \left(\cos\left(2\pi f T_s n\right) - j\sin\left(2\pi f T_s n\right)\right) \tag{1.11}$$

$$G_M = \frac{1}{\alpha}\frac{1}{A} \cdot \frac{2}{N} \cdot \sum_{n=0}^{N-1} v_i(n) \cdot \left(\cos\left(2\pi f T_s n\right)\right) \tag{1.12}$$

$$B_M = \frac{1}{\alpha}\frac{1}{A} \cdot \frac{2}{N} \cdot \sum_{n=0}^{N-1} v_i(n) \cdot \left(-\sin\left(2\pi f T_s n\right)\right) \tag{1.13}$$

G_M can be written as the sum of G and an error term.

$$\begin{aligned} G_M &= \frac{1}{\alpha}\frac{2}{AN}\sum_{n=0}^{N-1}\left[\alpha GA\cos\left(2\pi fT_s n\right) - \alpha BA\sin\left(2\pi fT_s n\right)\right]\cdot\cos\left(2nfT_s n\right) \\ &= \frac{2}{N}\sum_{n=0}^{N-1} G\cos^2\left(2\pi fT_s n\right) - \frac{2}{N}\sum_{n=0}^{N-1} B\sin\left(2\pi fT_s n\right)\cdot\cos\left(2\pi fT_s n\right) \\ &= \frac{2}{N}G\sum_{n=0}^{N-1}\left(\frac{1+\cos\left(4\pi fT_s n\right)}{2}\right) - \frac{2}{N}B\sum_{n=0}^{N-1}\frac{\sin\left(4\pi fT_s n\right)}{2} \\ &= G + \frac{G}{N}\sum_{n=0}^{N-1}\cos(4\pi fT_s n) - \frac{B}{N}\sum_{n=0}^{N-1}\sin\left(4\pi fT_s n\right) \end{aligned} \tag{1.14}$$

Similarly, B_M can be written as:

$$\begin{aligned} B_M &= \frac{1}{\alpha}\frac{2}{AN}\sum_{n=0}^{N-1}\left(\alpha GA\cos\left(2\pi fT_s n\right) - \alpha BA\sin\left(2\pi fT_s n\right)\right)\cdot\left(-\sin\left(2\pi fT_s n\right)\right) \\ &= \frac{-2}{N}\sum G\cos\left(2\pi fT_s n\right)\cdot\sin\left(2\pi fT_s n\right) + \frac{2}{N}\sum_{n=0}^{N-1} B\sin^2\left(2\pi fT_s n\right) \\ &= -\frac{G}{N}\sum_{n=0}^{N-1}\sin\left(4\pi fT_s n\right) + \frac{B}{N}\sum_{n=0}^{N-1}\left(1-\cos(4\pi fT_s n)\right) \\ &= B - \frac{G}{N}\sum_{n=0}^{N-1}\sin\left(4\pi fT_s n\right) - \frac{B}{N}\sum\cos\left(4\pi fT_s n\right) \end{aligned} \tag{1.15}$$

The summations in equations 1.14 and 1.15 can be simplified:

$$\begin{aligned} C_1 &= \sum_{n=0}^{N-1}\sin\left(4\pi fT_s n\right) = \frac{\sin\left(2\pi f(N-1)T_s\right)\sin\left(2\pi fNT_s\right)}{\sin\left(2\pi fT_s\right)} \\ C_2 &= \sum_{n=0}^{N-1}\cos\left(4\pi fT_s n\right) = \frac{\cos\left(2\pi f(N-1)T_s\right)\sin\left(2\pi fNT_s\right)}{\sin\left(2\pi fT_s\right)} \end{aligned} \tag{1.16}$$

Substituting 1.16 in 1.14 and 1.15, we get:

$$\begin{aligned} G_M &= G + C_2\frac{G}{N} - C_1\frac{B}{N} \\ B_M &= B - C_1\frac{G}{N} - C_2\frac{B}{N} \end{aligned} \tag{1.17}$$

The relative error can be written as:

$$\begin{aligned} \delta G &= \frac{C_2\frac{G}{N} - C_1\frac{B}{N}}{G} = \frac{C_2}{N} - \frac{C_1}{N}\frac{B}{G} \\ \delta B &= \frac{C_1\frac{G}{N} - C_2\frac{B}{N}}{B} = \frac{C_1}{N}\frac{G}{B} - \frac{C_2}{N} \end{aligned} \tag{1.18}$$

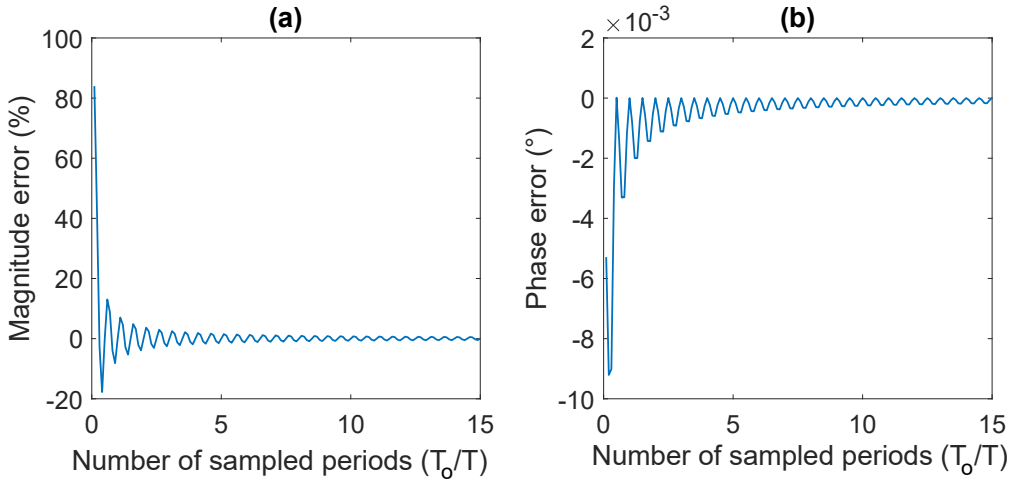

Figure 1.2: Error in calculated magnitude and (b) phase for an admittance with a phase of 0.

Note that for C_1 and C_2 to be simultaneously zero, $2fNT_s$ has to be an integer. NT_s is the total sampling time (T_o). So, the expression can be written as $2 \cdot \frac{T_o}{T}$ where T is the signal's period. Therefore, when the sampled data includes integer multiples of half the signal's period, the error is zero and G_M and B_M are equal to G and B.

1.2.4 Frequency Range and Voltage Range Considerations for Accuracy

1.2.4.1 Frequency Range

The AD5934 performs single-point DFT on a 1024-point sequence of data sampled by the ADC. As evident in equation 1.16 and 1.18, the accuracy of the obtained admittance, and equivalently the impedance, depends on its phase and the number of sampled periods ($\frac{T_o}{T}$).

The single-point DFT calculation was simulated in MATLAB. A sine wave with an amplitude of 0.1 V, sampled at 1024 points, was used as the excitation voltage, and the magnitude of the admittance was set to 10 Ω^{-1}. The number of periods per sampling time was swept from 0.1 to 15 in steps of 0.1. Conductance and susceptance were calculated based on equation 1.12-1.13. The magnitude and phase of the admittance and their error were then calculated. The simulation was repeated at admittance phases of 0, +45°, and -45°. The errors are shown in figures 1.2 to 1.4. As the number of periods increases, the error caused by non integer values of $2 \cdot \frac{T_o}{T}$ decreases. For instance, in all cases in the simulation, for $\frac{T_o}{T}$ of 14.4 and higher, the error in magnitude was below 1%.

The AD5934 data sheet characterizes the device at a clock frequency of 16.776 MHz. At this clock frequency, the ADC sampling rate is 250 kSPS and the sampling period is $T_s = 1/f_s = 4$ μs. Therefore, the total sampling time is $1024 \times T_s = 4096$ μs. For $\frac{2T_o}{T} = 8192 \times 10^{-6} \times f$ to be an integer, the excitation

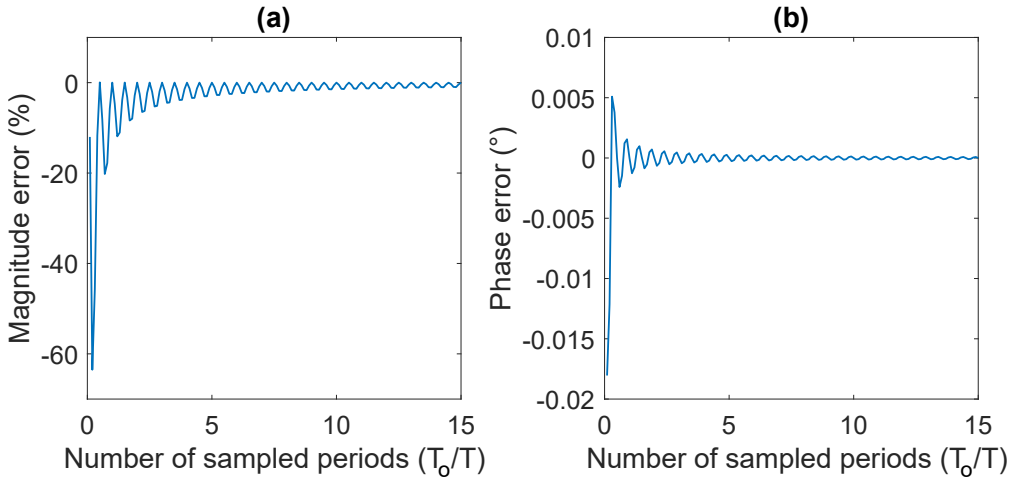

Figure 1.3: Error in calculated magnitude and (b) phase for an admittance with a phase of +45°.

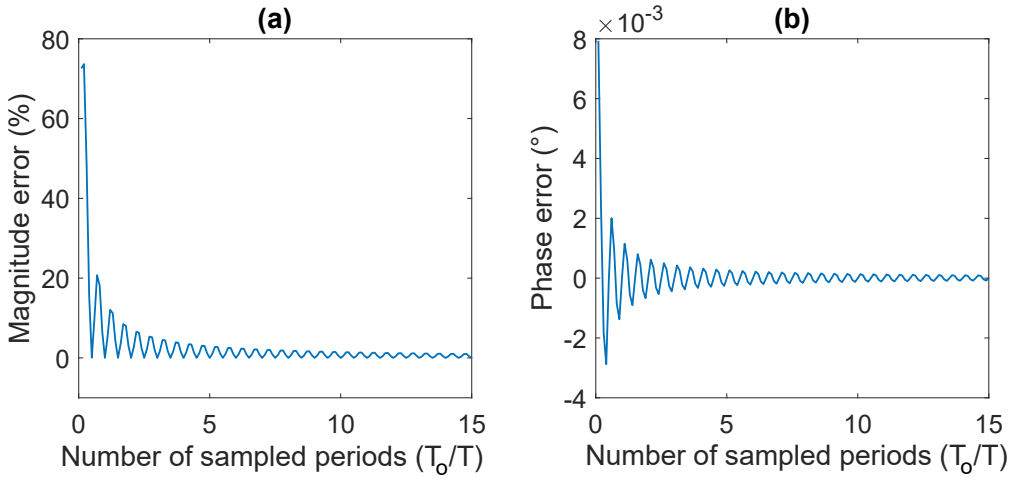

Figure 1.4: Error in calculated magnitude and (b) phase for an admittance with a phase of -45°.

frequency must be a multiple of $\frac{1}{8192\times10^{-6}s} = 122.07$ Hz. As shown in the simulations above, high accuracy can also be achieved by sampling over multiple periods. For example, with this clock frequency, a $\frac{T_o}{T}$ of 14.4 is equivalent to an excitation frequency of 3515.6 Hz. So, for excitation frequencies higher than 3515.6 Hz, the error in admittance magnitude is below 1%. The frequency must also be below the Nyquist limit of $f_s/2 = 125$ kHz.

The ADC sampling rate linearly changes with the clock frequency (f_{clk}). That is, f_s is equal to $\frac{250\times10^3}{16.776\times10^6} \cdot f_{clk} = f_{clk}/67.104$. The excitation frequency criteria change accordingly. These criteria are summarized in equation 1.19 and 1.20 where m is the minimum number of samples per period which is selected based on the desired accuracy.

$$f < \frac{f_s}{2} = \frac{f_{clk}}{134.208} \tag{1.19}$$

$$\begin{cases} f = k \cdot \dfrac{f_s}{2N} = k \cdot \dfrac{f_{clk}}{2 \times 1024 \times 67.104} =\approx k \cdot \dfrac{f_{clk}}{137429} \quad , \quad k \in \mathbb{N} \\ \quad or \\ f > m \cdot \dfrac{f_s}{N} = m \cdot \dfrac{f_{clk}}{1024 \times 67.104} \approx m \cdot \dfrac{f_{clk}}{68714} \end{cases} \tag{1.20}$$

1.2.4.2 Voltage Range

The AD5934 has a 12-bit ADC. Therefore, with a supply voltage of VDD, the ADC resolution or the least significant bit (LSB) is VDD/2^{12}. For supply voltages of 3 V and 5 V, this parameter is equal to 0.73 mV and 1.22 mV respectively. The amplitude of the voltage being sampled should be many times larger than the resolution in order to achieve high accuracy.

To determine the minimum voltage amplitude, we simulated a similar DFT calculation in MATLAB. The resolution was set to 1.22 mV and the voltage amplitude was swept from 0.1 mV to 20 mV. The amplitude of the signal determined by the DFT was compared to the actual signal amplitude. For a purely resistive load, in order to achieve an error of less than 5% and less than 1%, minimum signal amplitudes of 3.7 mV and 13.5 mV were required respectively (Figure 1.5) corresponding to 3 and 11 LSBs.

1.2.5 Comparison Between Impedance Converters and DSP Processors

The AD5934 and AD5933, offer a convenient solution for studying a system's response to sinusoidal excitations. The simplicity and convenience of these devices comes at the cost of limited flexibility. Some of the

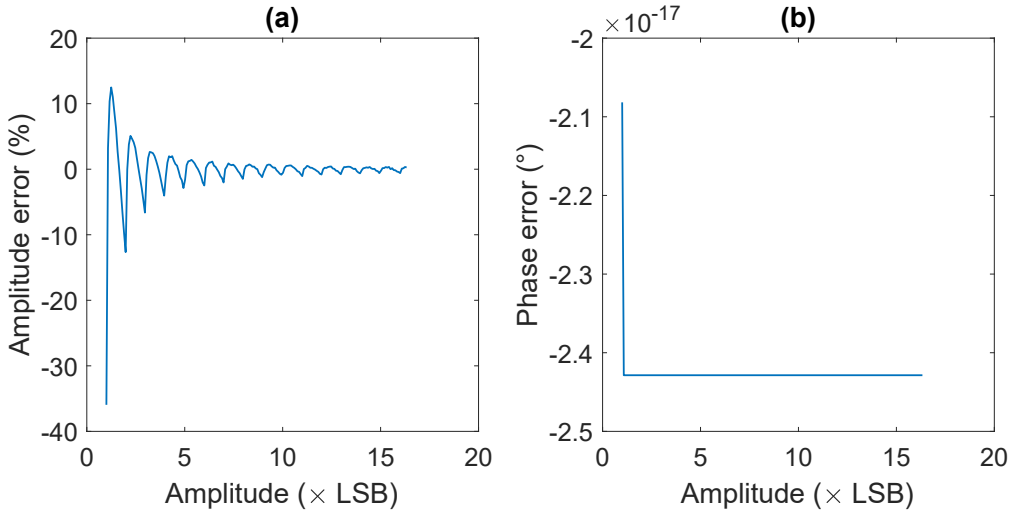

Figure 1.5: Error in calculated magnitude and (b) phase for a purely resistive load, for different amplitudes of the ADC input voltage. The voltage resolution is 1.22 mV.

limitations were discussed in Section 1.2.4. One notable limitation is the fixed and relatively low number of points (1024) over which the single-point DFT is calculated. With a 1024-point sequence of data, for a certain clock frequency, only at 1024 excitation frequencies the single-point DFT is equal to the conventional DFT. Therefore, measurement accuracy is highly dependent on the chosen excitation frequency.

Another hardware limitation is that there are only four options for the excitation signal level, and therefore additional signal conditioning is often required for the excitation voltage. Also, the AD5934's internal opamp's non-inverting input is not accessible and the biasing cannot be controlled. Additionally, this op-amp is automatically disabled between measurements which affects the biasing of the front-end electronics.

On the other hand, using a DSP (digital signal processing) processor provides a more flexible and customizable solution. A DSP processor allows for complete control over the signal processing algorithms and measurement process. However, the increased flexibility comes at the cost of complexity. Developing this system with a DSP processor involves programming signal processing algorithms, handling hardware interfaces, and ensuring synchronization between excitation and measurement stages.

The complexity of the DSP solution may be unnecessary for some applications. Despite the limitations of the AD5934 and AD5933, their convenience can make them suitable for such applications. Their straightforward setup and ease of use make them an attractive choice, especially for researchers and developers who prioritize convenience and want to implement the system without delving into intricate DSP programming. It is crucial, however, to be mindful of the devices' limitations. By considering these constraints and making appropriate design choices to ensure accuracy, the AD5934 and AD5933 can serve effectively in a variety of

applications.

The AD5933 and AD5934 are very similar devices. Despite the similarities between the two chips, the AD5933 is much more prevalent. This is mostly due to the higher ADC sampling rate which extends the range of measurable frequencies. The AD5933 also includes a temperature sensor and an internal oscillator.

For the EIS project, we are interested in frequencies between 1 Hz to 5 kHz. The ratio of the maximum to minimum excitation frequency in this range is 5000. Based on the frequency criteria mentioned in the previous section, for both chips with a fixed clock frequency, the maximum to minimum excitation frequency cannot exceed $(f_s/2)/(1 \times (f_s/2048)) = 1024$. Therefore, a configurable clock frequency is required. With a clock frequency of 8 MHz, and m of 14.4, the AD5934 can measure impedance at excitation frequencies between 1.68 kHz and 59.6 kHz. Frequencies below this range can be measured at lower clock frequencies. For instance at a clock frequency of 8 kHz, and m of 14.4, excitation frequencies between 1.68 Hz and 59.6 Hz can be. By sampling an integer number periods, the frequency range can be further extended. Therefore, an AD5934 with a configurable clock frequency is sufficient for this application. Details on the excitation frequencies will be provided in Chapter 3.

In the fiber photometry project, continuous measurements at only two frequencies will be made. The selected frequencies were between 260 Hz and 290 Hz. These excitation frequencies can be used with a clock frequency of 1 MHz. Therefore, the AD5934 is sufficient in this application as well.

Since the AD5934 can cover the excitation frequencies in both projects, and these projects do not involve temperature sensing the AD5934 was selected in this study.

1.2.6 Applications

Given the significant similarities between the AD5933 and the AD5934, and the AD5933's prevalence in the existing related literature, in this section, previous work using this chip is included. To the author's best knowledge, the AD5934 and AD5933 impedance converters have not been previously used in fiber photometry. However, they have widespread applications in impedance spectroscopy, in various fields including health monitoring, agriculture, and environmental and structural health monitoring in various industries [3–11].

Many researchers have designed customized analog front-ends to interface the AD5933 with various sensors to measure a wide range of parameters. For instance, Qui et al. interfaced the AD5933 with a two-terminal capacitive pressure sensor. The device was implemented as a wearable chest patch. In this configuration, the impedance was obtained by applying a 96 kHz voltage to the sensor and measuring the subsequent current. The sensor impedance was an indicator of respiration [12].

In another study by Liu et al., the AD5933 was incorporated into a four-electrode bio-impedance mea-

surement system for non-invasive glucose monitoring. A tetrapolar electrode was placed on the patient's fingertip, and its impedance was measured. In this four-electrode configuration, the current flowing through two electrodes was controlled, while the voltage across the other two electrodes was measured [13].

Rieger et al. designed a highly configurable analog front-end for this impedance converter. This front-end allows researchers to measure impedance in five modes. These modes include two, three, or four-terminal measurements, which involve either the application of voltage and measurement of the resulting current or vice versa. They proposed this impedance spectroscopy module as part of a multi-sensor system for monitoring the functionality of medical implantable microelectrodes [14].

Several researchers have worked on improving the device's accuracy and dynamic range. Stadnyk and Khoma analyzed the frequency-dependent leakage error, which reveals crucial considerations for precise measurements. Additionally, they investigated the impact of windowing techniques on the accuracy of impedance calculations [2].

Matsiev further delved into the leakage error, and in addition to the AC leakage, quantified the error resulting from the DC component of the AD5933's input signal. This analysis, unlike the analysis in Section 1.2.3 and Stanyk's work, does not disregard the DC component of the signal. This leads to an additional constraint on the measurable frequencies. Their mathematical analysis revealed that for eliminating the DC leakage, the number of periods sampled must be an integer. Matsiev also proposed a method for measuring DC impedance using the DC leakage [15]. Chabowski et al. also studied the practical considerations for the operation frequency to improve the device's accuracy [16]. Their experimental results were in close alignment with the previously mentioned studies.

Some researchers have broadened the frequency range of the AD5934 by employing a configurable oscillator for the clock signal [17–19]. Notably, Hoja and Lentka, reported accurate measurements across frequencies spanning seven decades. In addition, efforts to enhance the dynamic range of the system have led some researchers to implement an adaptive gain scheme [20,21]. Chen et al., for instance, conducted precise measurements within the range of 0.02 kΩ to 200 kΩ, surpassing the specified impedance measurement range of 1 kΩ to 10 MΩ in the AD5933 datasheet by one decade.

In this thesis, the selection of the AD5934 for the EIS device was driven by its proven versatility and effectiveness, as demonstrated in previous works. Our objective was to customize an EIS system to measuring cortisol concentration. Building upon the foundation of earlier research involving the AD5934, our efforts were focused on optimizing key parameters such as the excitation signal, impedance range, form factor, and scan timing to align with the requirements of cortisol analysis.

In the context of fiber photometry, the AD5934 can sinusoidally modulate the excitation light's amplitude. Amplitude modulation in a fiber photometry system offers advantages for low-light measurements and neural

activity detection. Modulation helps mitigate low-frequency noise, particularly 1/f noise, which tends to dominate at lower frequencies. By modulating the excitation signal, the system can reject signals and noise in unwanted frequency bands. This enables the system to detect signals in response to different sources of excitation. For fiber photometry with multiple optical excitation sources, a different AD5934 can be used for driving each excitation source and calculating the subject's response to it.

1.3 Summary

This chapter laid the foundation for understanding the operation of the AD5934 impedance converter for studying systems by applying excitation signals and measuring their responses. Two crucial measurement tools in biomedical research, fiber photometry and Electrochemical Impedance Spectroscopy (EIS) were briefly introduced, and their relation to AD5934's operation was discussed. Details about the impedance converter's hardware and measurement process were provided and practical considerations for accurate measurement were presented. The chapter concluded by providing insights into the wide range of applications of the AD5933 and AD5934 in various fields, including biomedical applications. With the basic fundamental concepts covered, the subsequent chapters of the thesis focus on two systems utilizing this device: An in-vivo fiber photometry system for neural recordings in mice (Chapter 2), and an EIS device for cortisol detection in sweat (Chapter 3).

Chapter 2

Fiber Photometry

2.1 Introduction

2.1.1 Motivation

Many aspects of neural activity, including neurotransmitter release, depend on intracellular calcium ions. Calcium indicators are fluorescent transmembrane proteins that can bind to these intracellular calcium ions. Consequently, their fluorescence properties change in response to changes in calcium levels. This change can be an indication of neural activity. Fiber photometry is a technique that allows the in vivo measurement of neural activity via fluorescence measurement. A fiber photometry system delivers light to calcium indicators in the brain and measures the light which is emitted in response to this excitation. The emission light intensity corresponds to the fluorescence and therefore calcium concentration. GCaMP, a genetically encoded calcium indicator, is widely used for fiber photometry experiments. It can be encoded into the genome of organisms, allowing researchers to target specific cells of interest leading to the expression of GCaMP in a specific type of cells, for instance neurons or astrocytes. Many researchers have used GCaMP to study neural activity in a variety of contexts, revealing valuable information about brain function [22]. However, there are still limitations and challenges associated with fiber photometry systems. For example, conventional systems use photomultiplier tubes (PMT) that require a high bias voltage or photodiodes that need high optical power. This results in expensive bulky systems or leads to photobleaching or phototoxicity, respectively [23].

One potential solution to these challenges is the use of silicon photomultipliers (SiPMs) as the photodetector. SiPMs are silicon-based photodetectors that can be affordable, sensitive, and relatively low-voltage alternatives to PMTs. This study explores the feasibility of using SiPMs in fiber photometry systems.

2.1.2 Aims

The aim of this project is to develop a SiPM-based fiber photometry system to measure neural activity in mice, using sinusoidally modulated excitation light. The fiber photometry system should meet the following criteria:

- Can be powered by a 6 V voltage source.
- Use an optical excitation power less than 10 μW for *in-vivo* measurements.
- Be able to detect changes in fluorescence as small as 5%.
- Can correct for SiPM gain variations.
- Can mitigate the effects of motion artifacts.

This system will be implemented, characterized and its performance will be demonstrated in *in-vivo* experiments. In characterization tests, the fluorescence of fluorescent solutions are measured in order to evaluate the system's stability, sensitivity, linearity, dynamic range, and robustness to artifacts. In *in-vivo* experiments, we will use our fiber photometry setup to record brain activity in mice. These recordings will be compared to those from a commercial fiber photometry system.

2.1.3 Organization

Section 2.2 provides background information on fiber photometry and the SiPM, demonstrating the potential use of the SiPM in fiber photometry. Section 2.3 describes the design of the system and two methods to correct for artifacts and stabilize the system's gain. In Section 2.4, characterization test results, demonstrating the system's performance, are included. Section 2.5 includes results from *in-vivo* experiments using the designed fiber photometry system.

2.2 Background

In this section, the basics of fiber photometry are first explained. Conventional hardware and signal processing approaches are described with a focus on photodetectors used in fiber photometry. The SiPM is introduced as a potential alternative, and its advantages and disadvantages are discussed.

2.2.1 Fiber Photometry

Fiber photometry is a technique used to measure neural activity in deep brain structures of freely-moving animals. In fiber photometry, the fluorescence of genetically-encoded calcium indicators (GECIs) in the brain is measured. These measurements capture the fairly slow changes in intracellular calcium concentration in the brain. This fluorescence is an indicator of neural activity in a targeted population of cells of a specific type.

To measure the brain tissue fluorescence, a fiber optic patch cord is connected to a ferrule implant in the subject's brain, with the fiber tip embedded in a region of interest (Figure 2.1). Excitation light is directed into the brain by the optical fiber. This causes the calcium indicator to fluoresce. The resulting emission and backscattered excitation signal is collected back through the same fiber. The emission is separated using optical filters and directed to a photodetector which measures the fluorescence emission light's intensity [22]. Typical fiber diameters are from 100 to 400 μm. Thus, the signal represents population activity in a volume around the tip of the fiber.

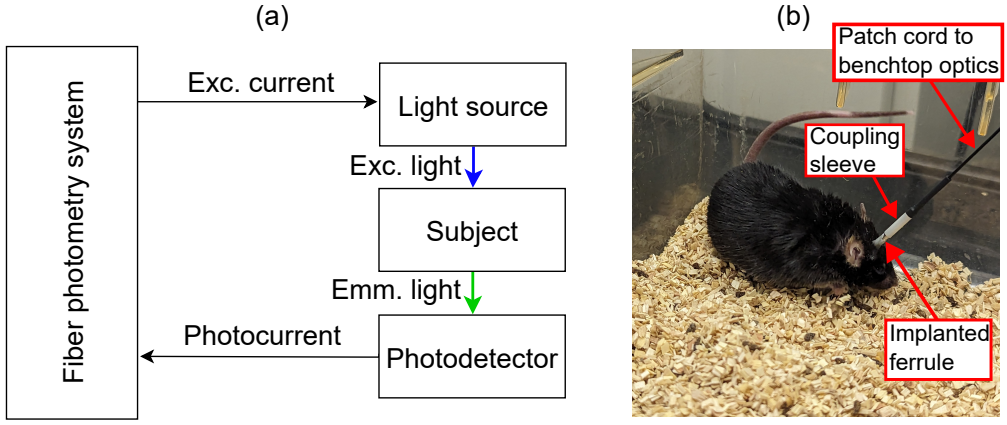

Figure 2.1: (a) Block diagram of a simple fiber photometry system. (b) A mouse with an optical fiber connected to a ferrule implant on its brain.

2.2.1.1 Isosbestic Control

One challenge with fiberoptic measurements in freely-moving animals is noise due to motion. Motion can change the coupling between the implanted ferrule and the patch cord. This manifests as a change in the measured signal which can be attributed to either a change in Ca^2+ concentration or motion. Furthermore, applying optical excitation to the tissue may lead to photobleaching which causes an exponential decay in the emission from the tissue. Using additional illumination an isosbestic wavelength is one way to solve this problem. GCaMP's isosbestic wavelength is the excitation wavelength at which the emission intensities from Ca^2-bound and unbound GCaMP are the same [22].

The excitation and emission spectra of a GCaMP variant (GCaMP6f) are shown in Figure 2.2. At a 470 nm excitation, GCaMP bound to calcium is excited much more than unbound GCaMP, leading to strong Ca^2+-dependent fluorescence. At the isosbestic point, around 410 nm, both the bound and unbound forms of GCaMP are equally well-excited leading to no Ca^2+ dependence in the resulting fluorescence. The artifacts however, are similarly reflected in the emissions corresponding to excitation at both 470 nm and 410 nm. Therefore, a simultaneous excitation at 410 nm can provide information about artifacts without being affected by neural activity. This information can be used to isolate the neural activity signal from the Ca^{2+}-independent signals. The block diagram of a fiber photometry system with isosbestic control is shown in Figure 2.3. Amplitude modulation, described in Chapter 1, allows for distinguishing between the emission caused by each excitation wavelength [22].

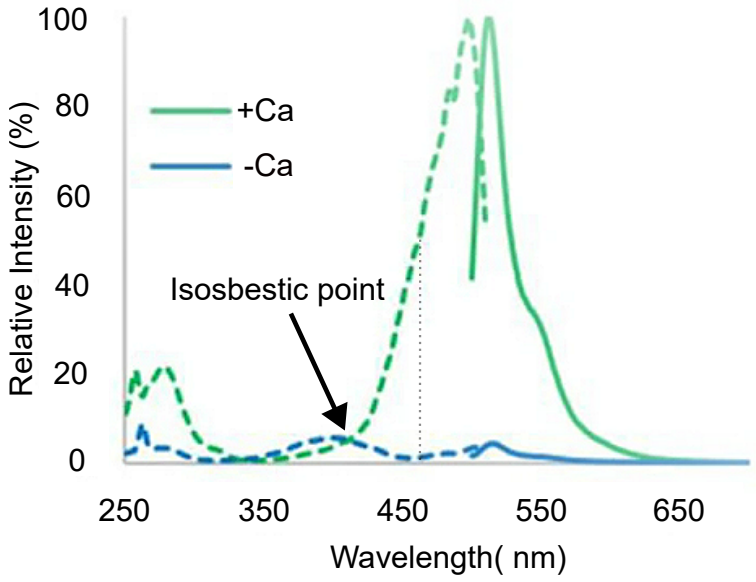

Figure 2.2: GCaMP6F's excitation and emission spectra in Ca^2-bound (+Ca) and unbound (-Ca) states. Solid lines show the emission spectra at a 495 nm excitation and dashed lines show the excitation spectra [24]. The dashed vertical line marks the 470 nm wavelength.

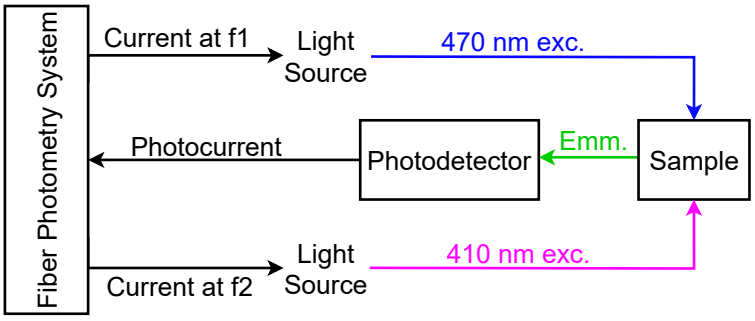

Figure 2.3: Block diagram of a fiber photometry system with isosbestic control.

2.2.1.2 Hardware

A typical fiber photometry setup consists of light sources, lenses, dichroic beamsplitters, optical filters, optical fibers, and a photodetector. In a system with isosbestic control, two light sources with peak wavelengths of 470 nm and 410 nm are used. Using dichroic beamsplitters and lenses, the two lights are combined and directed to an optical fiber. This optical fiber is connected to the end of a fiber probe implanted in the brain and delivers light to it. The light excites fluorescence and the emitted light as well as the backscattered excitation light is collected by the fiber. It is filtered to isolate the portion in the GECI's emission wavelength range and reject the rest. The emission light is then directed to a photodetector [22].

Electronics for fiber photometry include a light source driver, a detector amplifier, and a data acquisition system. The light source driver modulates the light source intensity. Most commonly, the intensity is sinusoidally modulated at different frequencies for each light source. The detector amplifier amplifies the weak fluorescence signal from the detector, and finally, the data acquisition system records the fluorescence signal [23].

Commercial systems for fiber photometry are available. Notably, Doric Lenses (Quebec, Canada) offers photometry cubes with built-in LEDs, filters, and detectors, as well as LED drivers and read-out electronics. Along with a data acquisition system and software, this setup provides a convenient off-the-shelf solution for researchers. However, these setups are bulky, expensive and use relatively high excitation powers in the range of tens of microwatts [23, 25], leading to photobleaching.

Researchers continue to develop novel photometry systems with the aim to achieve improved signal-to-noise ratio, smaller size, lower power, or increased sensitivity compared to commercial systems. For instance, a custom integrated circuit (IC) that incorporates low-power electronics required for photometry was developed. The electronics, along with implantable and fiber-less optoelectronic setups, can provide a wireless solution [26]. These devices however, suffer from low sensitivity and require high excitation powers. Additionally, alternative photodetectors and electronics have been used to achieve better SNR and sensitivity at lower excitation powers [23]. Alternative light source multiplexing approaches have also been explored to enhance SNR [27].

2.2.1.3 Signal Processing

In fiber photometry using isosbestic control, the raw data is processed to obtain a metric called $\Delta F/F$, where F is the fluorescence intensity and ΔF is the change in it. This signal represents the change in Ca^{2+}-dependent fluorescence intensity which corresponds to neural activity in the targeted cell population.

Several fiber photometry systems have been developed, and the specifics of signal processing may differ

among them. For instance, they may use different filtering, fitting, or scaling techniques to process the signals. Despite these differences, the general steps to calculate $\Delta F/F$ are typically the same. First, the sensor output components corresponding to the Ca signal and control channels are extracted using the Fourier Transform. The signals are then smoothed to remove high-frequency noise. After that, the signals' baselines are removed. This baseline includes low frequency fluctuations in the signal caused by factors other than calcium concentration, for example photobleaching. Then the signal and control channels' data are scaled to the same level, resulting in two normalized and filtered signals with one main difference; one includes calcium concentration information, and one does not. Finally, the processed control signal is subtracted from the Ca-dependent signal (ΔF). This removes common artifacts from the main signal. To represent the fluorescence change relative to the control signal ($\Delta F/F$), the obtained ΔF is divided by the control signal [22, 28].

2.2.1.4 Photodetectors in Fiber Photometry

The most common photodetectors used in fiber photometry are silicon photodiodes, photomultiplier tubes (PMT), and Complementary Metal-Oxide-Semiconductor (CMOS) cameras.

Photodiodes are the most widely used optical sensors in fiber photometry. Newport (California, USA) offers a photoreceiver consisting of a silicon photodiode followed by an amplifier, providing a convenient solution for many researchers [29–35]. Despite their wide use, silicon photodiodes have relatively low sensitivity compared to other detectors, such as photomultiplier tubes. As a result, in order to achieve high signal-to-noise ratios, high optical powers (tens of microwatts) are often required, which can lead to photobleaching or phototoxicity in biological samples.

Photomultiplier tubes are highly sensitive devices that are commonly used to detect and amplify optical signals in several scientific fields. In fiber photometry, PMTs have been utilized to measure calcium concentration in the brain, using excitation powers as low as 100 nW [23, 36, 37]. More recently, PMTs have also been employed in fiber photometry to measure other biomarkers such as dopamine [38, 39]. While PMTs are a valuable tool for studying neural circuits and behaviors, they have limitations. PMTs require a high (hundreds to thousands of volts) bias voltage, are bulky, and can be easily damaged when exposed to high levels of light.

CMOS cameras are also used in fiber photometry for measuring calcium concentrations [22,26,40]. CMOS cameras are relatively low-cost, and can offer spatial information. However, they have lower sensitivity and higher noise levels.

2.2.2 The Silicon Photomultiplier

A silicon photomultiplier (SiPM) is a photodetector that consists of an array of hundreds or thousands of integrated single-photon avalanche diodes (SPADs). Photons can trigger an avalanche process in SPADs, creating an electrical current, which can be thought of as a digital signal - the avalanche may or may not occur. When the SPADs are connected to a common readout, they can generate an analog signal produced by the sum of the single SPAD signals [41]. The SPADs in an SiPM are also referred to as pixels.

SiPMs have become increasingly popular due to their numerous advantages, such as single-photon sensitivity alongside broad dynamic range at a lower cost than PMTs. They are also insensitive to magnetic fields, require a relatively low bias voltage (few tens of volts), have high gain, and good time resolution. However, they have certain disadvantages such as a high dark-count rate and sensitivity to their bias voltage and temperature [42, 43]. Despite these drawbacks, SiPM has emerged as a promising alternative to PMTs in many applications.

SiPMs have found applications in particle physics, nuclear physics, and biomedical imaging. For instance, SiPMs are used for gamma-ray detection to study gravitational wave electromagnetic counterparts [44]. SiPMs have been used for scintillation detection in calorimeters intended for electron-positron colliders [45, 46]. SiPMs are also utilized in Time-of-Flight (TOF) measurements in Light Detection and Ranging (LiDAR) and in Positron Emission Tomography (PET) for biomedical imaging [47, 48].

Detector Read-out

Optical detectors typically output a current which is usually measured using a transimpedance amplifier (TIA) that converts a current to a voltage while holding a constant bias voltage across the detector. A typical front-end for an SiPM is depicted in Figure 2.4. The op-amp bias voltage and a power supply set the SiPM anode and cathode voltage respectively, controlling the SiPM bias voltage, while the TIA converts the SiPM output current to a voltage. The TIA can have a capacitive or predominantly resistive feedback (Z_f). The former is referred to as a Charge Sensitive Amplifier (CSA). For the latter, the capacitive portion of the feedback sets the bandwidth. Based on the requirements of the application, either of these feedback networks may be more appropriate for the SiPM read-out. CSAs are well suited to applications with a small charge range that have strict noise requirements, but do not require high timing accuracy [49]. For instance, a CSA is often used for positron emission tomography (PET) in medical imaging [50, 51]. A TIA with resistive feedback is used when timing accuracy is important, for example in TOF-PET and fluorescence lifetime measurements (FLT) [49, 52, 53].

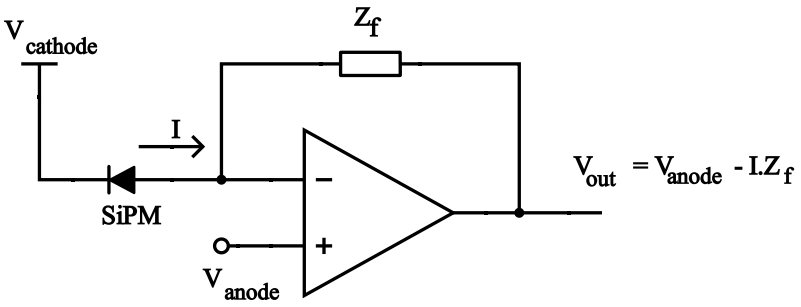

Figure 2.4: Typical SiPM read-out circuit. I is the photocurrent generated by the SiPM.

The Effect of Temperature and Bias Voltage on the SiPM Gain

The gain of an SiPM is the amount of charge that is produced for each photon that is detected, normalized to the elementary charge. At a typical operating point, the SiPM gain is highly sensitive to its temperature and bias voltage. At a higher bias voltage, the probability of avalanche breakdown in each SPAD is higher, causing the gain to be higher. On the other hand, at a higher temperature, the energy that is needed to cause the avalanche multiplication is higher. Therefore, the break-down voltage of the SPADs is higher and the SiPM gain at a fixed bias voltage is lower. This relation is reflected in equation 2.1, where G is the gain of the SiPM, C_{pixel} is the capacitance of a single pixel, V_{bias} is the bias voltage, V_{BD} is the breakdown voltage of the SiPM, and e is the charge of an electron [54].

$$G = C_{pixel}\frac{(V_{bias} - V_{BD})}{e} \tag{2.1}$$

V_{BD} changes linearly with temperature as evident in equation 2.2. In this equation, $V_{BD}(T)$ represents the breakdown voltage at temperature T, V_{BD0} is the breakdown voltage at a reference temperature T_0, and $\beta > 0$ is the temperature coefficient of the breakdown voltage [54].

$$V_{BD}(T) = V_{BD0}\left[1 + \beta(T - T_0)\right] \tag{2.2}$$

By substituting V_{BD} from equation 2.2 in equation 2.1, gain can be written as a function of the bias voltage and temperature (equation 2.3). In this equation, C_pixel's variations, due to bias or temperature, in the proximity of the operating point are ignored.

$$G = (\frac{C_{pixel}}{e})V_{bias} + (\beta \cdot \frac{C_{pixel}}{e} \cdot V_{BD0})T - \frac{C_{pixel}}{e} \cdot V_{BD0}(1 + \beta T_0) \tag{2.3}$$

Or simply:

$$G = aV_{bias} + bT + c \tag{2.4}$$

Where a, b, and c are constants. a and b are positive and negative respectively, meaning gain linearly increases when increasing voltage, and linearly decreases when increasing temperature. For instance Gil et al. reported a linear relationship between the gain of two S10362–11-025P (Hamamatsu, Japan) SiPMs and their bias voltage. At a bias voltage of 72 V and temperature of 24 °C, gain changed by approximately 20% when the bias voltage changed by 1%. Also, gain changed by approximately 7% in response to a 1% change in absolute temperature [55].

Gain Stabilization

The sensitivity of the SiPM gain to temperature and bias voltage presents a challenge in applications that require high accuracy. The stability of temperature and bias voltage are both important in order to keep the gain constant. Efforts to stabilize gain have been focused on mitigating the effects of temperature variations by two main methods. One is utilizing cooling systems to control the detector's temperature accurately. The other approach is monitoring the temperature and compensating for it accordingly. This compensation can be done by adjusting the bias voltage, or by correcting the SiPM output in postprocessing.

The most commonly used method to control the SiPM temperature is the use of Peltier coolers [56]. For instance, Anderson et al. thermally connected an SiPM to a Peltier plate. To stabilize the temperature, the temperature was continuously monitored and the cooling element's driving voltage was adjusted accordingly [57]. Raylman et al. immersed an SiPM in a circulating bath of mineral oil to lower and stabilize its temperature [56]. In another work, the SiPM enclosed in a copper enclosure. This enclosure was cooled with a mixture of water and ethylene glycol circulating through brass tubing channels [58].

Gain stabilization can be achieved by utilizing a hardware feedback loop to adjust the SiPM's bias voltage. From equation 2.1 it can be inferred that, when temperature changes by ΔT, to keep gain constant, the bias voltage should be adjusted based on equation 2.5.

$$\Delta V_{bias} = \frac{-b}{a} \cdot \Delta T \tag{2.5}$$

Bencardino and Eberhardt monitored the SiPM temperature by a thermistor. The SiPM was characterized in order to find a temperature coefficient to convert temperature variations to their equivalent bias voltage variations. Based on this coefficient, the thermistor's output was scaled by an amplifier and applied to the SiPM cathode. With a temperature variation of 3°C, gain variations were reduced from 33% to

1% [59]. Licciulli et al. used a second SiPM in the dark as the temperature sensor. The SiPM's dark pulses were detected and converted to a voltage adjusting the photodetector's bias voltage. Using this compensation method, gain variations were reduced by 28 times when temperature varied between 20°C and 30°C [54].

Alternatively, the required bias voltage can be determined in software. To control the SiPM gain, Marrocchesi et al. set the SiPM bias voltage via a benchtop power supply according to continuous temperature measurements [43]. Gil et al. designed a microcontroller-based programmable power supply for this purpose, reducing gain variations by 60 times while the temperature varied between 20°C and 30°C [55]. Several others have taken this approach to date [44, 60–62].

SiPM readings can also be corrected in software. Gong et al. implemented this gain stabilization technique in a SiPM-based spectrometer. They monitored the temperature, and corrected the output pulse amplitudes of the SiPM to a reference temperature [63].

2.2.3 SiPM and AD5934 in Fiber Photometry

SiPMs have not yet been utilized in fiber photometry. However, they have excellent properties which make them a promising photodetector in fiber photometry. Particularly, in contrast with APDs and CMOS cameras, SiPMs' high gain and sensitivity allow low excitation powers. While PMTs also have this advantage, they require a much higher bias voltage. SiPMs on the other hand, are better suited to battery-powered solutions because of their relatively low bias voltage. Moreover, SiPMs are more affordable. Therefore, SiPMs can be explored as a viable option for fiber photometry applications.

The AD5934, despite being designed for impedance spectroscopy can be utilized in other measurement systems that rely on amplitude modulation. The AD5934 generates data that represents amplitude and phase of the sinusoidal current it receives while outputting a fixed sinusoidal voltage. When it is used to measure an impedance, this data shows admittance. When interfaced with an optical system, this data can represent fluorescence. To measure fluorescence, the AD5934's sinusoidal output voltage can be used to drive a light source to generate excitation light at a selected frequency. The resulting emission can be detected by a photodetector. The photocurrent can be fed to the AD5934 for measurement. In this work, a fiber photometry system, with an SiPM as the photodetector is designed. An AD5934 is used for the excitation and read-out electronics.

2.3 Design

In this section, the three key blocks of the design - optics, electronics and signal processing - are described. First, the fundamental structure of the system is presented. Then, two correction approaches

(bias-monitoring and gain monitoring) and their corresponding design configurations are introduced.

2.3.1 Optics

In Ca^{2+}-sensitive fiber photometry using GCaMP probes, a light source with a wavelength of 470 nm causes fluorescence which is modulated by neural activity. Figure 2.5 illustrates the diagram of the optical setup for measuring fluorescence. Here, amplitude modulation is used, and fluorescence is encoded as the photodetector signal's amplitude. A 470 nm LED is driven at the frequency of f_1. The output light goes through a low-pass dichroic beamsplitter and is directed to the fluorescent sample. The beamsplitter reflects the resulting fluorescent light, which has a longer wavelength, onto the SiPM. This causes a photocurrent proportional to the fluorescence.

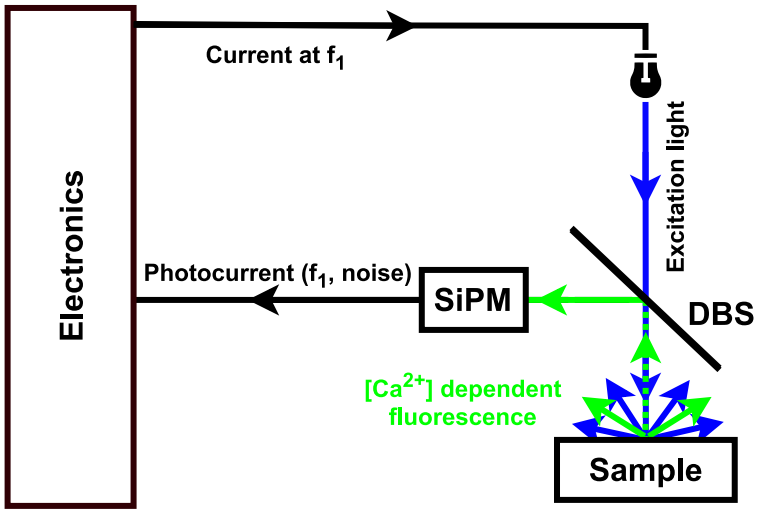

Figure 2.5: Diagram of an optical setup for measuring Ca^{2+}-dependant fluorescence. The dichroic beamsplitter (DBS) transmits short wavelength blue light and reflected longer wavelength green light.

2.3.2 Electronics

Figure 2.6 illustrates an overview of the electronics. A microcontroller controls the AD5934 and sets the SiPM's anode voltage through a digital to analog converter. The cathode voltage is set by a high-voltage voltage supply which is powered by an unregulated supply voltage (5.3-6.5 V). The rest of the electronics is powered by a 5-Volt regulator. The AD5934 generates a sinusoidal voltage for driving the light source. A voltage amplifier (VA) brings the voltage to the desired level. This voltage is input to a transconductance amplifier (TCA) which drives the LED. This light causes the fluorescent emission which is directed to the SiPM. The subsequent current through the SiPM is converted to a voltage by a transimpedance amplifier (TIA). This voltage is fed back into the AD5934 to calculate the DFT at the excitation frequency. The result

is read out by the microcontroller and sent via UART to a computer for further processing. Each part of this setup is described in the following sections.

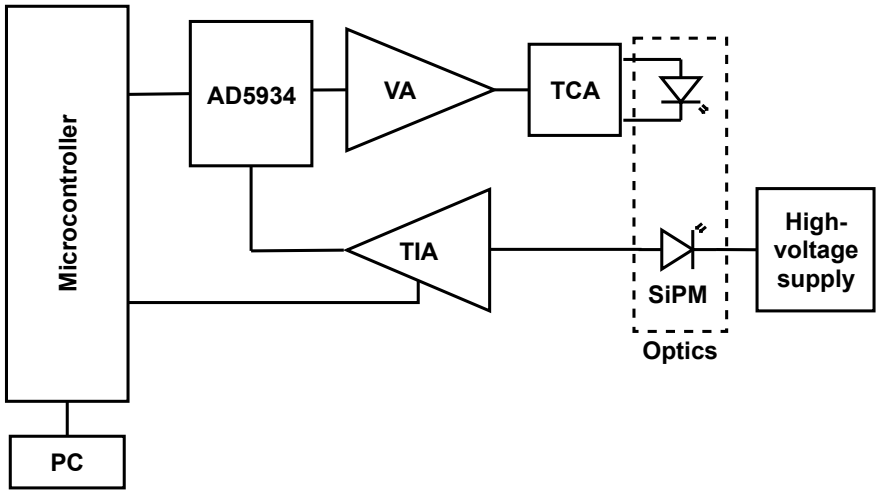

Figure 2.6: Block diagram of the AD5934-based electronics for photometry.

2.3.2.1 Microcontroller

A PIC24FV16KM202 microcontroller (Microchip, AZ) was programmed to communicate with the AD5934 using the I^2C protocol in order to set the measurement parameters, initiate the measurement, and read out the resulting data. After reading the AD5934 data, the microcontroller sends it to a computer via UART for further processing.

2.3.2.2 Excitation Stage

This stage consists of the AD5934, a voltage amplifier and a transconductance amplifier.

AD5934

The AD5934 generates a sinusoidal voltage with an offset of 775 mV and amplitude of 478 mV at the frequency of 260 Hz. The 1024-point buffer is filled every 65 ms which includes 17 periods of the excitation frequency. With an additional 8 ms for settling time and communication time, each round of excitation takes approximately 73 ms. A sample of the fluorescence intensity is available after this time.

Voltage Amplifier

The AD5934s output is AC-coupled to a voltage amplifier's (VA) input. The amplifier consists of an MCP642 op-amp configured as a low-pass inverting amplifier with a low-pass cut-off frequency of 1.78 kHz (Figure 2.7).

The gain and DC offset can be adjusted by two potentiometers. The amplifier's pass band voltage gain can vary between 0.066 (-23.6 dB) and 3.3 (10.4 dB).

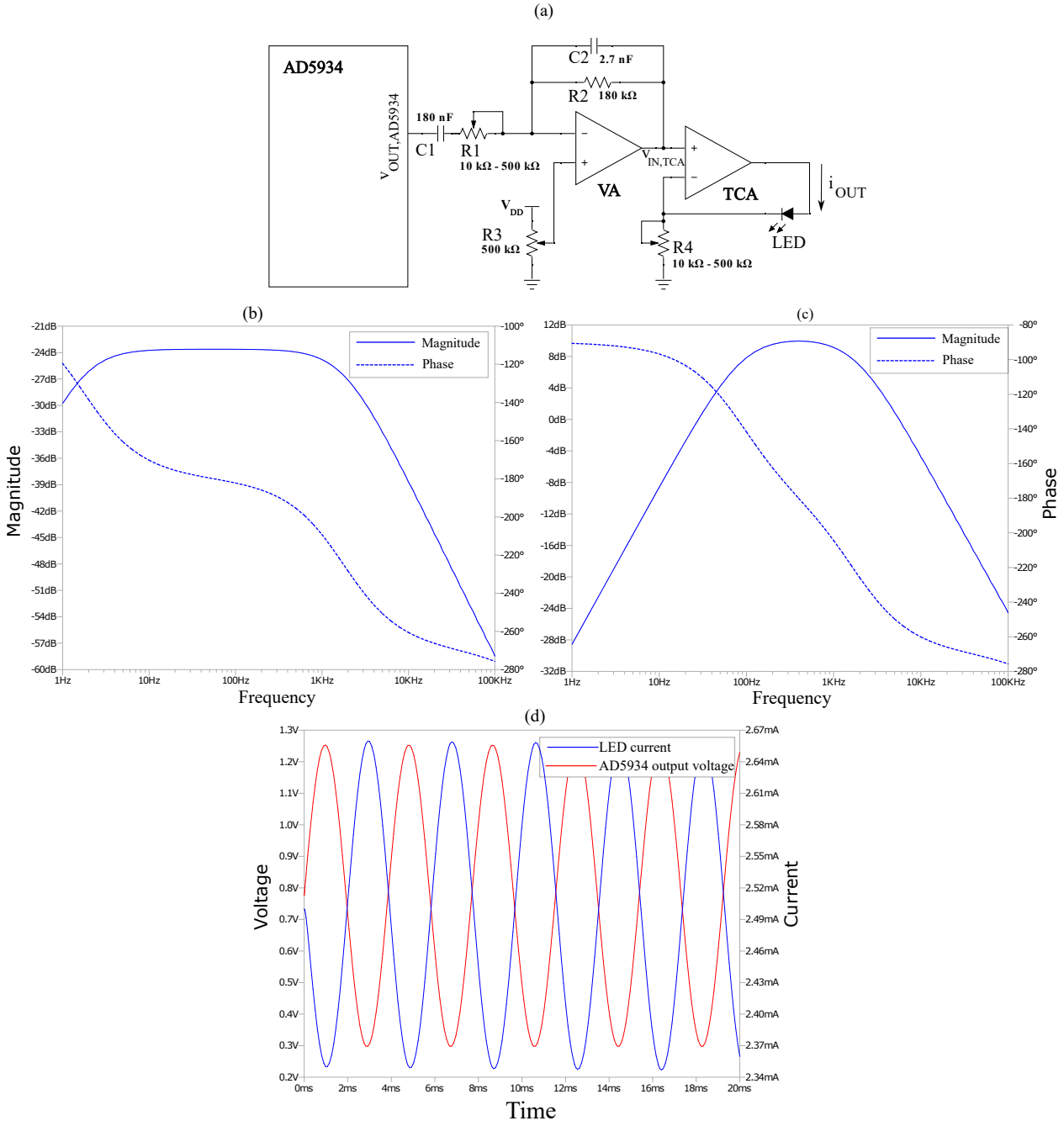

Figure 2.7: The excitation stage: the AD5934 drives a voltage amplifier followed by a TCA. (a) Circuit schematics. (b) VA gain when $R_1 = 500$ kΩ and (c) when $R_1 = 10$ kΩ, simulated in LTSPice. (d) LTSpice transient simulation showing the LED current when $R_1 = 100$ kΩ, $R_{3-1} = R_{3-2}$, and $R_1 = 1$ kΩ. R_{3-1} and R_{3-2} refer to the two sections of the R_3 potentiometer.

Transconductance Amplifier

Since LED output is proportion to the current flowing through it, the voltage amplifier's output is converted to a current by the transconductance amplifier (TCA) to drive the LED (Figure 2.7). The TCA gain can be adjusted by a potentiometer (R_4) from 0.1 mΩ^{-1} to 2 $\mu\Omega^{-1}$ to change the LED drive current to adjust excitation intensity.

The excitation stage sets the LED current according to equation 2.7 (AC level) and equation 2.9 (DC level). The parameters in these equations are shown in figure 2.7.

$$i_{out} = \frac{1}{R_4} \cdot v_{in,TCA} \tag{2.6}$$

$$= \frac{1}{R_4} \cdot \frac{R_2}{R_1} \cdot v_{o,AD5934} \tag{2.7}$$

$$I_{OUT} = \frac{1}{R_4} \cdot V_{IN,TCA} \tag{2.8}$$

$$= \frac{1}{R_4} \cdot \frac{R_{3-1}}{R_{3-1} + R_{3-2}} \cdot V_{DD} \tag{2.9}$$

2.3.2.3 Receive Stage

This stage includes a high-voltage supply, a transimpedance amplifier and the AD5934.

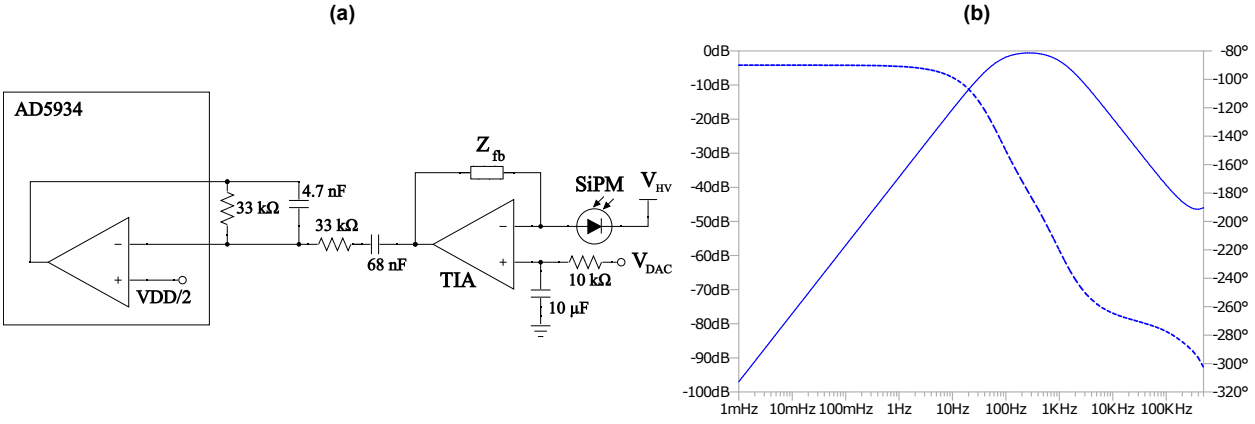

Figure 2.8: The receive stage: a TIA followed by the AD5934's internal amplifier. (a) Schematics. (b) LTSpice simulation of the internal amplifier.

High-voltage Supply

A step-up DC-DC converter (TPS61391, Texas Instruments) generates a 55.32 V voltage to bias the SiPM cathode.

Trans-impedance Amplifier

Another MCP642 op-amp was configured as a TIA (Figure 2.8). The TIA is biased by the digital-to-analog converter (DAC) of the microcontroller. Sockets are placed on the PCB for the TIA feedback impedance so that the gain can be easily changed. The SiPM current flows into the feedback branch of the TIA, meaning that the TIA output voltage is proportional to the SiPM current.

AD5934

The internal op-amp of the AD5934 is biased at the mid point of its supply voltage range. The output and the inverting input pins of the op-amp are accessible through pins 4 and 5 of the AD5934 respectively. This op-amp is configured as a band-pass filter with a gain of one and bandwidth of 71 Hz to 1 kHz. The internal op-amp's output is sampled at 15625 SPS by the AD5934's ADC. The DFT of each 1024-point data segment is calculated by the AD5934 at a rate of approximately 13.7 SPS, setting the overall fluorescence measurement sampling rate. For each segment, two numbers representing the real and imaginary part of the voltage at the excitation frequency are read by the microcontroller via I^2C.

2.3.3 Signal Processing

The magnitude of the AD5934 data is proportional to the SiPM current and consequently corresponds to the sample's fluorescence. This magnitude is calculated in MATLAB according to equation 2.10 where R and I are the AD5934 data associated with the real and imaginary part of the signal.

$$\text{Magnitude} = \sqrt{R^2 + I^2} \tag{2.10}$$

Further data processing can mitigate artifacts and better extract information about neural activity.

2.3.4 Mitigating Artifacts

As discussed in Section 2.2, variations in the SiPM's temperature and bias voltage affect its gain. In this section, two methods (bias monitoring and gain monitoring) for addressing these issues are presented. The gain monitoring method is also intended for mitigating motion artifact which affect the overall system gain.

2.3.4.1 Bias Monitoring

The gain of an SiPM varies linearly with changes in temperature and bias voltage. As discussed in Section 2.2, many researchers have controlled the SiPM gain, by monitoring temperature and accurately controlling the bias voltage to account for temperature changes.

To implement a similar correction scheme in the present system, an additional temperature sensor must be used. The temperature of the SiPM must be continuously monitored, and the anode voltage should be adjusted accordingly. However, the accuracy and precision of the bias voltage limit the performance of this setup and are not well-suited to a compact low-power implementation.

Alternatively, the system's output can be corrected in software based on measurements of the bias voltage and temperature. This section presents a model for correcting the output signal amplitude based the bias voltage. Since gain's relationship with both the bias voltage and temperature follows the same mathematical form, this model can be similarly effective in compensating for temperature variations.

Optics and Electronics Setup

The optical setup remains unchanged, while an addition is made to the electronics (Figure 2.9). The high voltage supply's output is attenuated by approximately 11 times using a resistor divider to, bring it to a low voltage level. This attenuated voltage is then buffered to enable monitoring by the microcontroller's ADC or an external data acquisition device.

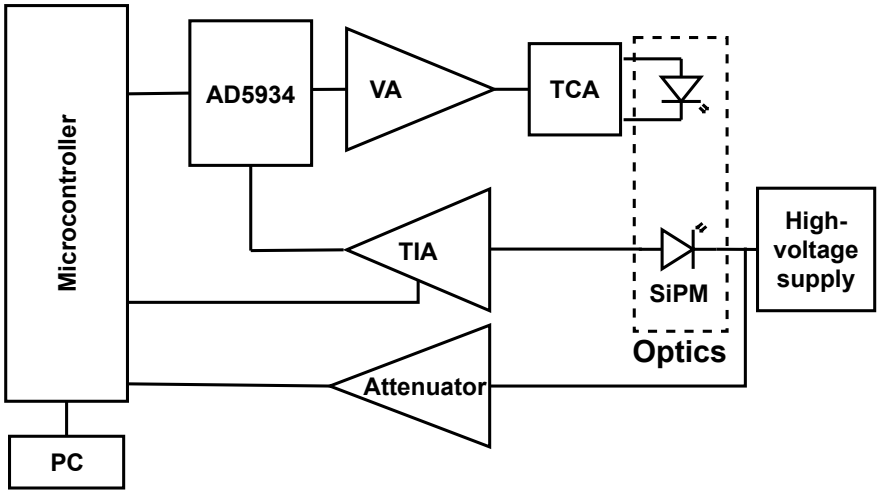

Figure 2.9: Block diagram of the electronics for the bias monitoring setup.

Correction Model

In this section, a method to correct for bias voltage variations at a fixed temperature is presented. The goal is to find the equivalent phototedector signal at a certain SiPM bias voltage for different values of the bias voltage.

Let v_{out} be the TIA output, and p_{in} be the optical power received by the SiPM. The photometry system measures the TIA output voltage amplitude (v_{out}) which corresponds to the optical power signal amplitude (p_{in}).

When measuring fluorescence, p_{in} is unknown. The objective is to correct v_{out} based on bias voltage (V_{HV}) recordings. That is, at a given V_{HV} of V_{HV1}, which leads to a v_{out} of v_{out1}, we need to find what v_{out} would have been if V_{HV} was at the nominal operating point of V_{HV0}.

System gain (A, defined in equation 2.11) is linearly dependent on the bias voltage V_{HV}.

$$A = \frac{v_{out}}{p_{in}} \tag{2.11}$$

$$A(V_{HV}) = aV_{HV} + b \tag{2.12}$$

The output signal voltage amplitude can be written as a function of V_{HV} and p_{in}:

$$v_{out}(V_{HV}, p_{in}) = A \cdot p_{in} = (aV_{HV} + b) \cdot p_{in} \tag{2.13}$$

At the operating point with a fixed optical power:

$$v_{out} = v_{out0}, \quad V_{HV} = V_{HV0}, \quad p_{in} = p_{in0} \tag{2.14}$$

At a fixed known p_{in} of p_{in0}:

$$v_{out}(V_{HV}, p_{in}) = v_{out}(V_{HV}, p_{in0}) \tag{2.15}$$

$$= (aV_{HV} + b) \cdot p_{in0} \tag{2.16}$$

$$= ap_{in0}V_{HV} + bp_{in0} \tag{2.17}$$

By recording data at a fixed optical power and fitting a linear regression model to the data with v_{out} and V_{HV} being the dependent and independent variables respectively, we can find the coefficients $ap_{in0} = a_0$ and $bp_{in0} = b_0$.

We will use the first-degree Taylor polynomial expansion of v_{out} as a function of V_{HV} and p_{in} to approx-

imate $v_{out}(V_{HV0}, p_{in1})$.

$$v_{out}(V_{HV0}, p_{in1}) \approx v_{out}(V_{HV1}, p_{in1}) + \left(\frac{\partial v_{out}}{\partial V_{HV}} \bigg|_{\substack{V_{HV}=V_{HV1} \\ p_{in}=p_{in1}}} \right) \cdot (V_{HV0} - V_{HV1}) \tag{2.18}$$

$$= v_{out}(V_{HV1}, p_{in1}) + a \cdot p_{in1} \cdot (V_{HV0} - V_{HV1}) \tag{2.19}$$

All variables in the question above are known, except for $a.p_{in1}$. To express this term in known variables we can rewrite is as:

$$a \cdot p_{in1} = a \cdot p_{in0} \cdot \frac{p_{in1}}{p_{in0}} = a_0 \cdot \frac{p_{in1}}{p_{in0}} \tag{2.20}$$

From equation 2.13 we have:

$$\frac{v_{out}(V_{HV1}, p_{in1})}{v_{out}(V_{HV0}, p_{in0})} = \frac{v_{out1}}{v_{out0}} \tag{2.21}$$

$$= \frac{aV_{HV1} + b}{aV_{HV0} + b} \cdot \frac{p_{in1}}{p_{in0}} \tag{2.22}$$

$$= \frac{p_{in0}}{p_{in0}} \cdot \frac{aV_{HV1} + b}{aV_{HV0} + b} \cdot \frac{p_{in1}}{p_{in0}} \tag{2.23}$$

$$= \frac{ap_{in0}V_{HV1} + bp_{in0}}{ap_{in0}V_{HV0} + bp_{in0}} \cdot \frac{p_{in1}}{p_{in0}} \tag{2.24}$$

$$\frac{p_{in1}}{p_{in0}} = \frac{v_{out1}}{v_{out0}} \cdot \frac{a_0V_{HV0} + b_0}{a_0V_{HV1} + b_0} \tag{2.25}$$

Substituting equation 2.25 in equation 2.20 we get:

$$a.p_{in1} = a_0 \frac{v_{out1}}{v_{out0}} \cdot \frac{a_0V_{HV0} + b_0}{a_0V_{HV1} + b_0} \tag{2.26}$$

And finally, by substituting $a.p_{in1}$ in 2.19, we have:

$$v_{out}(V_{HV0}, p_{in1}) = v_{out1} + a_0 \frac{v_{out1}}{v_{out0}} \cdot \frac{a_0V_{HV0} + b_0}{a_0V_{HV1} + b_0} \cdot (V_{HV0} - V_{HV1}) \tag{2.27}$$

Where:

$v_{out}(V_{HV0}, p_{in1})$ is the corrected output signal magnitude.

$v_{out1} = v_{out}(V_{HV1}, p_{in1})$ is the measured output signal amplitude.

$v_{out0} = v_{out}(V_{HV0}, p_{in0})$ is the measured output used to create the linear model.

a_0 and b_0 are the coefficients from applying linear regression on the modelling data.

V_{HV0} is the bias voltage at the reference operating point.

V_{HV1} is the bias voltage at the measurement point.

To find the model parameters, the high voltage bias and the system output at a fixed received optical power are recorded. In MATLAB, a linear regression model is fitted to the data, with bias voltage being the independent variable and the output signal amplitude being the dependent variable.

2.3.4.2 Gain Monitoring

The bias monitoring method requires accurate measurement of the bias voltage and temperature, data collection for modelling, calculating model parameters, and correcting the data. This requires additional sensors. Moreover, because of the variations in characteristics of different SiPMs, each device requires a unique model which is valid only in proximity to the operating point. The method introduced in this section relies on direct monitoring of the system's gain as opposed to monitoring the factors affecting it. As a result, variations caused by multiple sources are simultaneously accounted for. As discussed in Section 2.2, isosbestic control is commonly used in fiber photometry to correct for photobleaching and motion artifacts. The isosbestic control signal can also be used as a control for photodetector's gain.

Optics Setup

The conventional fiber photometry setup with isosbestic control is used here. In this setup, two LEDs with center wavelengths of 470 nm (XQEBLU, Cree LED) and 410 nm (QLUV04J3U, Quelighting Corp) are used. The emission light of the two LEDs are collimated by lenses (F240FC-A, Thorlabs). The output of the 470 nm LED is then filtered by a band-pass filter (DBS) with a center wavelength of 470 nm (ET470/24m, Chroma). Similarly, the 410 nm LED's output is band-pass-filtered with a center wavelength of 410 nm (FB410-10, Thorlabs). Both beams are incident on a 425 nm high-pass dichroic beamsplitter (DBS) (DMLP425, Thorlabs). The DBS passes the 470 nm beam and reflects the 410 nm one. As a result, the two beams are combined into one. This combined beam is incident on another high-pass DBS (T495lpxr, Chroma). Since both wavelengths are shorter than the DBS's cut-off wavelength (495 nm), the combined beam is reflected by the DBS. A lens (F240FC-A, Thorlabs) couples light into a fiber optic patch cord for delivery to the sample. The resulting fluorescent light is collected by the patch cord and directed to the 495 nm high-pass DBS. GCaMP's peak fluorescence emission wavelength is at 514 nm and the spectrum has a positive skew (Figure 2.2). Therefore, the fluorescent light passes through the DBS. A band-pass filter (ET525/50, Chroma) is used to filter the fluorescent light before being focused on to the SiPM (Fig. 2.10).

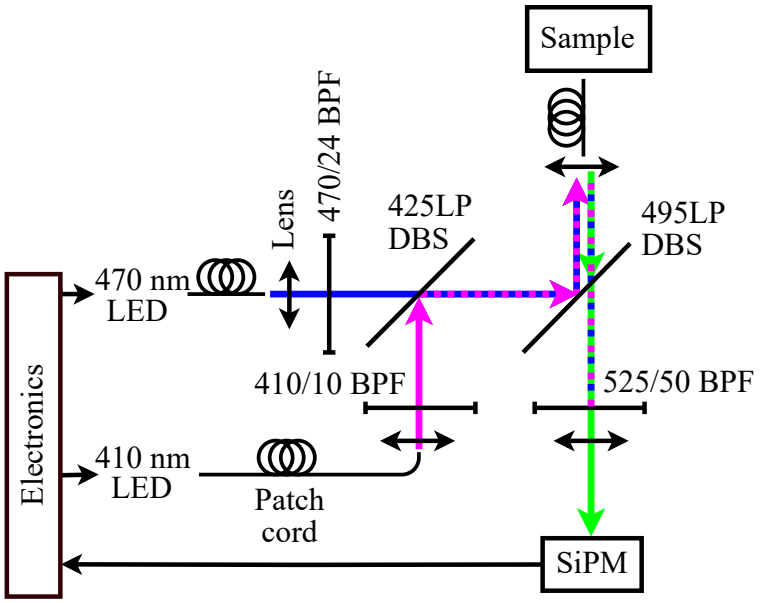

Figure 2.10: Block diagram of the optical setup with isosbetic control.

Electronics

The electronics are the same as the original design (Section 2.3.2), with an additional control signal path for the isosbestic channel (Figure 2.11). Each of the AD5934s generates an excitation signal and calculates the DFT at its respective channel's frequency.

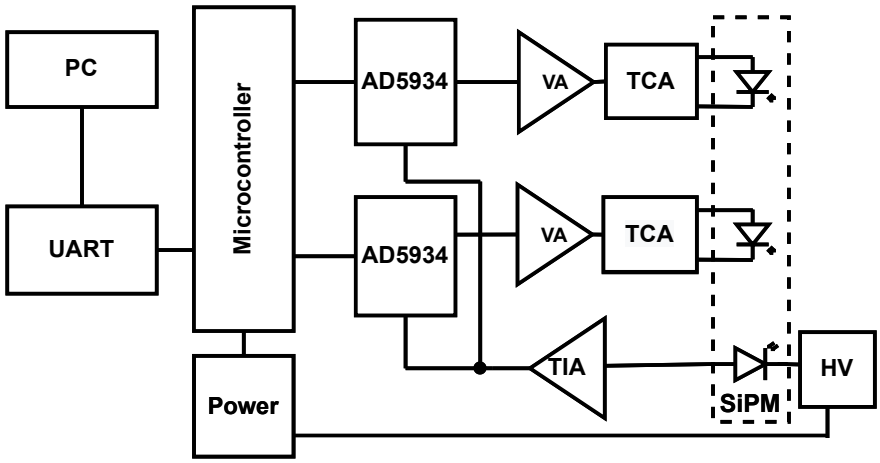

Figure 2.11: Block diagram of the electronics.

Correction Scheme

If the photodetector's current consists of two components, one only reflecting sensor gain and one additionally including an unknown gain, the unknown gain can be extracted. Figure 2.12 represents a measurement system

like this. In this diagram, x_1 and x_2 are optical excitation signals with constant amplitudes of $|X_1|$ and $|X_2|$ and frequencies of f_1 and f_2 (equation 2.28). x_1 is affected by an unknown varying gain (A_u). The second excitation light (x_2) is used for monitoring the system gain. Unlike A_u, A_0 which affects x_2 is constant. A sensing system with a gain of A_S converts the optical signal to an electrical one (z).

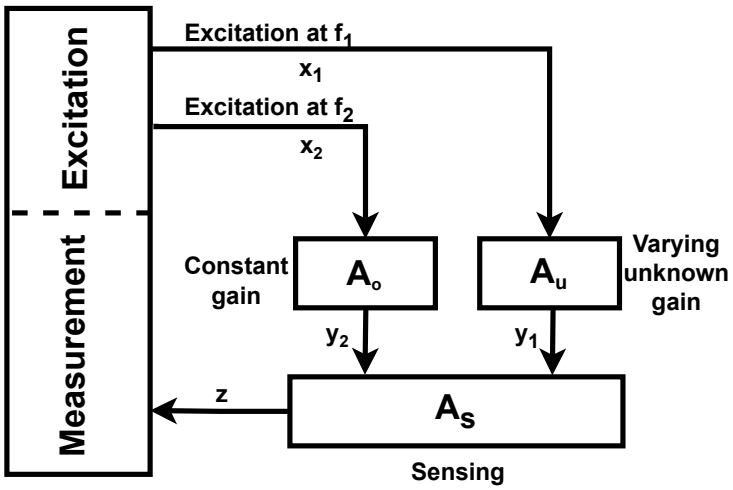

Figure 2.12: Block diagram representing a system with gain monitoring control.

$$x_1(t) = |X_1| \cdot \sin(2\pi f_1 t + \varphi_1) + B_1, \quad x_2(t) = |X_2| \cdot \sin(2\pi f_2 t + \varphi_2) + B_2 \tag{2.28}$$

z is the combination of two signals at f_1 and f_2.

$$z = A_u A_s x_1 + A_0 A_s x_2 \tag{2.29}$$

By calculating the Fourier transform, the amplitude of both signal components can be determined.

$$|Z_1| = A_u A_s |X_1| \tag{2.30}$$

$$|Z_2| = A_0 A_s |X_2| \tag{2.31}$$

In equation 2.31, $|Z_1|$ and $|Z_2|$ are the amplitudes of the f_1 and f_2 components of z. By taking the ratio of these two amplitudes, a metric proportional to A_u will be obtained which is not affected by changes in A_s.

$$\frac{|Z_1|}{|Z_2|} = \frac{|X_1|}{|X_2|A_0} \cdot A_u \tag{2.32}$$

In fiber photometry using GCaMP, the isosbestic channel can act as the gain monitoring signal in this scheme. However, the correction scheme is slightly more complicated as the sample includes two fluorescent elements: Calcium-bound GCaMP and unbound GCaMP. The goal is to extract the calcium-bound GCaMP fluorescence from channel 1's signal which contains both of the fluorescent elements.

The block diagram in Figure 2.13 illustrates a model for fiber photometry with isosbestic control. In this diagram, x_1 and x_2 are optical excitation signals with constant amplitudes of $|X_1|$ and $|X_2|$. x_1 and x_2 have a wavelengths of λ_1 (410 nm) and λ_2 (470 nm) respectively. Similar to the previous model discussed, x_1 and x_2 are sinusoidal signals with frequencies of f_1 and f_2. These signals are combined and are directed to a sample with a fluorescence capability of $A_F(\lambda)$. Motion can cause changes in the intensities of the excitation light delivered and the emission light collected. These can be combined into a gain A_a representing artifacts. A sensing system with a noisy gain of A_S converts the optical signal to an electrical one (z).

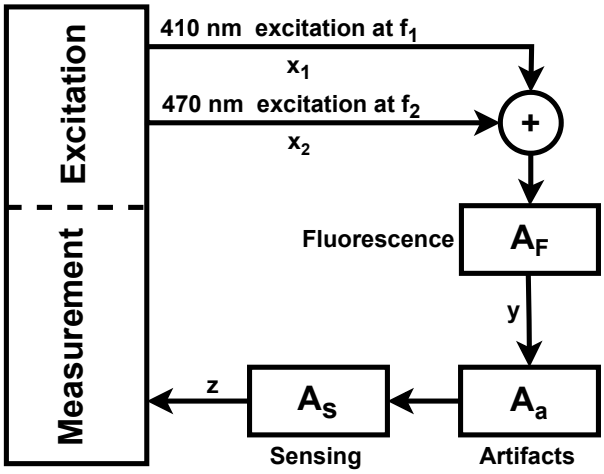

Figure 2.13: Block diagram of a model for fiber photometry with isosbestic control.

The AD5934s generate the LED driving signals corresponding to x_1 and x_2, and calculate the DFT of z at their respective frequency to extract the signal amplitudes at f_1 and f_2. The results are eventually received by MATLAB which performs the following processing. The goal of this processing is to derive a metric that represents the changes in concentration of calcium in the sample. The following analysis shows that the metric $\Delta z/z$ represents the calcium concentration, and it is robust to sensor gain changes and artifacts present in fiber photometry.

$A_F(\lambda)$ Affects the two excitation wavelength differently. The resulting fluorescent emission (y) consists of two components (y_1 and y_2) corresponding to excitation at λ_1 and λ_2 (equation 2.33).

$$y = y_1 + y_2 = A_F(\lambda_1)x_1 + A_F(\lambda_2)x_2 \tag{2.33}$$

When multiple (N) fluorescent substances are present, $A_F(\lambda)$ is the sum of the fluorescence capability of all substances (equation 2.34). In equation 2.34, $A_{F,i}(\lambda)$ is the fluorescence capability of the i^{th} substance at the excitation wavelength of λ. C_i is the concentration of the i^{th} substance and $F_{\lambda,i}$ is its intrinsic ability to fluoresce which is a constant.

$$A_F(\lambda) = \sum_{i=1}^{N} A_{F,i}(\lambda) = \sum_{i=1}^{N} C_i F_{\lambda,i} \tag{2.34}$$

There are two main fluorescent components in fiber photometry ($N = 2$): GCaMP bound to calcium (GCa), and GCaMP not bound to calcium (free, Gf). From equation2.34, $A_F(\lambda)$ depends on the concentration of each, and its ability to fluoresce at the excitation wavelength (λ). Changing indices (i) from equation 2.34 to GCa and Gf, $A_F(\lambda)$ can be written as:

$$A_F(\lambda) = A_{F,GCa}(\lambda) + A_{F,Gf}(\lambda) = C_{GCa}F_{\lambda,GCa} + C_{Gf}F_{\lambda,Gf} \tag{2.35}$$

From equations 2.33 and 2.35, fluorescent lights y_1 and y_2 can be determined based on GCaMP's fluorescence capability and concentration (Equations 2.36-2.37).

$$y_1 = \left(C_{GCa} \cdot F_{470,GCa} + C_{Gf} \cdot F_{470,Gf}\right) x_1 \tag{2.36}$$

$$y_2 = \left(C_{GCa} \cdot F_{410,GCa} + C_{Gf} \cdot F_{410,Gf}\right) x_2 \tag{2.37}$$

Since 410 nm is the isosbestic point of GCaMP, $F_{410,GCa} = F_{410,Gf}$ and is denoted by F_{410}. Therefore:

$$y_2 = \left(C_{GCa} + C_{Gf}\right) F_{410} x_2 = C_G F_{410} x_2 \tag{2.38}$$

where $C_G = C_{GCa} + C_{Gf}$ is the total concentration of GCaMP which is fixed.

The sensing gain and artifacts can be represented as a total system gain of $G = A_a \cdot A_S$. So, the measured signal (z) is:

$$z = z_1 + z_2 = Gy = Gy_1 + Gy_2 \tag{2.39}$$

$$z_1 = G\left(C_{GCa}F_{470,GCa} + C_{Gf}F_{470,Gf}\right) x_1 \tag{2.40}$$

$$z_2 = GC_G F_{410} x_2 \tag{2.41}$$

If in a period of time, the calcium concentration is constant ($C_{GCa} = C_0$), z_1 and z_2 are:

$$z_{1,0} = G\left(C_0 F_{470,GCa} + C_{Gf} F_{470,Gf}\right) x_1 \tag{2.42}$$

$$z_{2,0} = G C_G F_{410} x_2 \tag{2.43}$$

$z_{1,0}$ can be written as a function of $z_{2,0}$. From equation 2.43:

$$C_{Gf} = C_G - C_0 = \frac{z_{2,0}}{G F_{410} x_2} - C_0 \tag{2.44}$$

Substituting in equation 2.42

$$z_{1,0} = G\left(C_0 F_{470,GCa} + \frac{z_{2,0}}{G F_{410} x_2} F_{470,Gf} - C_0 F_{470,Gf}\right) x_1 \tag{2.45}$$

$$= \left(\frac{F_{470,Gf} x_1}{F_{410} x_2}\right) z_{2,0} + \left(G C_0 F_{470,GCa} x_1 - G C_0 F_{470,Gf} x_1\right) \tag{2.46}$$

If a linear regression model is fitted to $z_{2,0}$ against $z_{1,0}$, the slope m and intercept b of the model will be:

$$m = \frac{F_{470,Gf}}{F_{410}} \cdot \frac{x_1}{x_2} \tag{2.47}$$

$$b = G C_0 \underbrace{\left(F_{470,GCa} - F_{470,Gf}\right)}_{F'_{470}} x_1 = G F'_{470} C_0 x_1 \tag{2.48}$$

This model can scale z_2 (from equation 2.41) to the level of z_1.

$$z'_2 = m z_2 + b \tag{2.49}$$

$$= \frac{F_{470,Gf}}{F_{410}} \cdot \frac{x_1}{x_2} \cdot \left(G C_G F_{410} x_2\right) + G F'_{470} C_0 x_1 \tag{2.50}$$

$$= F_{470,Gf} G C_G x_1 + G F'_{470} C_0 x_1 \tag{2.51}$$

By subtracting z'_2 from z_1, the effect of unbound GCaMP can be removed from z_1.

$$\Delta z = z_1 - z'_2 \tag{2.52}$$

$$= G\left(C_{GCa} F_{470,GGa} + C_{Gf} F_{470,Gf}\right) x_1 - G F_{470,Gf}\left(C_{GCa} + C_{Gf}\right) x_1 - G F'_{470} C_0 x_1 \tag{2.53}$$

$$= G x_1 \left(C_{GCa} F_{470,GCa} - C_0 F'_{470} - C_{GCa} F_{470,Gf}\right) \tag{2.54}$$

$$= G x_1 \left(F'_{470} C_{GCa} - C_0 F'_{470}\right) \tag{2.55}$$

$$= G x_1 F'_{470} \left(C_{GCa} - C_0\right) \tag{2.56}$$

By dividing Δz by z_2', the effect of a varying system gain (G) will also be removed.

$$\frac{\Delta z}{z} = \frac{z_1 - z_2'}{z_2'} = \frac{GF_{470}' \left(C_{GCa} - C_0\right) x_1}{GF_{470,Gf} C_G x_1 + GF_{470}' C_0 x_1} \tag{2.57}$$

$$= \frac{F_{470}' \left(C_{GCa} - C_0\right)}{F_{470,Gf} C_G + F_{470}' C_0} = \frac{C_{GCa} - C_0}{C_0 + \frac{F_{470,Gf}}{F_{470}'} C_G} \tag{2.58}$$

$$\approx \frac{C_{GCa} - C_0}{C_0} \tag{2.59}$$

The approximation in equation 2.59 requires that :

$$C_0 >> \frac{F_{470,Gf}}{F_{470}'} C_G \tag{2.60}$$

$$\iff \frac{C_0}{C_G} >> \frac{F_{470,Gf}}{F_{470,GCa} - F_{470,Gf}} \tag{2.61}$$

$$\iff \frac{C_0}{C_G + C_0} >> \frac{F_{470,Gf}}{F_{470,GCa}} \tag{2.62}$$

If the fluorescence capability of GCaMP proteins bound to calcium is sufficiently larger than that of unbound GCaMP proteins, equation 2.62 is true. Under this condition, $\Delta z/z$ represents the deviation of calcium concentration from a reference value of C_0. This metric is not affected by variations in system gain which can be caused by SiPM gain changes and motion artifacts.

Note that $\frac{\Delta z}{z}$ is equal to $\frac{z_1}{z_2'} - 1$ which is $\frac{z_1}{z_2'}$ with a constant offset. This metric is similar to $\frac{|Z_1|}{|Z_2|}$ in equation 2.32. In the case of fiber photometry, scaling is required in order to remove the varying Ca-unbound GCaMP signal from the first channel.

2.4 Characterization

To evaluate and finalize the design, two sets of experiments were done. First, in order to compare the two correction schemes (bias monitoring and gain monitoring) characterization tests were done with a simplified system, using a function generator and data acquisition card instead of the AD5934s. In this simplified system, instead of fluorescence emission, an LED's output light was measured. These tests verified that the LED's output light can be detected and measured, and the signal amplitude can be calculated and corrected. Based on the results, the gain monitoring correction method was selected for further experiments.

In the second set of characterization tests, the fluorescence of fluorescent samples was measured, first using off-board electronic devices, and then using the on-board AD5934 chips in their stead. Performance of the two setups was compared. These tests verified the AD5934-based system's ability to measure fluorescence.

2.4.1 Characterization of the Simplified System

In the simplified setup, an LED, with an output wavelength range similar to GCaMP emission, was sinusoidally driven and its output light was measured. For the gain monitoring correction method, an additional LED was used as the control. The purpose of these characterization tests is to evaluate the system's ability to measure modulated light with the wavelength of interest. A 33522A function generator (Agilent, USA) was used to drive the LED(s) via the on-board TCA(s). A USB-6211 data acquisition device (National Instruments, USA) was used to acquire the output voltage of the TIA. The Fourier transform calculation and further data processing was done in MATLAB.

Two types of tests were conducted: 1. Stability Test and 2. Steps Test.

In Stability Tests, the main LED's driving current is a sinusoidal signal with a fixed amplitude and offset. The TIA output voltage is recorded. Signal-to-Noise Ratio (SNR), defined below, is calculated as a measure of variation in the output. A higher SNR means the recorded signal is more stable, indicating successful mitigation of artifacts. In equation 2.63, μ is the mean of output signal amplitudes calculated over a certain period of time, and σ is the standard deviation of these amplitudes.

$$SNR = \frac{\mu}{\sigma} \tag{2.63}$$

In Steps Tests, the LED's current (both amplitude and offset) increases by a certain amount over multiple steps each lasting a fixed amount of time. Contrast-to-Noise Ratio (CNR), defined below, is calculated between each two consecutive steps. The average CNR is used to evaluate how well the different steps are differentiated by the device. A higher CNR corresponds to a higher resolution.

$$CNR = \frac{|\mu_2 - \mu_1|}{\sqrt{\frac{1}{2}(\sigma_2^2 + \sigma_1^2)}} \tag{2.64}$$

These tests were done under three conditions: nominal conditions, in presence of a controlled thermal perturbation, and with motion artifacts. Note that all three include noise in the high voltage supply and ambient temperature variations. In this section, the setup for both correction schemes are described. The results of Stability and Steps Tests under the three conditions are presented. Comparing the results revealed that the gain monitoring method was more effective in mitigating artifacts.

2.4.1.1 Optics Setup

To assess the system's ability to measure low-power light at the wavelength of interest, the system was set up to measure the output light of a 516 nm LED, referred to as the main LED. A control LED with a wavelength of 560 nm was also used. In this setup, a beamsplitter passes and reflects a portion of the main and control LEDs' outputs respectively. As a result these portions of the LED output lights are combined into a beam that is incident on an SiPM (S13360-1375PE, Hamamatsu). This generate a photocurrent in the SiPM (Figure 2.14).

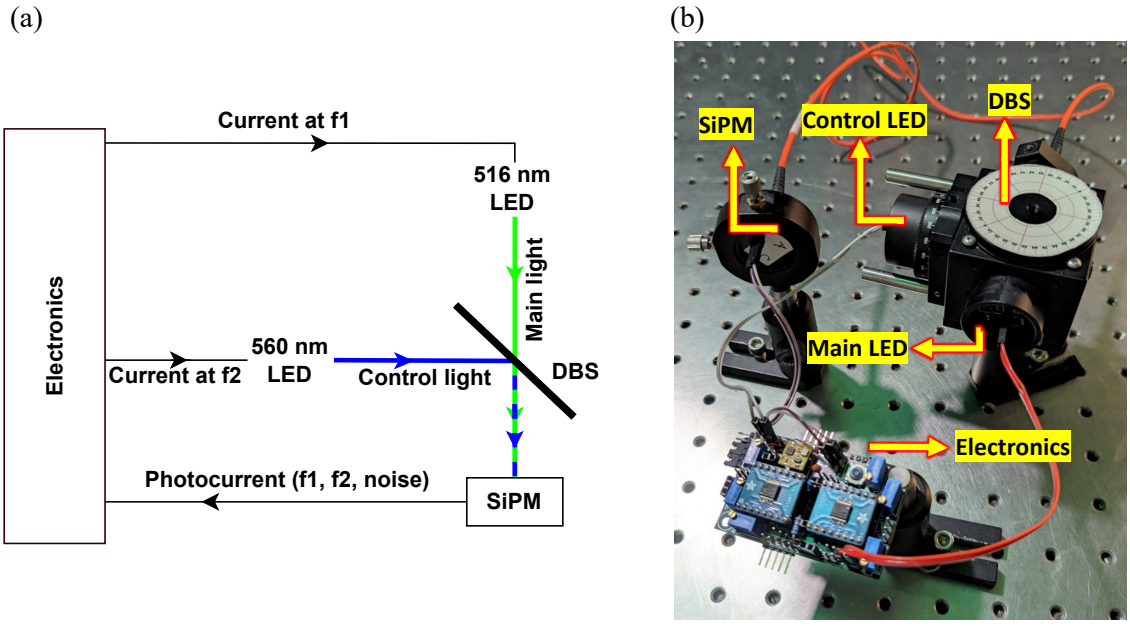

Figure 2.14: The optical setup for characterization tests (a) block diagram (b) photo of the setup.

2.4.1.2 Electronics

The AD5934s were switched to idle mode and disconnected from the TCAs. The TCAs were driven by a two-channel function generator (Agilent 33522A). DC voltage was used for optical power measurements, while sinusoidal voltages at 260 Hz and 290 Hz were applied to the main channel and control channel respectively for all other tests.

A NI USB-6211 data acquisition device was used to measure the voltage at the TIA output and the high-voltage supply output at a sampling rate of 10,000 SPS. The DFT of each 100 ms data segment (1000 samples) was computed in MATLAB, proving information in the 0 Hz to 5 kHz range with a frequency resolution of 10 Hz. The amplitude of the 260 Hz and 290 Hz signal components were determined based on the DFT calculation. Consequently, signal amplitude data was obtained at a rate of 10 SPS.

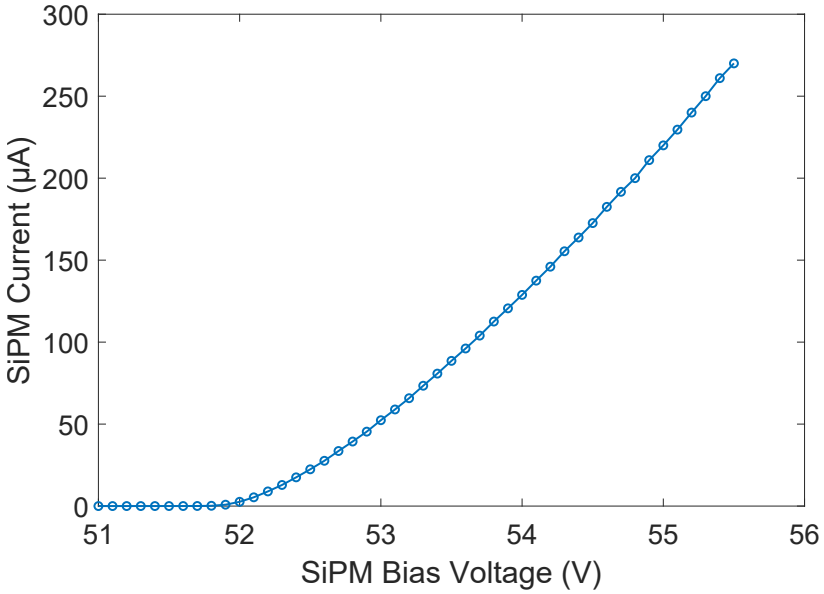

Figure 2.15: SiPM current with reference to its bias voltage while receiving a constant optical power.

2.4.1.3 Operating point

To observe the gain and break-down voltage of the SiPM, the main LED was driven to a fixed power. The SiPM was biased by a sourcemeter (Kiethley 236, USA) and the its current was measured at different bias voltages (Figure 2.15). The break-down voltage was observed to be approximately 51.9 V. The SiPM cathode voltage was set to 55.32 V by the high-voltage voltage source, while the anode voltage was set by the microcontroller's DAC. The choice of anode voltage was made based on a trade-off between SiPM gain and the TIA's output voltage swing. Lowering the anode voltage increases the SiPM gain, but it also limits the output voltage swing of the TIA. To balance these factors, an anode voltage of 2.71 V was selected, setting the SiPM bias voltage to 52.61 V, and allowing the TIA output to vary between 0 V and 2.71 V.

The LED output power at different driving voltages was measured by a S130VC detector and PM100USB powermeter interface (Thorlabs, NJ). Figure 2.16 shows the results. The main LED and the control must be driven to a maximum optical power of approximately 100 pW, to stay within the linear region. We selected a sinusoidal output light power with an offset and amplitude of approximately 50 pW as the operating point for both channels.

2.4.1.4 Bias Monitoring

Nominal Operation

For the stability test, the main LED was driven at the chosen operating point and the control LED was turned off. The TIA output and the attenuated bias voltage were recorded for 20 minutes. The last 1-minute

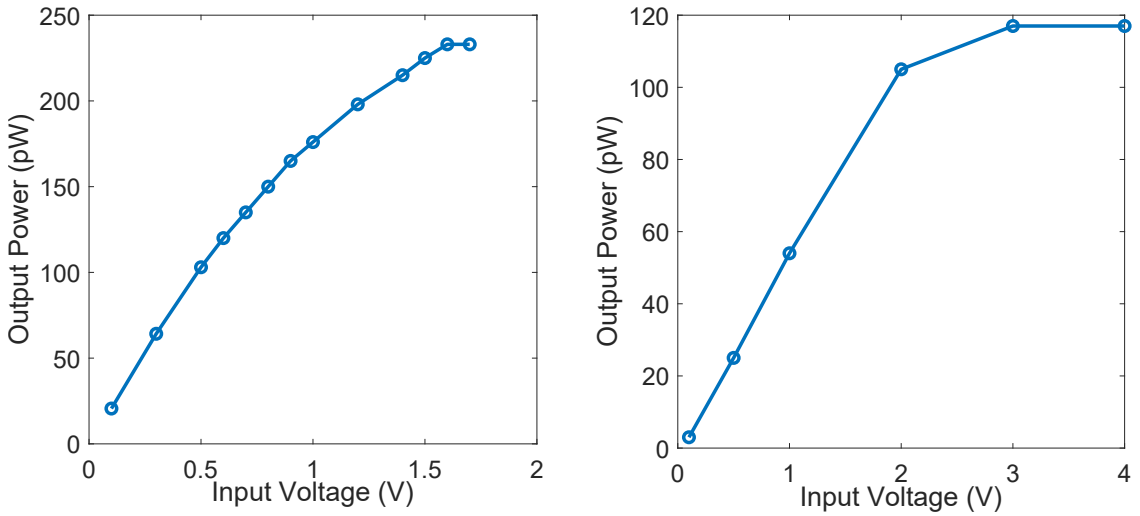

Figure 2.16: LED output optical power with reference to the TCA's driving voltage; (a) Main LED (b) Control LED

segment of the data was used to calculate the correction model parameters. An R^2 of 0.455 was obtained for the regression model. This model was used to correct the rest of the data. Figure 2.17 shows the output signal's amplitude before and after correction using the bias monitoring method. The SNR improved from 311 to 363 after correcting for SiPM bias variations.

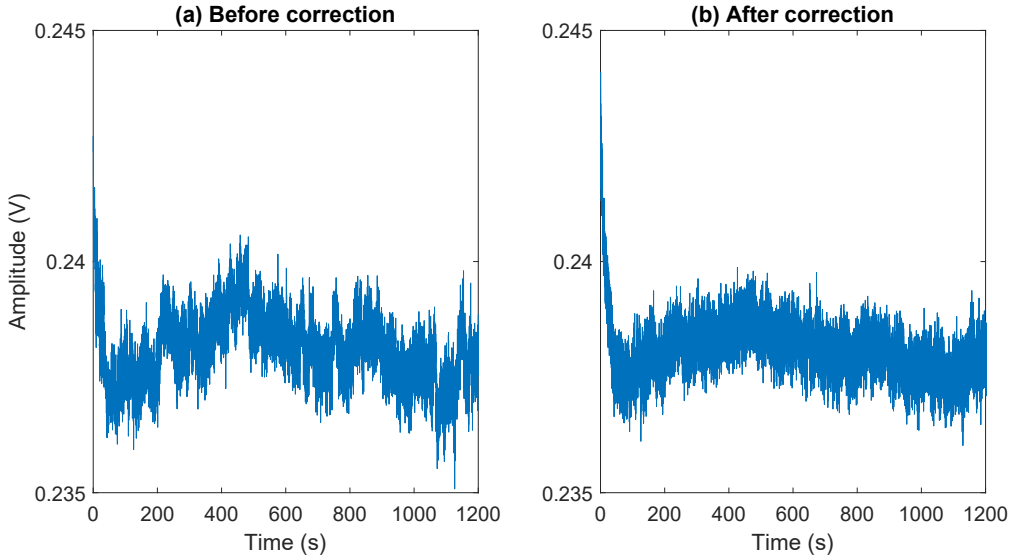

Figure 2.17: The TIA output in a 20-minute stability test using a single light source (a) before and (b) after correction using the bias monitoring correction scheme.

For the steps test, the driving voltage of the LED was changed in ten steps of 1%, from 95% to 105% of the operating point, each lasting 30 seconds. Figure 2.18 shows the results before and after correction. The average CNR was 3.47 and did not improve with correction.

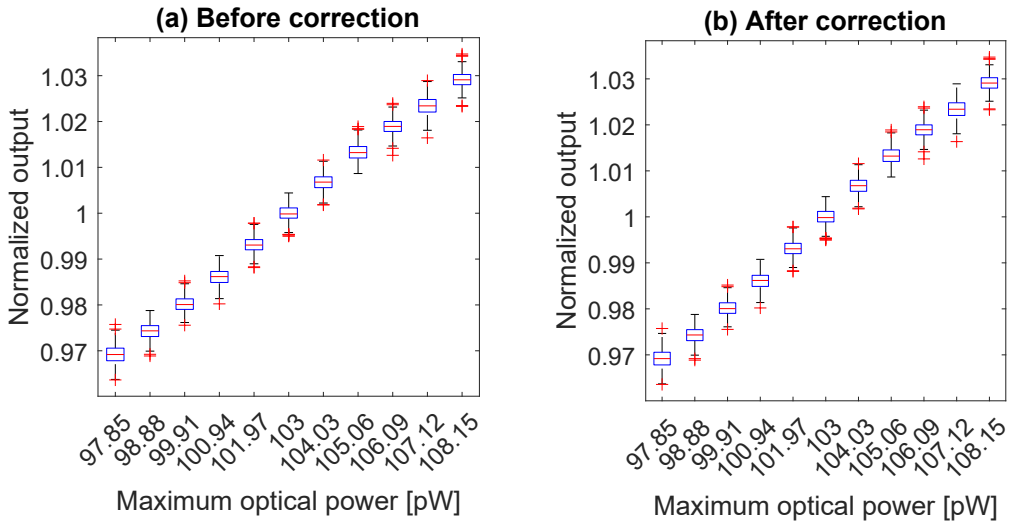

Figure 2.18: The TIA output in a Steps test using a single light source before and after correction using the bias monitoring correction scheme. The output amplitude was normalized to scale the mean at the operating point to one. Each box displays the median at the center, with the box edges indicating the 25th and 75th percentiles. Whiskers extend to non-outlier extremes, while outliers are marked individually with '+'. Outliers are data points that are greater than $q_3 + 1.5 \times (q_3 - q_1)$ or less than $q_1 - 1.5 \times (q_3 - q_1)$, where q_1 and q_3 are the 25th and 75th percentiles, respectively.

Temperature Change

A change in temperature can impact the SiPM gain. In order to observe the effect of temperature, an IRF510 MOSFET (Vishay Intertechnology, USA) was attached to the back of the SiPM board. The SiPM was heated by passing a 170 mA current through the FET for a duration of 750 ms, while the LED drive was kept constant. The resulting change in gain is illustrated in Figure 2.19 (a). A 60-second recording yielded an SNR of 65. No improvement in SNR was observed after correction. This was expected, because to correct for thermal variation, temperature sensing is required which was not implemented in this system.

A Steps Test was conducted with ten 60-second steps. During each step, the sensor temperature was increased in the same way. The result is shown in Figure 2.19 (b). The average CNR did not improve after correction.

Motion Artifacts

In order to mimic the effects of motion artifacts, the sensor mount was rotated for approximately 180 degrees, which caused the fiber to be pulled and moved. It was then returned to its initial position. This rotation was performed eight times in a period of 60 seconds. Figure 2.20 shows a stability test and a steps test under this condition. In the stability test, the SNR in a 60-second recording was 81. No improvement in the SNR was observed after correction. This was expected as the correction scheme can only correct for bias voltage

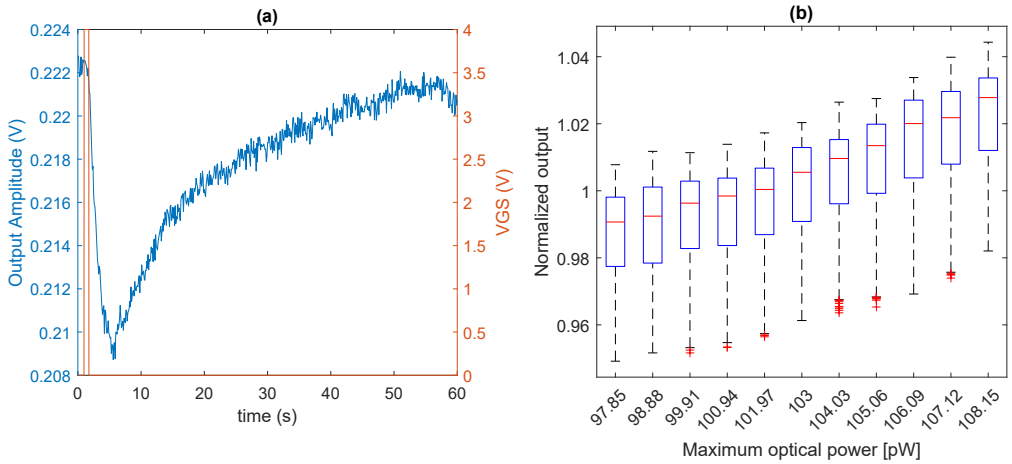

Figure 2.19: Effect of heat on the SiPM gain. (a) A 1-minute stability test using a single light source after correction using the bias monitoring correction scheme. During the period where VGS = 4 V, the FET is on and heating up the sensor. (b) A bias-corrected steps test while applying thermal perturbations to the sensor.

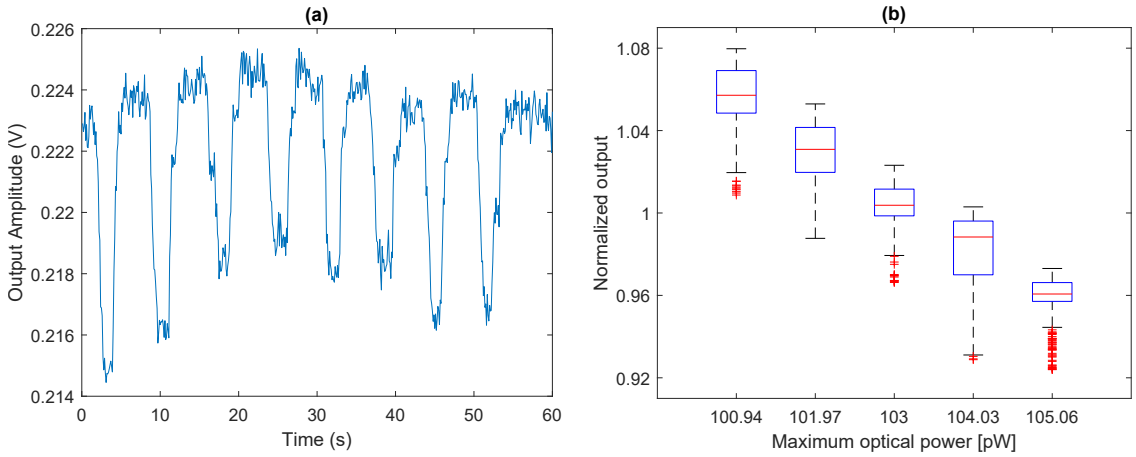

Figure 2.20: The effect of motion artifacts on the single light-source system output after bias-correction. (a) A 1-minute stability test. (b) A Steps Test.

variations. Figure 2.20 (b) shows a steps test with five 60-second steps. A negative CNR was observed, meaning that the system was not able to detect the increase in power in each step.

As demonstrated above, motion artifact and temperature changes limit the system's performance. As discussed in section 2.2, by adding a temperature sensor and monitoring and controlling the SiPM bias, the effect of temperature can be mitigated. However, this method cannot be used for motion artifacts.

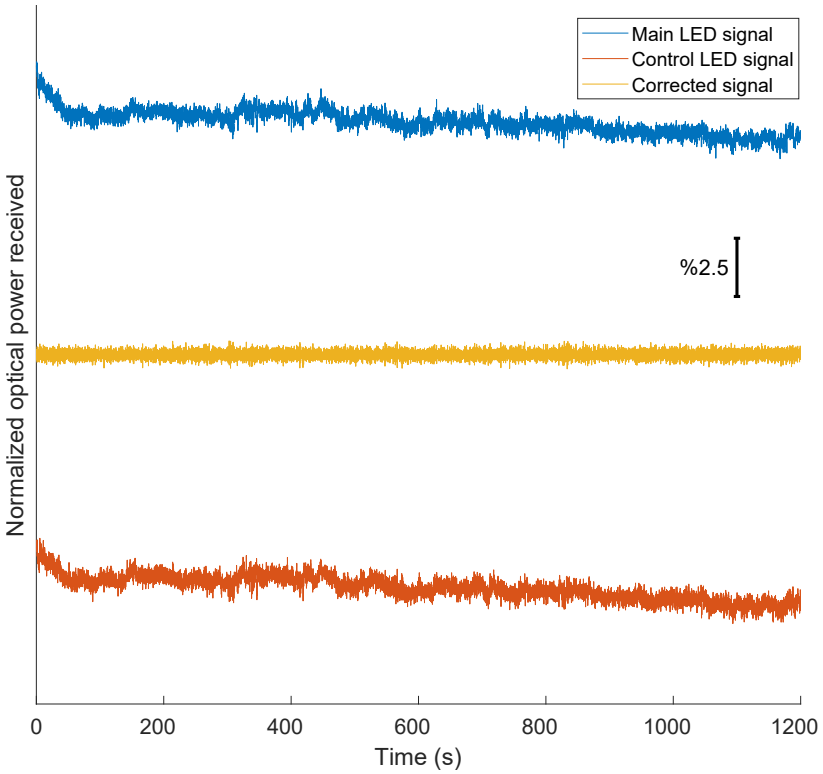

Figure 2.21: A 20-minute stability test using the gain monitoring correction method.

2.4.1.5 Gain Monitoring

Nominal operation

For the gain monitoring system, both LEDs were sinusoidally driven at the selected operating points. In this simplified system, there is no fluorescence and the measured light comes directly from LEDs. So, it can be modelled by the system shown in Figure 2.12. Therefore, correction can be done by simply dividing the first channel's signal by the second channel's signal.

Figure 2.21 shows a 20-minute recording of the output signals' amplitude. The SNR for the control channel, main channel and the corrected signal was 197, 190 and 468 respectively, showing a significant improvement with correction.

A steps test with ten 30-second steps was performed. Results are shown in Figure 2.22. Correction improved the average CNR from 2.53 to 3.02.

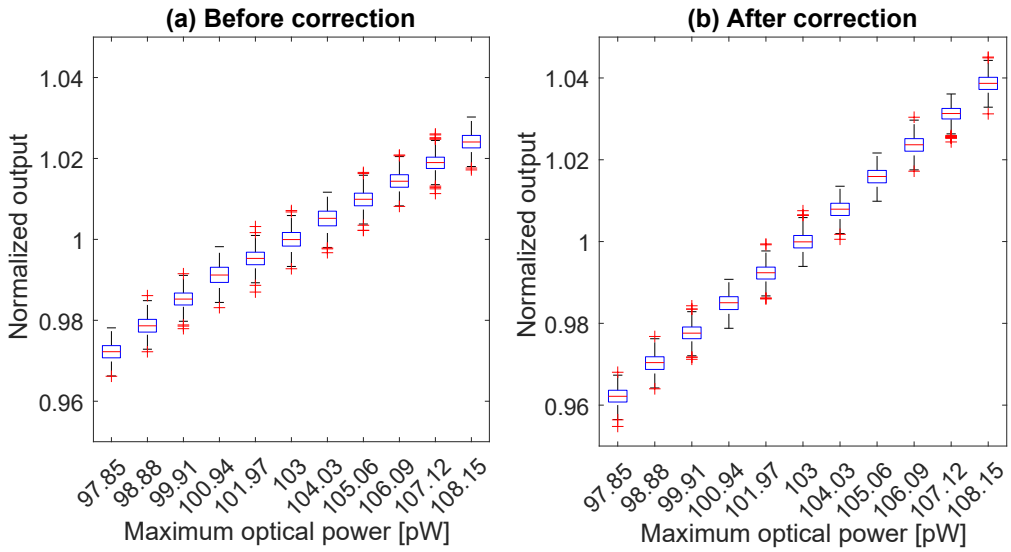

Figure 2.22: A steps test using the gain monitoring correction method.

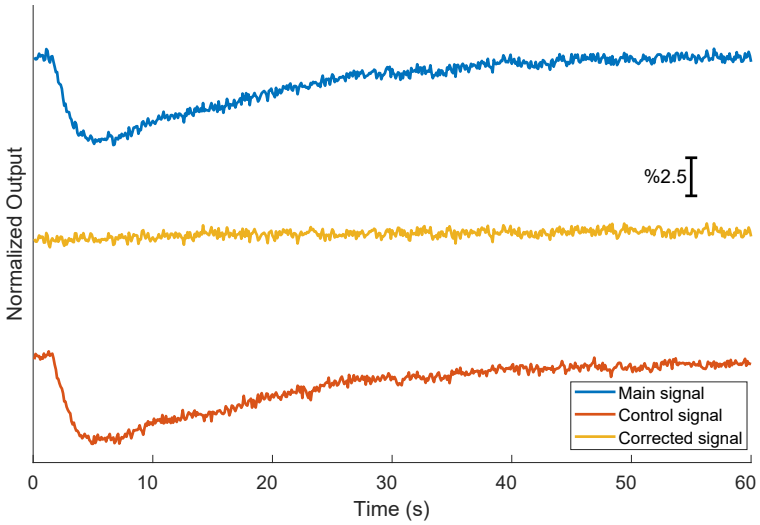

Figure 2.23: A 1-minute stability test using the gain monitoring method to correct for the effects of heat on SiPM gain.

Temperature Change

Similar to the previous section, the effect of a change in temperature on the system's gain was studied. In a one-minute recording at the operating point, correction improved the SNR from 59 to 368 (Figure 2.23). In a steps test, the CNR improved from 0.24 to 3.51 (Figure 2.24)

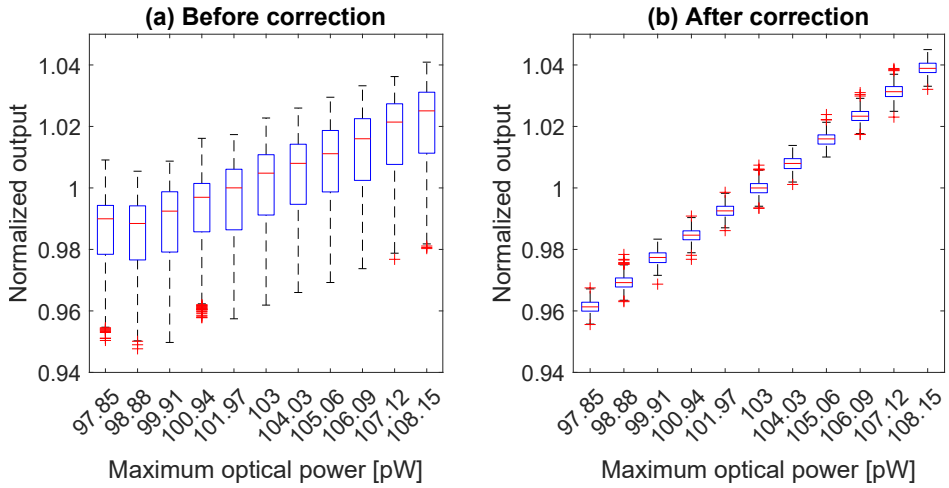

Figure 2.24: A steps test test using the gain monitoring method to correct for the effects of heat on SiPM gain.

Motion Artifacts

Motion artifacts were mimicked in a similar way to the previous section. Correction by gain monitoring successfully mitigated the motion artifacts. Results of a stability test and a steps test are illustrated in

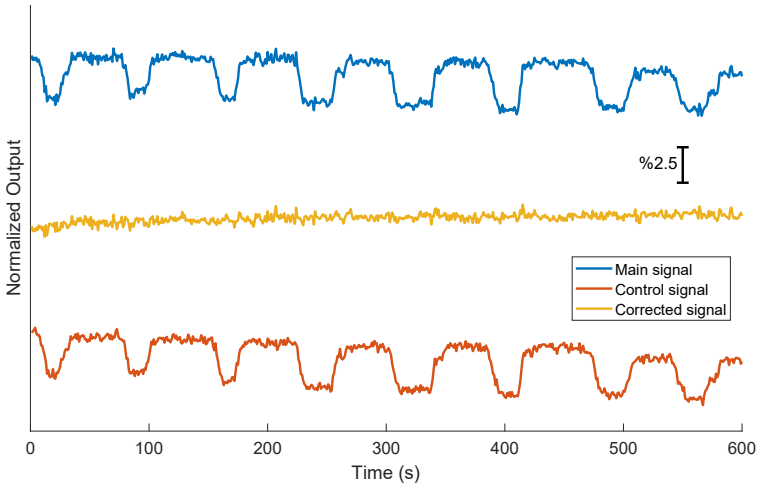

Figure 2.25: A 1-minute stability test using the gain monitoring method to correct for the effects of motion artifacts.

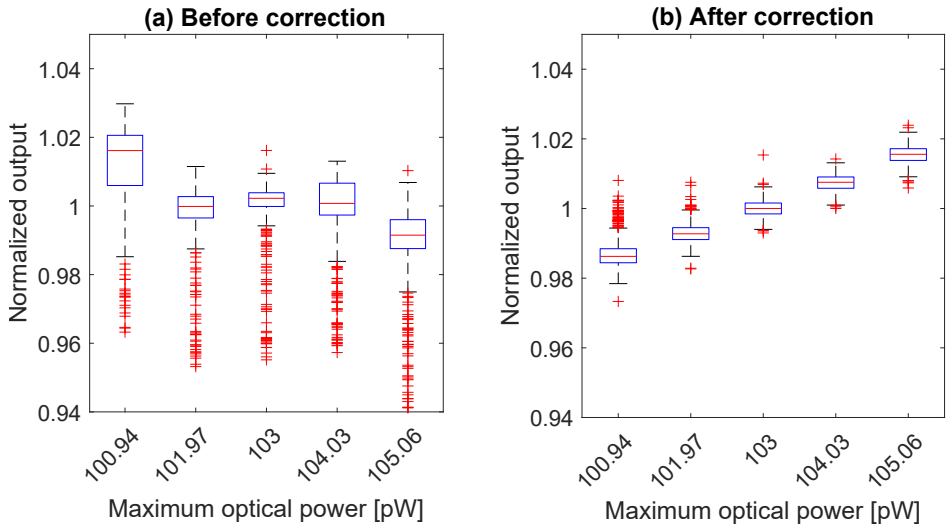

Figure 2.26: A steps test using the gain monitoring method to correct for the effects of motion artifacts.

Figures 2.25 and 2.26. In the stability test, correction improved the SNR from 71 to 315. In the steps test, CNR improved from -0.553 to 2.65.

2.4.1.6 Discussion

A simplified version of our fiber photometry system was implemented to evaluate its credibility and characterize the system. First, we selected an appropriate operating point for measurement of the output light intensity of a green LED. Then, a set of characterization tests were done to compare the two correction methods. These tests included stability and steps tests with and without the presence of thermal perturbations and motion artifacts. The results are presented in tables 2.1 and 2.2. Based on these results, it is evident

that the gain monitoring method is capable of compensating for multiple sources of variation simultaneously. Even in nominal operation, without introducing any additional artifacts, this method outperforms the bias monitoring method in terms of SNR.

The performance of the system deteriorates significantly in the presence of temperature changes and motion artifacts. In particular, when motion artifacts are present, a 1 percent increase in light level may be indistinguishable. However, the gain monitoring method is capable of correcting for artifacts, resulting in detectable changes.

These results indicate that the gain monitoring method offers better system resolution, precision, and accuracy. Therefore, this method was selected for the finalized system, and all subsequent experiments were conducted using gain monitoring.

Correction Method	Nominal operation		Heat		Motion	
	Raw	Corrected	Raw	Corrected	Raw	Corrected
Bias Monitoring	311	363	65.5	64.7	81.1	81.8
Gain Monitoring	190	468	58.6	368	71	315

Table 2.1: SNR in stability tests.

Correction Method	Nominal operation		Heat		Motion	
	Raw	Corrected	Raw	Corrected	Raw	Corrected
Bias Monitoring	3.99	4.22	0.393	0.384	-0.581	-0.648
Gain Monitoring	2.53	3.02	0.24	3.51	-0.553	2.65

Table 2.2: Average CNR in steps tests.

2.4.2 Characterization of the Fluorescence Measurement System

The fluorescence measurement optical setup, previously described in Section 2.3.4.2, was implemented. This setup was used to measure the fluorescence of fluorescein isothiocyanate (FITC) solutions in water. FITC has an excitation and emission spectrum similar to GCaMP without the Ca^{2+}-dependence.

To measure fluorescence, a patch cord was dipped in the samples to deliver the excitation light and collect the emission light. Stability tests using off-board devices (DAQ device and function generator) and the on-board AD5934 were performed. Results of a stability test with the two electronic implementations were compared. Once the AD5934-based implementation's functionality was validated, different concentrations of FITC were measured to demonstrate the device's sensitivity.

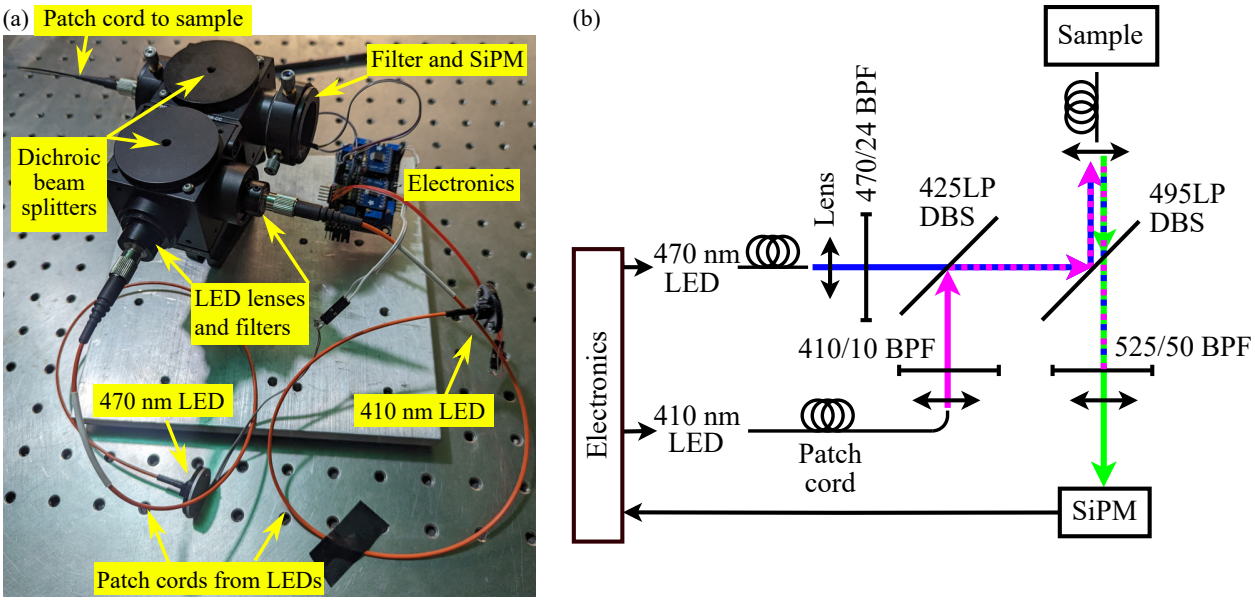

Figure 2.27: The fluorescence measurement setup; (a) a photo of the setup, and (b) the diagram of the optics.

2.4.2.1 System Setup

Figure 2.27 shows the implemented fluorescence measurement setup. The electronics shown in Figure 2.27 (a) is the PCB which includes the AD5934 chips. The diagram (b) is the same as the one in Section 2.3.4.2.

For both electronic implementations, similar to the previous tests, the SiPM bias was set to 52.61 V. The electronics were set to drive the 470 nm and 410 nm LEDs to maximum optical powers of 3.80 μW and 3.92 μW respectively. This power level was selected based on the SNRs obtained in a series of stability tests using the function generator and the DAQ device at different operating points where the fluorescence of a 0.25 μM FITC solution was measured (Table 2.3). As expected, the highest tested power resulted in the highest SNR. An SNR of 640 means the variation is less than 0.16 %, while the aim is to detect changes of 5%. The excitation power is also within the target range of 10 μW. Therefore, the highest optical power tested was selected for the following tests.

The concentration of FITC was selected based on initial tests using a commercial system by Doric Lenses. In a 0.25 μM solution, the fluorescence emission level was similar to that of a GCaMP-expressing mouse's brain in a fiber photometry experiment.

Note that in response to a 410 nm excitation, FITC has very low fluorescence, and the fiber's autofluorescence is dominant in the sample's emission (Figure 2.28). Therefore, in these characterization tests, correction mostly relies on the fiber autofluorescence at 410 nm excitation. Because the autofluorescence is weak, a relatively higher 410 nm excitation power is required comparing to fiber photometry experiments.

470 nm \ 410 nm power (μW)	0.75	1.80	2.86	3.92
0.70	142	130	118	104
1.73	365	363	353	333
2.77	351	544	552	478
3.80	399	569	629	640

Table 2.3: SNR after correction

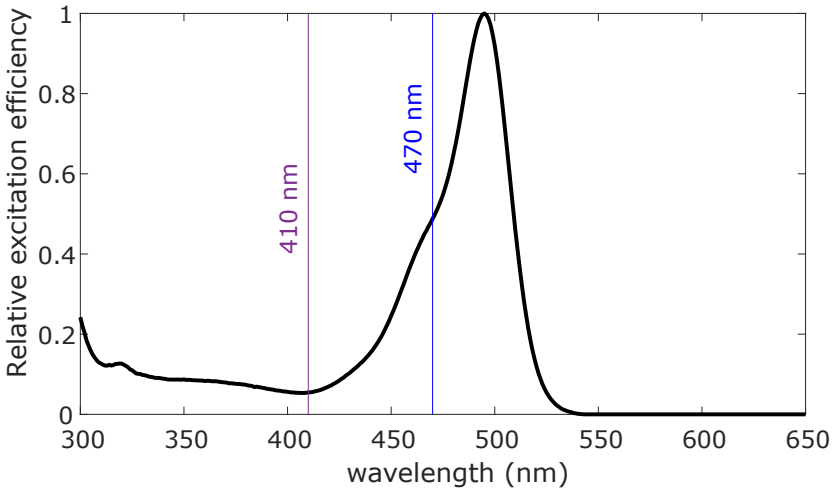

Figure 2.28: The excitation spectrum of FITC [64]. The relative excitation efficiencies at 410 nm and 470 nm are 5% and 43%, respectively.

2.4.2.2 Test Results

A one-minute stability test was done with both electronic implementations. Using the external devices, the SNR during a 1-minute recording of a 0.25 μM solution was 680 and 634 before and after correction respectively (Figure 2.29 (a)). In comparison, SNRs of 380 and 371 were observed before and after correction when using the on-board AD5934s (Figure 2.29 (b)). The external electronic device's showed a higher SNR. However, an SNR of 371 corresponds to a variation of 0.27% in the signal. This variation is well below the targeted resolution of 5%. Therefore, the AD5934-based implementation has an acceptable performance.

Although in the stability test, correction reduced the SNR, overall, correction improves the system's robustness to non-ideal conditions. To demonstrate, a one-minute recording using AD5934s with a thermal perturbation is shown in Figure 2.30. Here, correction improves SNR from 113 to 387.

To demonstrate the dynamic range of the system, six FITC solutions with concentrations of 6.25 pM to 0.4 μM were measured. The system output was scaled by a simple linear regression model to convert the numerical outputs to a concentration in micromolars. With a root mean square error 0.0027, the system output accurately measured the concentration of FITC in the 0.0125 μM to 0.4 μM range. The system's output for each concentration and the errors are shown in Figure 2.31 and Table 2.4. Note that there may

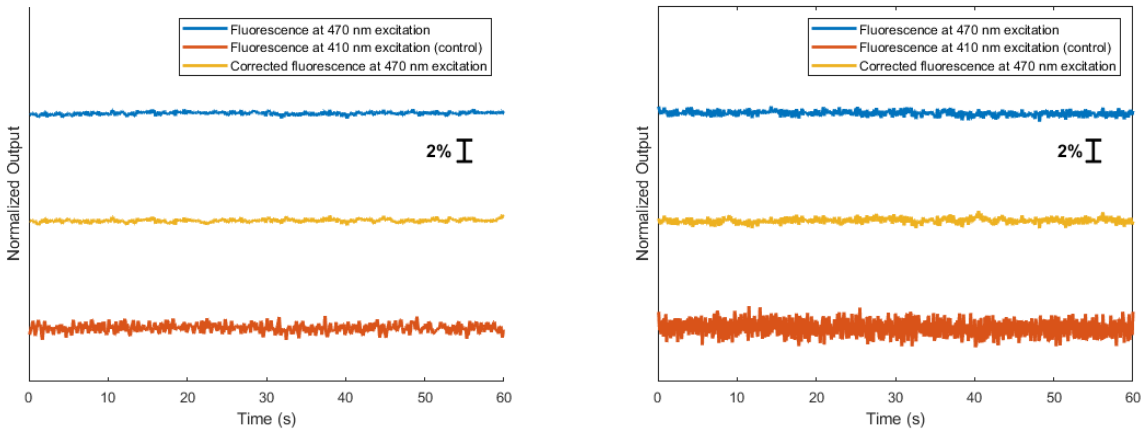

Figure 2.29: A 0.25 μM fluorescein solution measured for one minute by (a) a function generator and DAQ device (b) AD5934 chips.

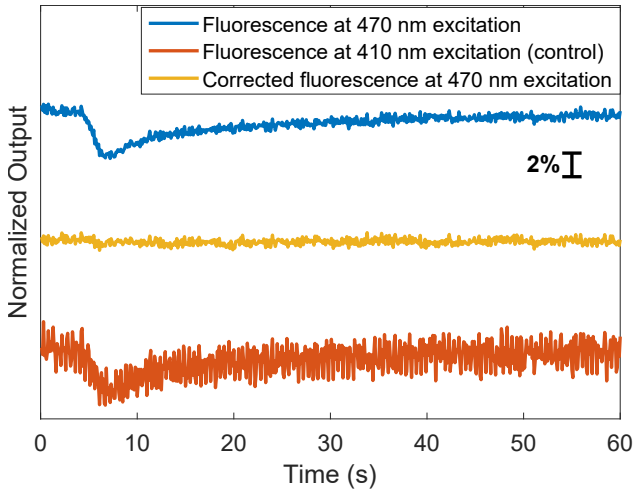

Figure 2.30: Compensation for temperature-dependent SiPM gain variation in the AD5934-based system.

have been errors in the solution preparation process and the actual concentrations may be different.

Sensitivity to small changes in fluorescence was evaluated by diluting a solution by 1% in four steps and measuring the fluorescence at these five concentration (Figure 2.32). The average CNR is these four steps was 4.3.

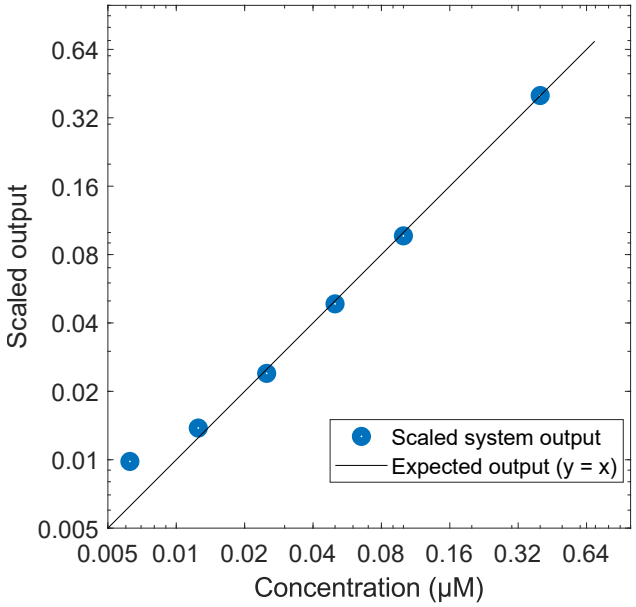

Figure 2.31: Six concentrations of fluorescein measured by the AD5934-based implementation.

Table 2.4: Concentration Measurements and Errors

Concentration (μM)	0.00625	0.0125	0.025	0.05	0.1	0.4
Measured Concentration (μM)	0.0098	0.0138	0.0240	0.0485	0.0967	0.4009
Error (%)	57.2520	10.2977	-4.0151	-2.9253	-3.2992	0.2259

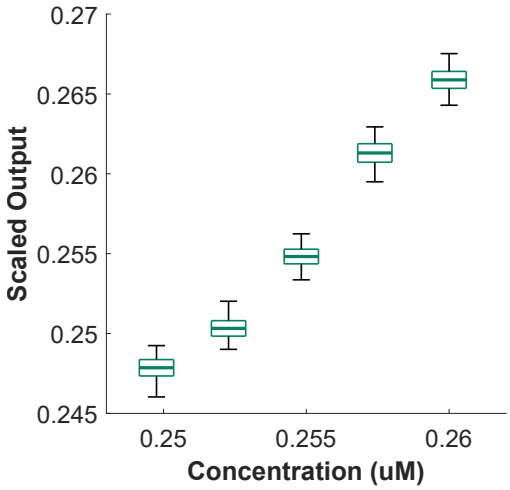

Figure 2.32: AD5934-based system's output when diluting a fluorescein solution in steps of 1% with a starting concentration of 0.26 μM. The mean, standard deviation, maximum, and minimum are shown by the boxplots [65].

2.4.2.3 Discussion

Fluorescence measurements were made using external devices for generating the excitation signals and acquiring the sensor data, and using the on-board AD5934 chips. The former resulted in a better SNR when measuring the fluorescence of a fluorescein solution. There are several factors affecting the SNR and sensitivity of the two implementations.

Firstly, the DAQ device has a 16-bit ADC with a 10 V range making the resolution 152 μV. In comparison, AD5934 has a 12-bit ADC. With a reference voltage of 5 V, the resolution is 1.22 mV. A lower ADC resolution, results in lower sensitivity. Additionally, the function generator output is more accurate and stable than the AD5934's excitation signal. Also, the AD5934's power consumption affects the supply voltage, causing slight changes in the electronics' biasing. These factors affect the device's accuracy and SNR.

Despite these limitations, the AD5934-based implementation can measure a wide range of concentrations and is sensitive to small changes in fluorescence which are similar to the changes of interest in $in-vivo$ fiber photometry experiments. The gain monitoring correction scheme is also effective in this implementation as demonstrated by a stability test in presence of a thermal perturbation.

2.5 Experiments

Two sets of in-vivo experiments were done in mice. In the first experiment, GGaMP was present in the mice's brain and stress-related neural activity was recorded. In the second set, a mouse was injected with a fluorescent dye, and the recorded signals provided information about blood flow in the brain. All animal procedures were approved by the University of Calgary's Animal Care and Use Committee.

2.5.1 GCaMP

Footshock experiments were conducted on three transgenic mice expressing GCaMP6f in neurons or astrocytes in the paraventricular nucleus of the hypothalamus, a brain region involved in stress processing. The experiments involved subjecting mice to footshocks, where they experienced 10 footshocks, each lasting 2 seconds and occurring every 30 seconds. These experiments were done over two sessions.

On day 1, the 470 nm and 410 nm LEDs in the AD5934-based device were driven to mean optical powers of 3.9 μW and 2.3 μW respectively. Recordings from mouse 1 and mouse 2 were collected during the footshock experiments, using the AD5934-based device. The correction model for each animal was calculated based on a section of the recording with no seeming neural activity. The resulting signals are depicted in Figures 2.33 and 2.34. The first peak in the corrected signal is due to picking up and transferring the animal

into the cage, while responses to footshocks are marked by the vertical grey traces.

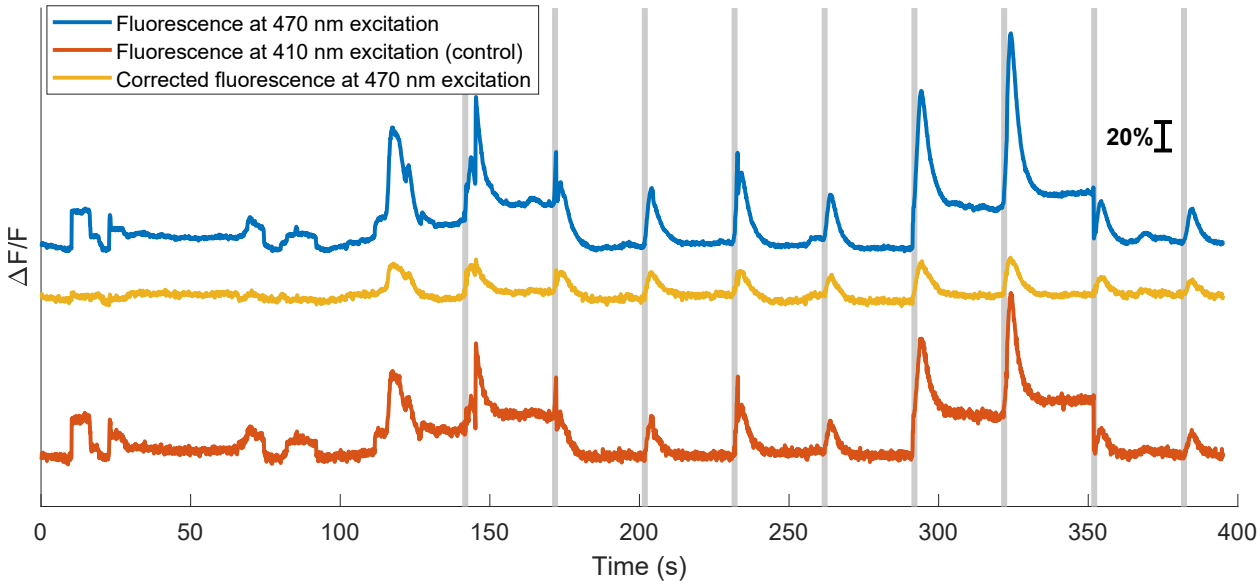

Figure 2.33: Mouse 1's footshock response recording by the custom setup on day 1 (3.9 μW 470 nm excitation).

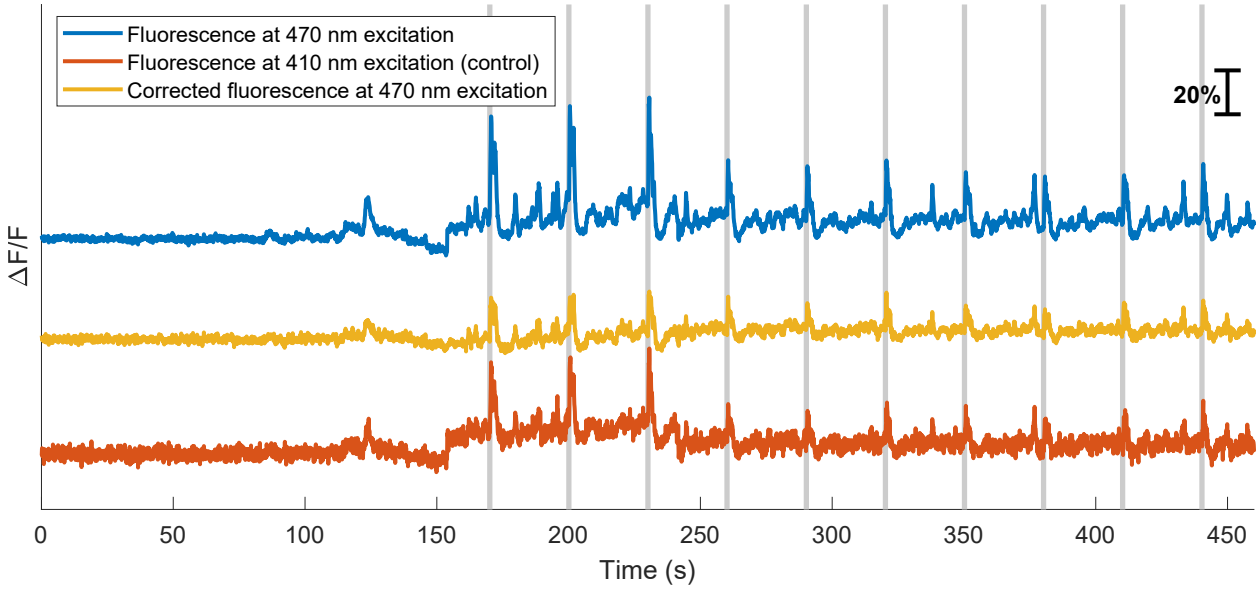

Figure 2.34: Mouse 2's footshock response recording by the custom setup on day 1 (3.9 μW 470 nm excitation).

On day 2, the same experiments were repeated on all three mice, once using the AD5934-based device and once using a commercial system (Doric Lenses, Canada). The excitation for the custom setup was set to a lower power level of 2.3 μW and 1.7 μW. The commercial system's power was set to 30 μW and 7.1 μW which is a typical level for these experiments. The signals were corrected as described earlier. The results

are shown in Figures 2.35 to 2.40.

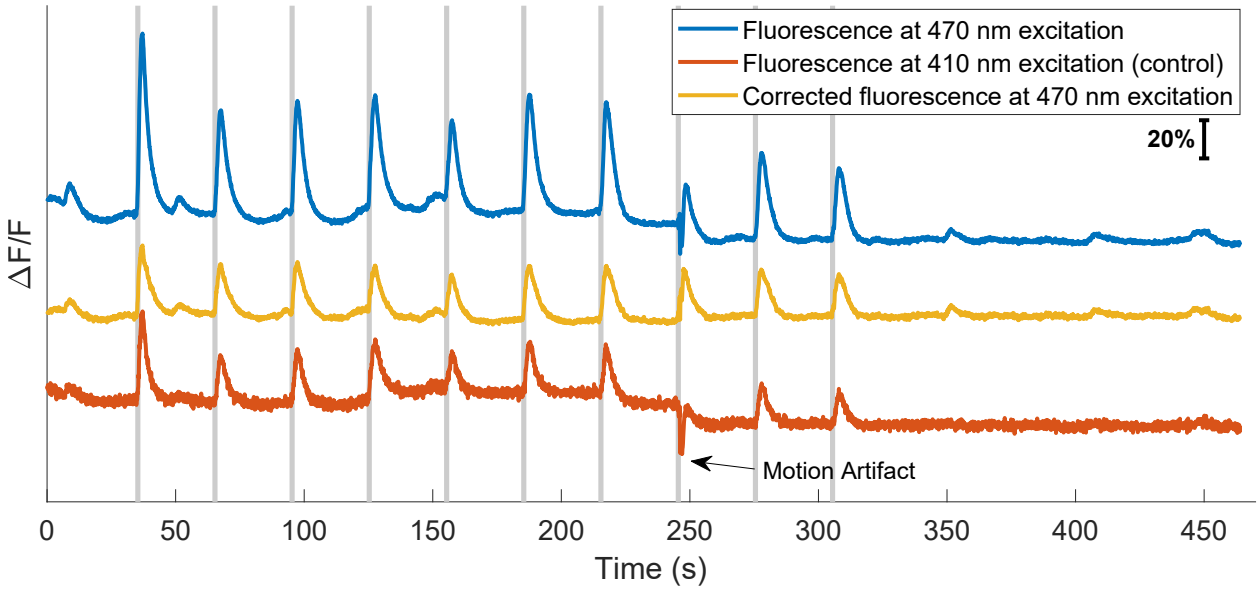

Figure 2.35: Mouse 1's footshock response recording by the custom setup on day 2 (2.3 μW 470 nm excitation). A motion artifact, eliminated by isosbestic correction is marked with an arrow.

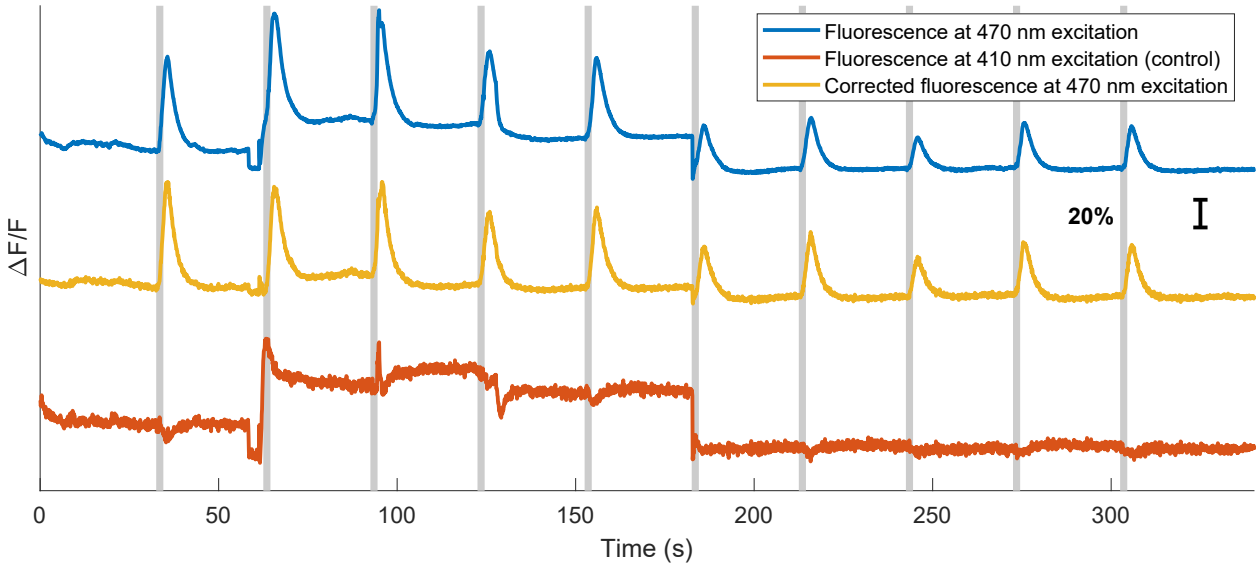

Figure 2.36: Mouse 1's footshock response recording by the commercial setup on day 2 (30 μW 470 nm excitation)

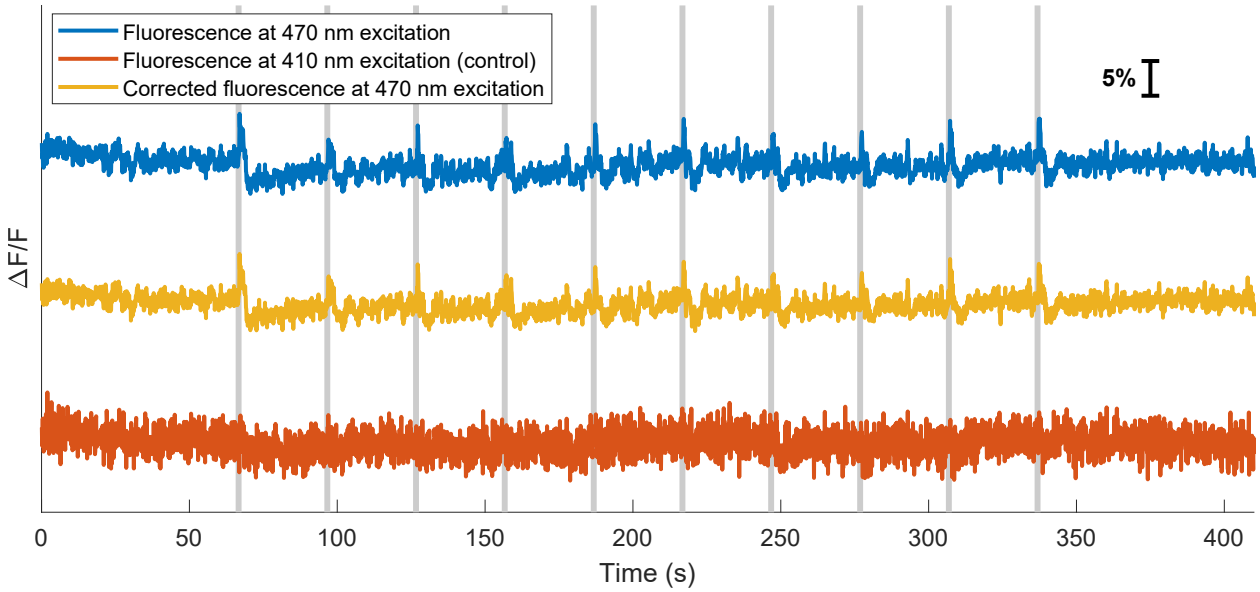

Figure 2.37: Mouse 2's footshock response recording by the custom setup on day 2 (2.3 μW 470 nm excitation).

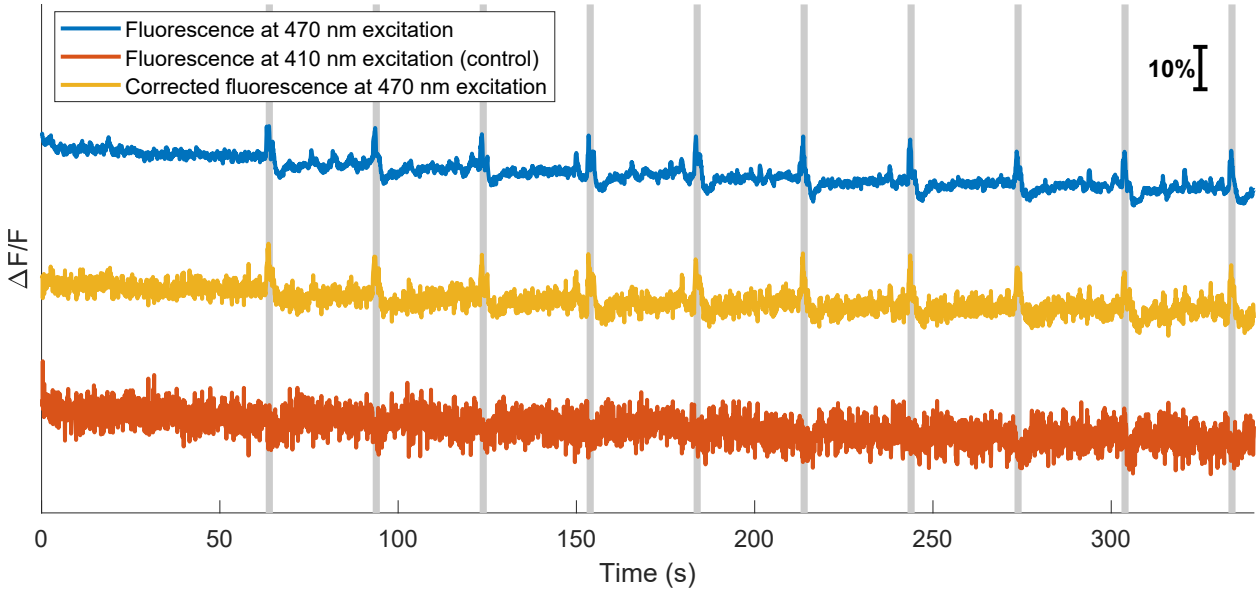

Figure 2.38: Mouse 2's footshock response recording by the commercial setup on day 2 (30 μW 470 nm excitation)

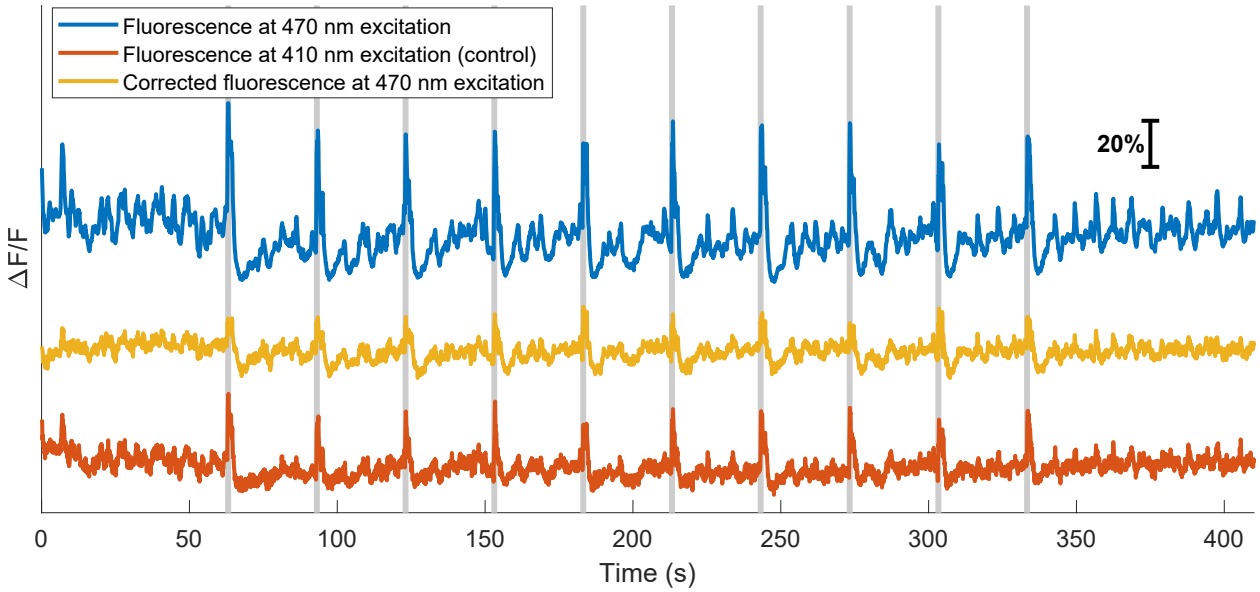

Figure 2.39: Mouse 3's footshock response recording by the custom setup on day 2 (2.3 μW 470 nm excitation).

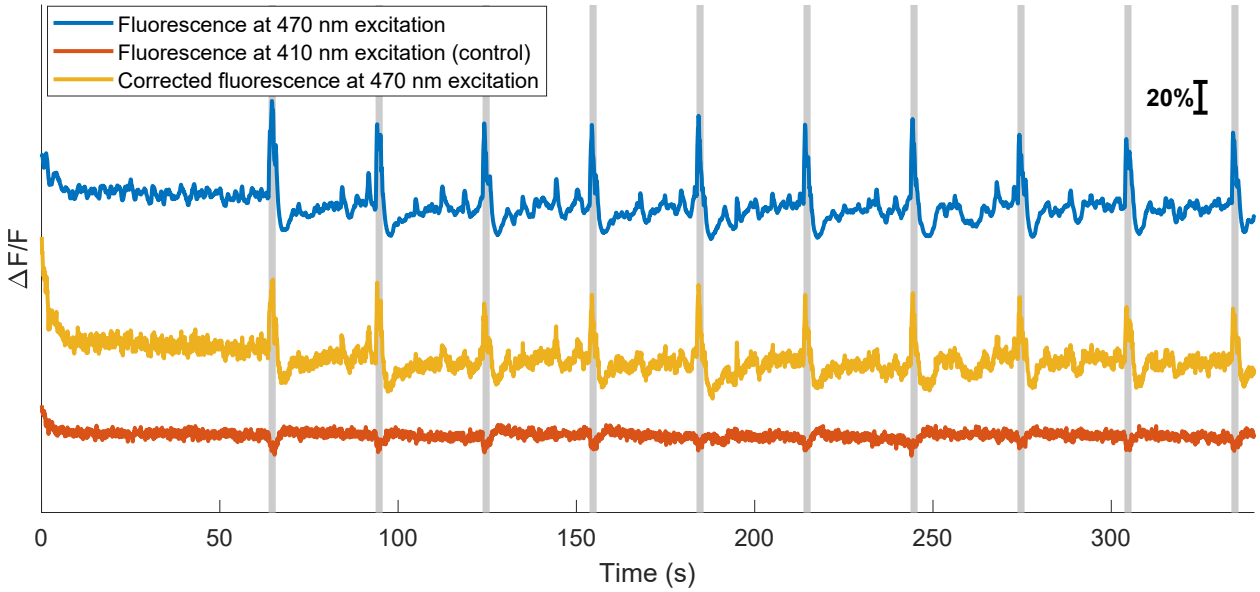

Figure 2.40: Mouse 3's footshock response recording by the commercial setup on day 2 (30 μW 470 nm excitation).

In these experiments, due to an oversight, the second channel's frequency was set to 280 Hz instead of 290 Hz. The Fourier transform spectral resolution in AD5934's calculations is ∼15 Hz. With the two channels' frequencies being only 20 Hz apart, crosstalk between the two channels is observed. That is why the footshock response appears on the second channel as well. This leads to overcorrection and reduced peaks in the $\Delta F/F$ signal. The next sections describes and experiement after correction the oversight.

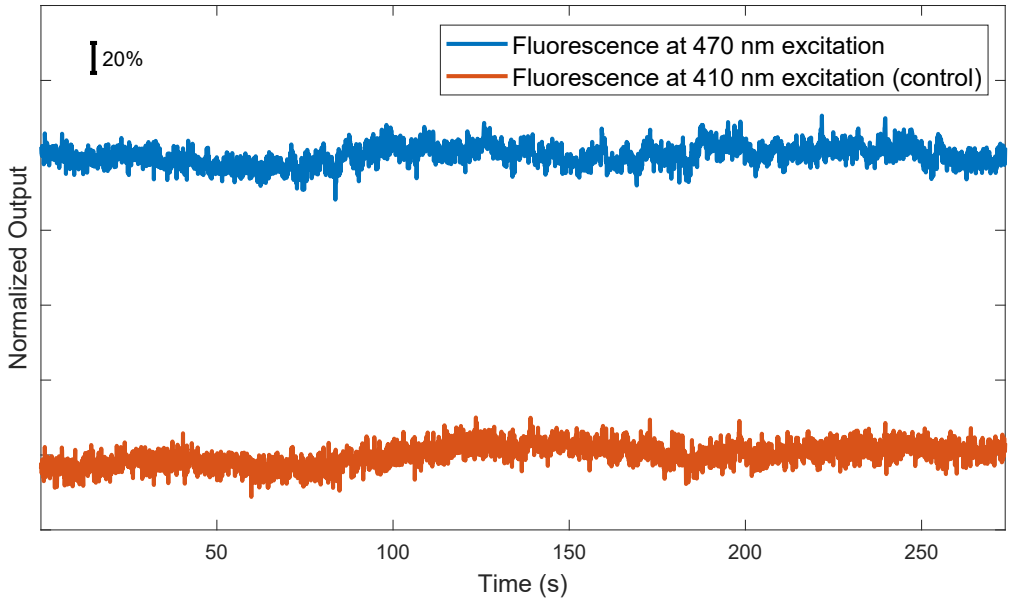

Figure 2.41: Baseline fluorescence recordings by our fiber photometry setup from the mouse with FITC before adminstering footshocks.

2.5.2 FITC

We initially intended to redo the experiment with the correct channel 2 frequency, but unfortunately, over time, the mice lost the neural activity dependent fluorescence response. This was confirmed with both our setup and the Doric system. Therefore, instead, a mouse was injected with a 5% fluorescein isothiocyanate-dextran (FITC-dextran) solution, allowing us to observe total regional blood volume within the paraventricular nucleus via fiber photometry.

The optical power in our setup was configured to 370 nW and 190 nW for the 470 nm and 410 nm excitations, while in the Doric system, they were set to 33.5 μW and 8.7 μW. Before applying footshocks, a 5 minute baseline recording was made to calculate a correction model. Afterwards, the mouse was placed in a footshock cage. Footshocks were administered every 30 seconds. While the mouse was the footshock cage, we alternated between the two setups, starting with Doric, then ours, and repeated this cycle three times. This alternating approach aimed to account for changes in the animal's response during the experiment. This was done to allow a fair comparison between the signal peak heights measured by the two systems.

Post-experiment analysis revealed clipping in the recorded signal from the Doric system. Therefore, this data was discarded. Figure 2.41 shows the baseline recording by our setup used to create the correction model. Figure 2.42 shows the fluorescence elicited by the 470 and the 410 nm excitation recorded by our setup during footshocks. These recordings suggest that the cross-talk between the two channels has been eliminated.

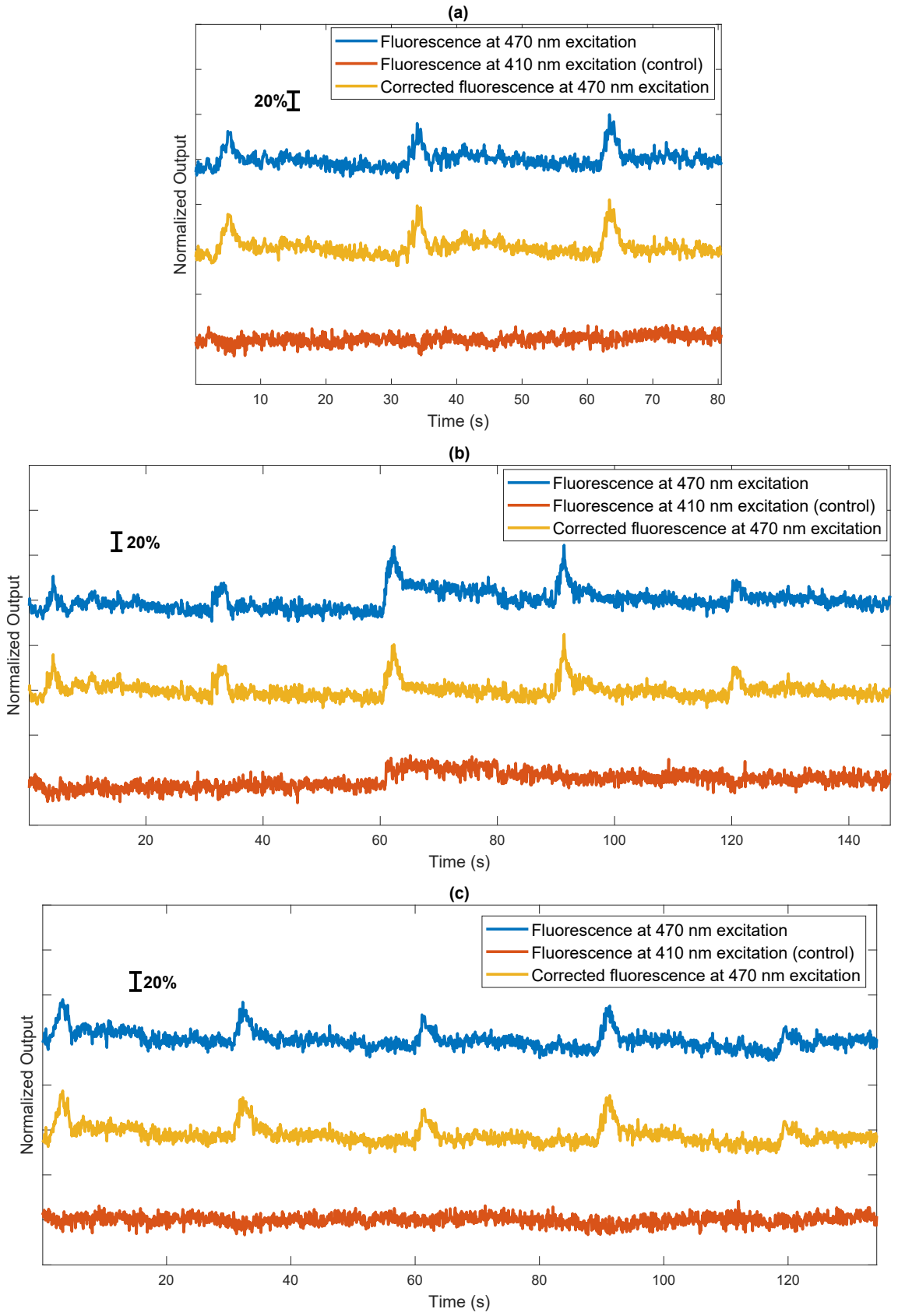

Figure 2.42: The footshock response of a mouse with fluorescein in its blood. Each plot shows a measurement from the same mouse in the three alternate recordings by our setup.

Table 2.5: Percentage increase in $\Delta F/F$ in response to footshocks in mice expressing GCaMP.

Setup	Mouse		
	1	2	3
Custom setup (3.9 μW excitation)	11-17	9-21	-
Custom setup (2.3 μW excitation)	21-37	4-7	9-18
Commercial setup (30 μW excitation)	28-76	8-11	34-50

2.5.3 Discussion

In the first set of experiments, the custom photometry setup was used for neural recordings during footshock experiments at two excitation power levels. To compare, these recordings were also made using a commercial setup by Doric Lenses. Overall, the commercial setup exhibited better sensitivity to neural activity, since over three animals, the increase in $\Delta F/F$ in response to footshocks was larger than that of the custom setup (Table 2.5). This is largely due to the crosstalk caused by the small difference between the two excitation frequencies.

Despite this limitation, our fiber photometry system was capable of detecting stress-related neural activity signals caused by footshocks. The corrected neural activity signal was similar to the one recorded by a commercial setup. The system also successfully mitigated motion artifacts. This is best evident in mouse 1's response shown in Figure 2.33.

The custom setup uses significantly lower excitation powers while still detecting the changes in $\Delta F/F$, comparing to the Doric setup. Also, a larger downwards drift in $\Delta F/F$ can be observed in the Doric system's recordings. This can be due to photobleaching caused by its high optical power.

The cross-talk issue was addressed in the experiments with the FITC-injected mouse. In these recordings, peaks in the second channel were eliminated. These recordings show promise that with the modifications, cross-talk between the channels is reduced and a larger $\Delta F/F$, similar to Doric system's measurements, may be obtained in neural recordings in mice expressing GCaMP.

2.6 Summary and Conclusion

This chapter presented the design, characterization, and validation an SiPM-based low-light fiber photometry system. First, background information on fiber photometry was provided. The system design was described in detail. Finally, characterization tests and *in vivo* experiment results were presented.

The system design consists of three main parts: electronics, optics, and signal processing. The optics setup is similar to a standard fiber photometry system, with the distinction that an SiPM is used as the photodetector. Using an SiPM allows us to use low optical excitation powers, without requiring high-voltage power supplies.

The electronics were implemented on a PCB, with two AD5934 impedance converters at its core. These integrated circuits simplify the system by generating excitation signals that are conditioned by op-amp circuits to drive two LEDs that excite a fluorescent sample. The impedance converters also measure the conditioned SiPM signal and extract its amplitude by calculating the DFT.

The AD5934s' readings are further processed in MATLAB. Processing includes correcting for SiPM gain variations, and extracting the $\Delta F/F$ signal. An SiPM's gain can be affected by variations in its bias voltage and temperature. Two methods for correcting for SiPM gain variations when detecting sinusoidally modulated light were explored. In the first one, its bias voltage was monitored and the system's readings were corrected to a certain bias level. In the second method, a second modulated light source was used to monitor the SiPM gain. The SiPM signal at the main channel's frequency was corrected using the signal component at the second channel's frequency.

Two sets of characterisation tests were carried out. First, with a simplified optical setup and electronics, the two SiPM gain correction methods were studied and compared. These tests showed that the gain monitoring method is as effective as the bias monitoring method. Additionally, the gain monitoring method can mitigate motion artifacts and can rely on isosbestic control in fiber photometry. Therefore, the gain monitoring method was incorporated into the finalized fiber photometry setup. Before *in vivo* experiments, the finalized setup was used to measure the fluorescence of multiple fluorescent solutions, to evaluate its resolution, dynamic range, and robustness to artifacts.

Finally, two sets of *in vivo* experiments were done. In the first set, neural signals in mice expressing GCaMP were recorded and compared to recordings from a commercial fiber photometry system. An oversight in the experiment led to lower $\Delta F/F$ signals in our setup due to cross-talk between channels. Despite this, our system successfully detected peaks in fluorescence in response to footshocks. The cross-talk was reduced in the second experiment where blood volume in a mouse's brain was measured via fiber photometry.

The main aim of this project was to develop a SiPM-based fiber photometry system for measurement of neural activity in mice. This objective was achieved in this research. The implemented system can operate on a 6 V power supply, can detect neural activity using optical excitation powers below 10 μW, and can correct for SiPM gain variations and motion artifacts. The system was able to detect 1% changes in the fluorescence of an FITC solution with a fluorescence similar to those observed in transgenic mice. Therefore, the system meets all the objectives of the project.

2.6.1 Future Work

Repeat Experiments on Transgenic Mice with Reduced Cross-talk: As mentioned earlier, because we did not have access to mice expressing GCaMP, we were not able to repeat the experiments using the intended excitation frequencies. These experiments must be repeated in order to confirm that the cross-talk between channels is reduced, and higher $\Delta F/F$ signals, similar to the commercial setup's recordings, can be obtained.

Optimize the SiPM Performance via Improved Biasing: In this work, the cathode voltage of the SiPM was kept constant and only the anode voltage was adjusted. The anode voltage was selected in order to provide sufficient voltage swing at the SiPM read-out TIA's output. Instead, the SiPM bias voltage can be set to maximise the gain to dark-count ratio. A configurable cathode voltage can allow for this optimization.

Use Lower Optical Excitation Powers: In the present research, conservative gain and power settings were used to provide a proof of concept for a SiPM and AD5934-based fiber photometry system. With modified SiPM biasing, it may be possible to detect neural activity using lower optical powers.

Increase Sampling Rate: In the present system, the AD5934 samples at least 17 periods of each signal which is more than what is required. If the clock frequency is increased by two times, the number of periods sampled will still be high enough to achieve accurate DFT calculations. This will come at the cost of higher power consumption. The AD5933 ADC is four times faster than the AD5934. Therefore, switching to the AD5933 can further increase the sampling rate.

Miniaturization: A more compact form factor could be beneficial for some applications. Firstly, it would improve portability and ease of use. Wearable miniaturized systems can open up possibilities for experiments in non-traditional settings where the animal is not confined to a small space. Based on the application, these advantages may justify implementing a compact and simplified system with an SiPM and the electronics integrated into a single chip.

Adapt for Multichannel Recording and Red Fluorescent Probes: Similar to GCaMP, RCaMP is a GECI used for monitoring intracellular calcium levels. However, its red fluorescent emission can be

advantageous in certain situations, such as when researchers want to simultaneously monitor different neural populations.

User-Friendly Interface: The current system offers a high degree of configurability, but its complexity might present challenges for researchers who prefer a more streamlined and user-friendly solution tailored to their specific needs. A user-friendly interface can be developed for the system that would allow researchers to configure the system via software, and process and visualize the data.

Chapter 3

Electrochemical Impedance Spectroscopy

3.1 Introduction

Electrochemical Impedance Spectroscopy (EIS) is a technique used in electrochemistry to study the electrical properties of electrochemical systems. It provides information about the interface between an electrode and an electrolyte by measuring impedance of a system in a range of frequencies. EIS has a variety of applications including studying batteries, fuel cells, and corrosion processes, monitoring biological interactions, and detecting biomarkers. EIS can be used in immunosensing to detect targeted antigens. In this work, we focus on EIS for immunosensing of cortisol antigens.

3.1.1 Motivation

Cortisol, a hormone synthesized by the adrenal cortex, is a significant biomarker, particularly for stress. Cortisol levels in different bodily fluids such as sweat, saliva, tears, urine and blood are increased by both acute and chronic stress. Chronic stress, as indicated by cortisol levels, impacts multiple physiological systems. Irregular cortisol patterns due to chronic stress are implicated in a range of health problems, including cardiovascular diseases, anxiety, depression, obesity, and disruptions in immune system function [66].

Beyond stress, cortisol is also connected to circadian rhythms that govern processes such as carbohydrate metabolism, glucose regulation, blood pressure, and immune function. Dysregulated cortisol secretion can give rise to disorders like Cushing's disease, characterized by excessive cortisol levels, or Addison's disease, characterized by insufficient cortisol production [66].

By monitoring cortisol levels, we can gain valuable insights into the repercussions of chronic stress on the body and its role in the development and management of conditions related to stress. Neurodegenerative diseases are an example of these conditions.

The relationship between cortisol levels and neurodegenerative diseases, specifically Parkinson's disease (PD) and Alzheimer's disease (AD), is a topic of ongoing research and interest. These diseases, characterized by a progressive loss of cognitive function and movement problems, have complex interactions with cortisol levels. Higher cortisol levels have been associated with AD, leading to brain atrophy and cognitive decline [67]. Similarly, PD patients exhibit higher cortisol levels than healthy individuals, suggesting a potential connection with the progression of motor symptoms and behavioral disorders [68]. However, these studies have limitations such as small sample sizes, limited longitudinal studies, and lack of standardized measurement instruments [67]. To achieve a more comprehensive understanding of the connection between cortisol levels and neurodegenerative diseases, a substantial volume of data collected over an extended period, involving a large participant pool, is essential.

The development of wearable cortisol monitoring devices is important for conducting comprehensive, long-term studies in this context. These devices should offer a non-invasive, continuous means of tracking cortisol levels in individuals over extended periods. These wearable devices will be essential in revealing potential relationships between cortisol, stress, and the progression of neurodegenerative diseases.

Various electrochemical sensors have been developed for cortisol detection. These sensors are read-out by electrochemical techniques such as cyclic voltammetry, differential pulse voltammetry, and impedance spectroscopy, among others. The focus of this chapter is an EIS read-out system for a cortisol immunosensor.

3.1.2 Aims

The primary aim of this research is to design an EIS system as a read-out for custom screen-printed electrodes (SPE) designed in the BioMEMS and Bioinspired Microfluidic Laboratory at the University of Calgary. The device should perform potentiostatic measurements, using the frequency sweep EIS technique, in a three-electrode configuration. The desired characteristics of the device are:

- Optimized for the measurement of cortisol samples. Based on previous experiments, the EIS excitation signal specifications were preselected as follows: frequency range of 1 Hz to 5 kHz, voltage amplitude of 15 mV, and offset of 170 mV.
- Compact, with potential to be modified as a wearable device for humans.
- Battery-powered, with the battery lasting for semi-continuous measurements throughout one day; that is, five measurements an hour during 24 hours.

- Capability of wireless data transfer
- Fast, with each measurement taking less than two minutes.

This device will be developed, and then characterized and validated. Characterization involves studying the device's dynamic range, accuracy and precision by measurements in RC cells. EIS capability will be validated on electrochemical samples containing different concentrations of cortisol. The device's ability to measure these samples will be compared to a commercial potentiostat.

3.1.3 Organization

In Section 3.2, background information for EIS is provided. First, the fundamental concepts of EIS are introduced, then notable previous research using EIS for cortisol detection are mentioned. In Section 3.3, the design specifics of our EIS device are described. Section 3.4 includes characterization of the described EIS system, and finally, Section 3.5 includes experimental results. The experiments include EIS measurements in SPE electrodes both with and without cortisol antibodies and antigens, using our device and a commercial system.

3.2 Background

3.2.1 Electrochemical Impedance Spectroscopy Fundamentals

Impedance spectroscopy (EIS) is a valuable tool in electrochemistry that offers insight into the characteristics of electrochemical cells and electrodes. In this technique, impedance at different frequencies is measured to analyze cell and electrode behavior. In these measurements, either the current through a cell is controlled while its voltage is measured (galvanostatic), or vice versa (potentiostatic). Benchtop galvanostats and potentiostats are the gold standard devices used in EIS [69]. The focus of this work is on the latter.

3.2.1.1 Current Flow in an Electrochemical Cell

An electrochemical cell consists of two or more electrodes submerged in an electrolyte solution. In an electrolyte, current flows via the movement of charged ions. At the electrolyte and electrode interface, a double layer, acting like a capacitor, forms. This double layer consists of charged ions attracted to the electrode surface and an opposing layer of counter-ions. When applying a voltage to an electrochemical cell, a portion of the current through the cell is associated with charging the double layer capacitance. In addition, there is a Faradaic current which involves the transfer of electrons between the electrode and the

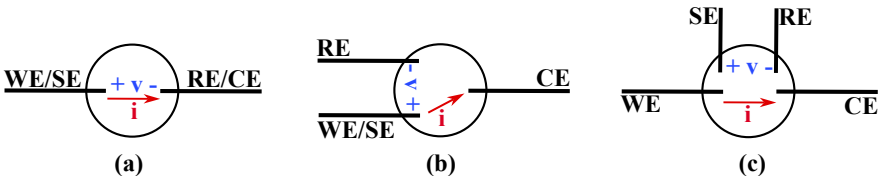

Figure 3.1: Electrode configurations for EIS. (a) 2-electrode system. (b) 3-electrode system. (c) 4-electrode system.

species in the electrolyte. The Faradaic current is typically the result of a redox reaction occurring at the electrode-electrolyte interface. The current flowing through the electrolyte, and therefore the impedance, is affected these electrochemical processes in the cell [69].

In biosensors, typically, a recognition element interacts with an analyte and consequently, the behavior of the sensor is affected. If the impedance is affected, by performing EIS, the analyte can be detected. These recognition elements include, but are not limited to, enzymes, antibodies, nucleic acids, and aptamers [70].

3.2.1.2 Electrode Configuration

EIS can use several electrode configurations, shown in Figure 3.1. The simplest electrode configuration used in EIS is the 2-electrode setup. In this electrochemical system, there are two electrodes: the working electrode (WE) and the counter electrode (CE). A certain voltage is applied across the two electrodes, and the current between them is measured. Because of the electrochemical reactions occurring at both electrode surfaces and the current flowing between them, it is challenging to precisely control the voltage in this setup. In some cases, the impedance of the electrical connections to the electrodes cannot be ignored.

A more common setup is the 3-electrode system. In this configuration, an additional reference electrode (RE) is used, and the voltage is applied across WE and RE instead. RE is a stable electrode with no current flowing through it. All of WE's current passes through CE instead, and this current is measured. The CE voltage can vary with different values of current, but this will not affect the WE voltage with reference to RE [71].

In a 4-electrode system, in addition to WE, RE, and CE, another electrode called a working sense electrode (WS or SE) is used. In this setup, the voltage between the SE and RE can be controlled, while the resulting current through CE or WE is measured. This setup is not as common as the previous one but has specialized applications. In the 4-electrode mode, measurement focuses on processes involving the solution and barriers, such as a membrane, between the sense and reference electrodes. However, it does not provide information about electrode surface reactions [72].

3.2.1.3 Potentiostatic Measurement Techniques

A potentiostat is a device that is capable of applying a voltage across two of its terminals, and measuring the current flowing through another terminal. Potentiostats are used in various electrochemical techniques including impedance spectroscopy. A typical commercial potentiostat has four terminals that can be used in an appropriate configuration for each of the aforementioned systems. For instance, in a 3-electrode system, the potentiostat's SE and WE terminal are both connected connected to the working electrode in the electrochemical cell [71].

To measure impedance at different frequencies, different types of excitation signals have been used. The most common one in EIS is a series of sinusoidal voltages at different frequencies. In a typical EIS experiment, a potentiostat applies a small AC voltage on top of the sample's open-circuit potential (OCP) to the electrodes. OCP is the potential difference existing between the electrodes when no current flows through the solution. The resulting current within the cell is then measured by the potentiostat. The amplitude and phase of this signal are calculated to determine the impedance at the specific frequency. This can be done by calculating the Fourier Transform of the signal [71].

Another method is to use an excitation signal containing a range of multiple frequency components. This signal can be a step function, white noise, or a well-defined multi-sine. The different frequency components of the resulting current are extracted by calculating the Fourier transform. Simultaneous measurement of impedance at different frequencies allows for a faster measurement. However, this results in a lower signal-to-noise ratio [73].

3.2.1.4 Equivalent Circuits

The electrical behavior of electrochemical cells can be modeled by equivalent electrical circuits. While all cells are not best modelled by the same circuit, the Randle's equivalent circuit is the most common one (Figure 3.2 (a)). In this circuit, the solution resistance, through which all current must pass, is represented by a series element (R_Ω). i_c and i_f represent the double-layer charging current and the Faradaic current, respectively. The relation of these currents with the applied voltage is modeled by C_d and Z_f, where C_d is the double layer capacitance and Z_f is models the Faradaic current's effect. Faradaic currents cannot be modelled perfectly with linear circuit elements. However, it is sometimes simplified to a resistor (R_s) and capacitor (C_s) in series (Figure 3.2 (b)). The impedance is often presented in a Nyquist plot with each point representing impedance at one frequency (Figure 3.2 (c)). The horizontal and vertical axes show the real and imaginary part of the impedance. As shown in equation 3.4, if Z_f only consists of a resistor (R_s), the Nyquist plot is a semicircle with a radius of R_s.

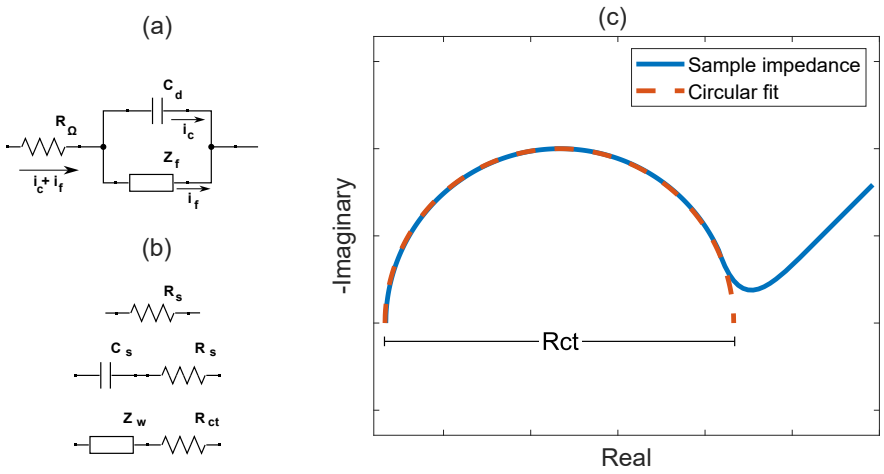

Figure 3.2: (a) Randle's equivalnt circuit. (b) Circuit models for the Faradaic process. (c) Example of a Nyquist plot of an electrochemical sample. R_{CT} is the diameter of the fitted semi-circle.

$$Z = R_\Omega + (\frac{1}{j\omega C_d} \parallel R_s) = \left(R_\Omega + \frac{R_s}{1+(\omega R_s C_d)^2}\right) - j\frac{\omega R_s^2 C_d}{1+(\omega R_s C_d)^2} \tag{3.1}$$

$$\mathrm{Re}\{Z\} = R_\Omega + \frac{R_s}{1+(\omega R_s C_d)^2} \tag{3.2}$$

$$\mathrm{Im}\{Z\} = -\frac{\omega R_s^2 C_d}{1+(\omega R_s C_d)^2} \tag{3.3}$$

$$(\mathrm{Re}\{Z\})^2 + (\mathrm{Im}\{Z\} - R_\Omega)^2 = R_s^2 \quad , \quad R_s \,\&\, C_d > 0 \tag{3.4}$$

In many cases, a portion of the impedance Nyquist plot appears as a straight-line segment at the end of the semicircle in the high-frequency region. This segment is called the Warburg tail, and the Warburg element is defined to represent this behavior (Figure 3.2 (b) and (c)). In equation 3.5, Z_W is the Warburg element's impedance, and ω and A_W are the angular frequency and the Warburg coefficient respectively. In these cases, the Warburg element and a series resistor called the Charge Transfer Resistance (R_{CT}) represent the Faradaic process. In R_{CT}, CT refers to the charge transfer that occurs at the electrode-electrolyte interface during electrochemical reactions. R_{CT} can provide valuable information about surface reactions, and possibly the concentration of an analyte [69].

$$Z_\mathrm{W} = \frac{A_\mathrm{W}}{\sqrt{\omega}} - j\frac{A_\mathrm{W}}{\sqrt{\omega}} \tag{3.5}$$

In immunoassays relying on EIS, antibodies are immobilized on the surface of a sensor. If antigens are present in the sample, they will bind to the antibodies. A higher concentration of antigens corresponds the more antigen-antibody pairs on the sensor surface. This process affects the reactions at the electrode-

electrolyte interface, and in turn increases R_{CT}. Therefore, by determining R_{CT}, the antigen concentration can be determined [74]. R_{CT} is approximately equal to the diameter of the semicircle appearing in the impedance Nyquist plot. To extract R_{CT} from EIS measurements, a circle can be fitted to the data points in the section of the Nyquist plot where the Warburg effect is not present.

3.2.2 Electrochemical Impedance Spectroscopy for Cortisol Detection

Some common cortisol detection methods include electrochemical, fluorescence, colorimetric, and surface plasmon resonance (SPR) assays [75–80]. Electrochemical measurements, in particular, offer several advantages, and among them, Electrochemical Impedance Spectroscopy (EIS) stands out as a powerful and versatile technique for cortisol detection.

EIS can offer high sensitivity, enabling the detection of cortisol molecules at concentrations down to the picogram per milliliter range [81, 82]. Low limits of detection (LOD), makes EIS well-suited to the precise quantification of cortisol at small concentrations. Additionally, EIS can provide rapid response times, facilitating real-time continuous monitoring of cortisol levels which is essential for the dynamic tracking of cortisol throughout the circadian cycle. Furthermore, due to reduced reagent usage, costs and resource consumption are minimized. Lastly, the simplicity of electrochemical sensors and their read-out electronics make them a versatile and accessible choice for miniaturization and point-of-care applications. Along with small sample volume requirements, this characteristic makes them suitable for wearable applications [75].

A substantial body of research has focused on the application of commercial desktop and benchtop EIS devices along with novel sensors for cortisol measurement. These studies have explored various electrode materials, immobilization molecules, sample types and volumes, concentration ranges, and excitation signal ranges in EIS. Cortisol has been measured in multiple media such as interstitial fluid, synthetic and human sweat, human serum, saliva, whole blood and tears. Various excitation levels and frequency ranges have been used for EIS, which are optimized for the particular sample, sensor, and experimental conditions. These studies have demonstrated the effectiveness of EIS as a robust cortisol detection method [81–86].

In order to gain insight into the implications of cortisol levels on health, continuous monitoring of cortisol concentrations is essential. Therefore, developing wearable electronics tailored to specific applications is a subject of interest. Sweat is an excellent choice for wearable long-term continuous cortisol monitoring applications. It offers a non-invasive and convenient method to collect a biofluid that contains cortisol and can provide insights into long-term stress patterns. Only a limited number of standalone wearable cortisol sensing devices have been developed. The most notable ones which have been developed in recent years, are mentioned below.

In 2019, Rice et al. introduced a cortisol measurement device in the form of a wristwatch. It was used for continuous monitoring of cortisol levels. To transfer data, the device is plugged into a computer. The device uses an interdigitated electrode design as the sensing platform. Using a sample volume of 5 μL, cortisol concentrations between 8-151 ng/mL were measured [87].

Torrente-Rodriguez et al. designed a wearable wireless sensing device for cortisol, published in 2020. The compact device can be placed on subjects' bodies for sweat sampling and in-situ cortisol recognition. The device is battery powered and can conduct 330 minutes of continuous measurements. It was used for continuous monitoring with a sample volume of less than 10 μL. The concentration range measured was 0 to 5 ng/mL [88].

Churcher et al. developed a portable sensing device that uses aptamers to detect biomarkers in human sweat. EIS was performed within the frequency range of 10-100 Hz. Data transfer to a computer was done via a USB connection. The device was used for continuous monitoring of Neuropeptide Y (NPY) and cortisol levels in human sweat using a microfluidic sensor with a sample volume of 2 μL. The range of measured concentrations for both analytes was 1-256 ng/mL [89].

Wang et al. created a wearable aptamer-field-effect transistor sensing system that can monitor cortisol levels in sweat. The device is in the form of a wireless smartwatch, incorporating a microfluidic module and a liquid crystal display (LCD), and flexible electronics. The device comes with a smartphone graphical user interface where the user can change the device operational mode and store and display data. The device was used for continuous monitoring in human subjects. To collect sweat, the subject's forearm was iontophoretically stimulated [90].

Cortisol sensing platforms are being developed by the BioMEMS and Bioinspired Microfluidic Laboratory at the University of Calgary. This includes a wearable microfluidic patch for sweat collection [91]. Custom functionalized screen-printed electrodes (SPE) are used in an immunoassay to detect cortisol. A similar sensor developed by the group has also been described [92]. The purpose of this work is to develop miniaturized electronics for the cortisol immunosensor read-out.

3.3 Design

3.3.1 Overview

The impedance measurement circuit, pictured in Figure 3.3, was designed and implemented as a 3.42×3.34 cm PCB. The circuit is battery-powered and wireless. The board features three switches that control its modes and functions: an on/off switch, a 2/3 electrode mode switch, and a calibration/measurement switch. With

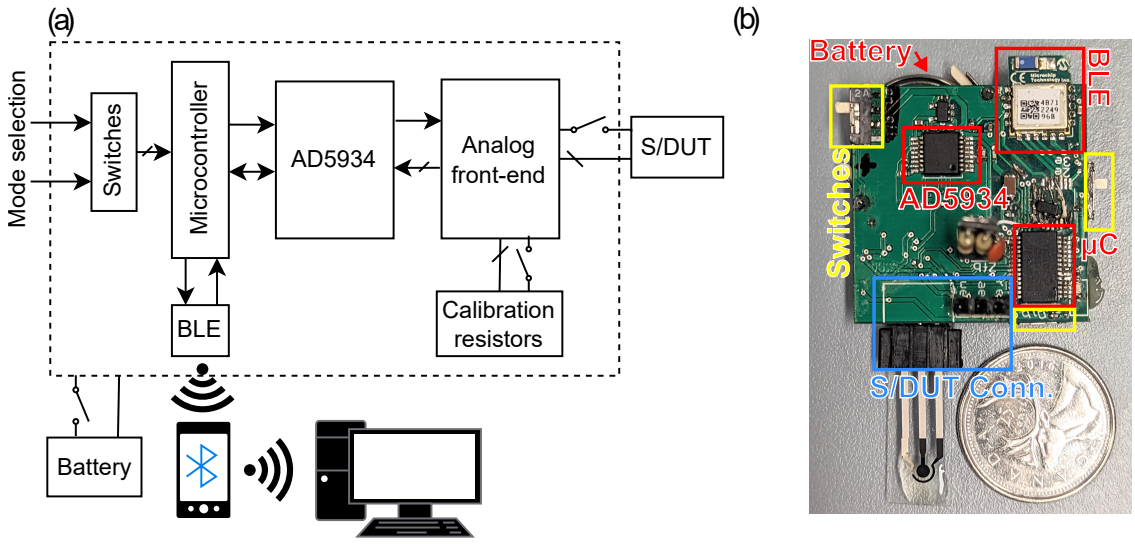

Figure 3.3: The impedance measurement device. (a) Block diagram. (b) A photograph of the circuit board. μC is short for microcontroller, and S/DUT Conn. shows the connectors for samples or devices under test.

these switches, the system can be configured to operate in three modes: one for calibration and two for impedance measurements. The impedance measurement modes include a 2-terminal mode for RC cells and a 3-terminal measurement mode for EIS. In calibration, six scans are completed to measure the impedance of on-board resistors as a reference for subsequent measurements. In the two measurement modes, impedance of an external sample or device under test (S/DUT) is measured in a single scan. For EIS, a flat flexible connector (FFC) is included for screen printed electrodes to be inserted and connected to the circuit. Socket headers are also available to insert a DUT or access the terminals for testing.

To initiate a scan, the user first sets the switches according to the desired mode. Upon powering on, the measurement process begins. In each scan, the impedance of a device, sample, or an on-board calibration resistor is measured at seven fixed frequencies. After completion, an LED indicator lights up to signal the availability of data. The user then establishes a BLE connection between a client device (here, a smartphone) and the circuit (host). The host device then transfers its data to the client device. After data transfer, the host terminates the BLE connection, at which point the circuit enters sleep mode to conserve power. For subsequent measurements, the user must power cycle the device.

Data received by the phone is sent to a PC to be further processed in MATLAB. In calibration mode, the data is saved to be used as a reference for subsequent measurements. When used for EIS, the charge transfer resistance (R_{ct}) can be extracted from the impedance data received.

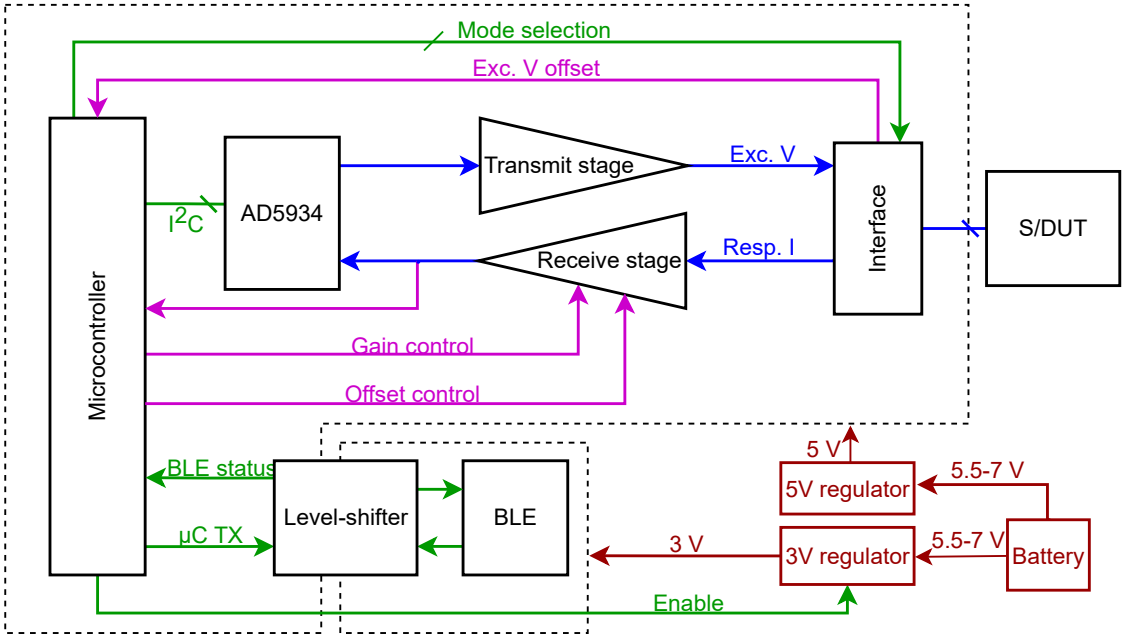

Figure 3.4: Block diagram of the EIS circuit.

3.3.2 Electronics

The main blocks of the electronic circuit are illustrated in Figure 3.4. The AD5934, controlled by a microcontroller, generates a sinusoidal voltage that is conditioned by the transmit stage to provide a excitation voltage. The excitation voltage is then applied to the S/DUT or calibration resistors via an interface circuit, based on the operation mode. Before the scan begins, this voltage is measured by the microcontroller and the applied offset voltage is adjusted if needed. The current through the sample or device is then converted to a voltage and amplified by the receive stage. The output of this stage is monitored and its gain is adjusted if necessary. This signal is then input to the AD5934 for impedance calculation. The microcontroller then reads the AD5934's data and transfers it to the BLE module. Two regulators, powered by two CR2025 coin cells, provide the power supply for this circuit. A 3-Volt linear regulator powers the BLE module while a 5-Volt linear regulator powers everything else. In this section, each part of this design is described in detail.

3.3.2.1 Microcontroller

A 16-bit PIC24FV16KM202 microcontroller (Microchip, AZ) was programmed to communicate with the AD5934 through the I^2C protocol in order to set the measurement parameters, initiate the measurement, and read out the resulting data. After reading the AD5934 data, the microcontroller sends it to a RN4871 BLE module (Microchip, AZ) via UART, and then turns the module off. Additionally, the microcontroller sets the operation mode of the circuit based on the state of the mode switches. This is done by controlling a

single-pole four-throw (SP4T) and a single-pole double-throw (SPDT) analog switch in the interface circuit. The microcontroller also manages the gain selection and offset control process, and controls the charging of capacitors in the receive stage. The interface and gain control are describes in Sections 3.3.2.4 and 3.3.2.5.

3.3.2.2 Transmit Stage

The transmit stage conditions the excitation voltage generated from the AD5934 and applies it to the S/DUT. The selection of the excitation voltage level and frequencies was made in alignment with the requirements and standards outlined by our collaborators in the BioMEMS and Bioinspired Microfluidic Laboratory for the intended EIS measurements. The selected excitation signal is a 30 mV_{pp} sinusoidal voltage with an offset of 170 mV at seven frequencies between 1 Hz and 5 kHz. This voltage should be applied across the WE and RE.

Following these requirements, the AD5934 generated sinusoidal voltages at seven frequencies in proximity of seven logarithmically-spaced frequencies between 1 Hz and 5 kHz. These frequencies were selected so that the 1024-point data over which DFT is calculated comprises integer multiples of the excitation period. Details for the selected excitation frequencies are included in Table 3.1.

Table 3.1: Timing details for impedance measurement.

AD5934 Clock Frequency (Hz)	**ADC Sampling Rate (sps)**	**Buffer Fill Time (ms)**	**Excitation Frequency (Hz)**	**Number of Periods Sampled**
8000000	119218	8.589	4880	41.91
8000000	119218	8.589	1160	9.96
2000000	29804.48	34.36	291	10.00
500000	7451.12	137.4	65.50	9.02
125000	1862.78	549.7	16.40	9.02
31250	465.70	2198.9	4.090	8.99
7812.5	116.42	8795.5	0.909	8.00

The transmit stage consists of a band-pass filter. For measurement at each frequency, the AD5934 generates a sinusoidal voltage with an offset of 298 mV and amplitude of 330 mV_pp. One MCP6422 op-amp (Microchip, AZ) in a dual package is configured as multiple feedback band-pass filter, with a bandwidth of 120 mHz-40 kHz, and passband gain of 0.1 (Figure 3.5). The AD5934s output is input to this band-pass filter. The filter's output is a sinusoidal voltage with an amplitude of approximately 30 mV_{pp} and an offset 2.0 V. The choice of the offset voltage is explained in Section 3.3.2.4. This voltage is applied to one terminal of the sample/device-under-test (S/DUT) by an interface described in Section 3.3.2.4.

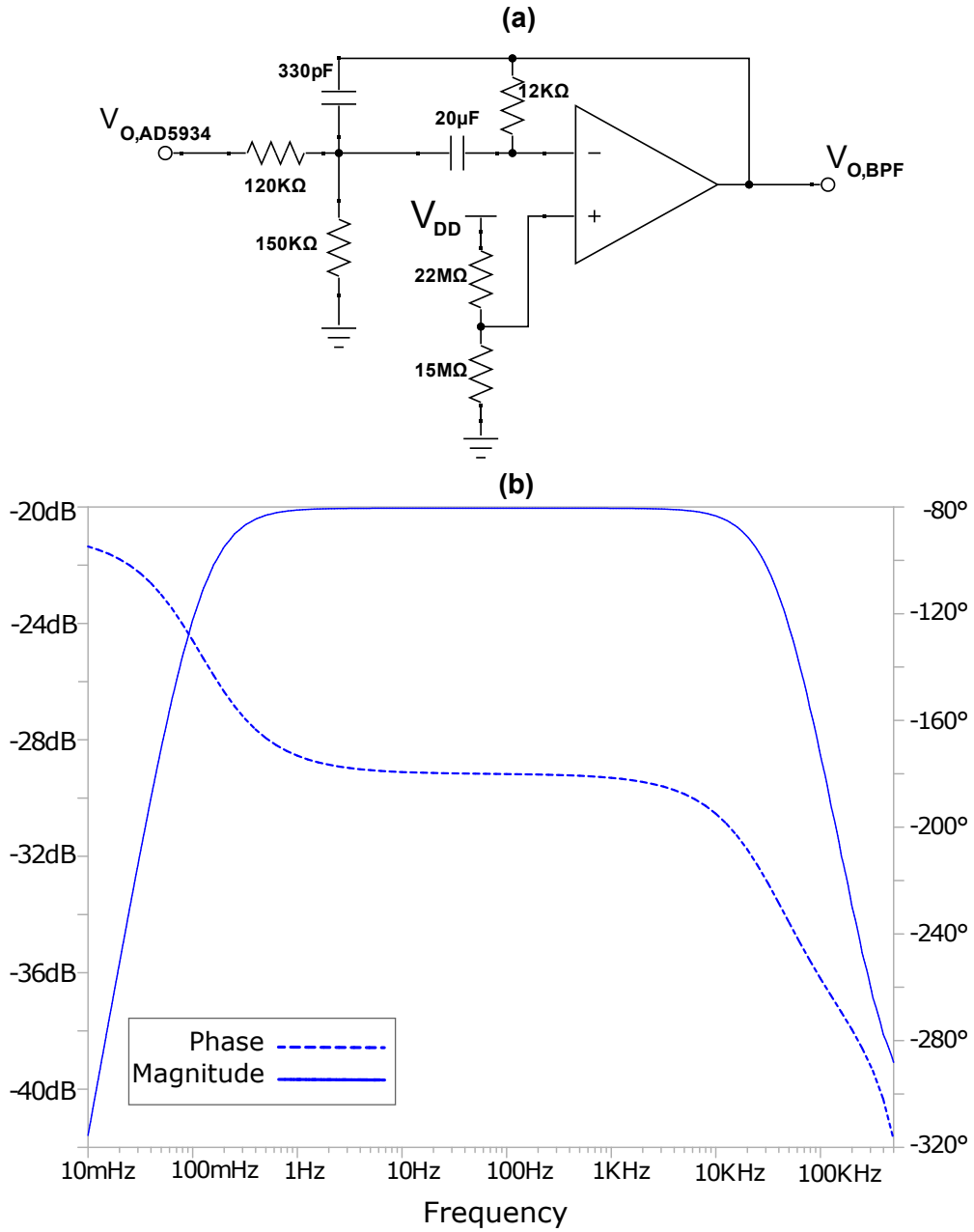

Figure 3.5: Band-pass filter (BPF) in the transmit stage. (a) Schematics (b) LTSpice simulation of the filter's frequency response.

3.3.2.3 Receive Stage

To measure the current flowing through the S/DUT, the second op-amp in the MCP6422 dual package is configured as a TIA (Figure 3.6). The non-inverting input, and consequently the inverting input of the op-amp, are set to 2.17 V by the microcontroller's digital-to-analog converter (DAC). During the EIS scan, this 2.17 V voltage is applied to the WE. With the 2-V offset in the applied excitation, this sets the voltage

across WE and RE to a 30 mV_{p-p} sinusoidal voltage with an offset of 170 mV. A single-pole four-throw (SP4T) analog switch can select the feedback impedance of the TIA. Four impedances (Z_1 , Z_2, Z_3, Z_4) are available for the TIA feedback. Z_1 is plugged into a socket on the circuit board and can be adjusted based on the S/DUT of interest. Z_2, Z_3, and Z_4 consist of 1 kΩ, 10 kΩ, and 100 kΩ in parallel with 10 nF, 1 nF, and 100 pF capacitors, respectively to set a low-pass cutoff of 15 kHz. The output voltage of the TIA is amplified by the AD5934's internal op-amp, and then sampled by the AD5934's ADC. With the external feedback network, this internal voltage amplifier (VA) has a gain of 3.70 and a bandwidth of 86.7 mHz to 10.6 kHz. After measurement at each frequency is complete, the AD5934 enters standby mode before starting the next measurement. During this period, the internal op-amp is disabled and the inverting input's voltage (marked as VDD/2 in Figure 3.6) drops to zero. Therefore, the steady-state DC voltage over the 68 μF capacitor changes by $V_{DD}/2$. When a new measurement starts, the capacitor must be charged to reach its steady-state first. One of the capacitors terminals is connected to the TIA output and is low-impedance. However, the resistance at the second terminal is 27 kΩ resulting in a time constant of 1.84 seconds. This significantly slows than the measurement process. In order to reduce the time constant, two 470 Ω resistors are connected to this capacitor terminal and a I/O pin of the microcontroller. During the settling period, the two pins are configured as outputs with one being low and one being high. This provides a path for the capacitor to be charged or discharged at a faster rate, changing the time constant to 16 ms. After settling, these two pins are configured as high-impedance inputs so they do not affect the TIA output.

3.3.2.4 Sensor Interface

The interface (Figure 3.7) consists of an op-amp, an SPDT analog switch, and an SP4T analog switch and can be configured in three modes: two-terminal impedance measurement, 3-electrode EIS, or calibration.

The 30 mV_{p-p} signal at the multiple-feedback filter output in the transmit stage is applied to the interface op-amp's non-inverting input.

In calibration and two-terminal impedance measurement modes, the interface op-amp is configured as a buffer. In the calibration mode, a calibration resistor is between the buffer output and the TIA input. In the two-terminal measurement mode, the buffer output and the TIA input are connected to the CE and RE connectors respectively. With the TIA input biased at 2.17 V and the buffer output being a 30 mV_{p-p} sinusoidal voltage with an offset of 2.0 V, the voltage applied to the S/DUT or calibration resistor is a 30 mV_{p-p} sine wave with an offset of 170 mV. The TIA measures the resulting current through the S/DUT or calibration resistor.

In the three-electrode EIS mode, the op-amp's inverting input is connected to the RE and the output is connected to the CE. The SUT creates negative feedback for the op-amp, setting the reference voltage

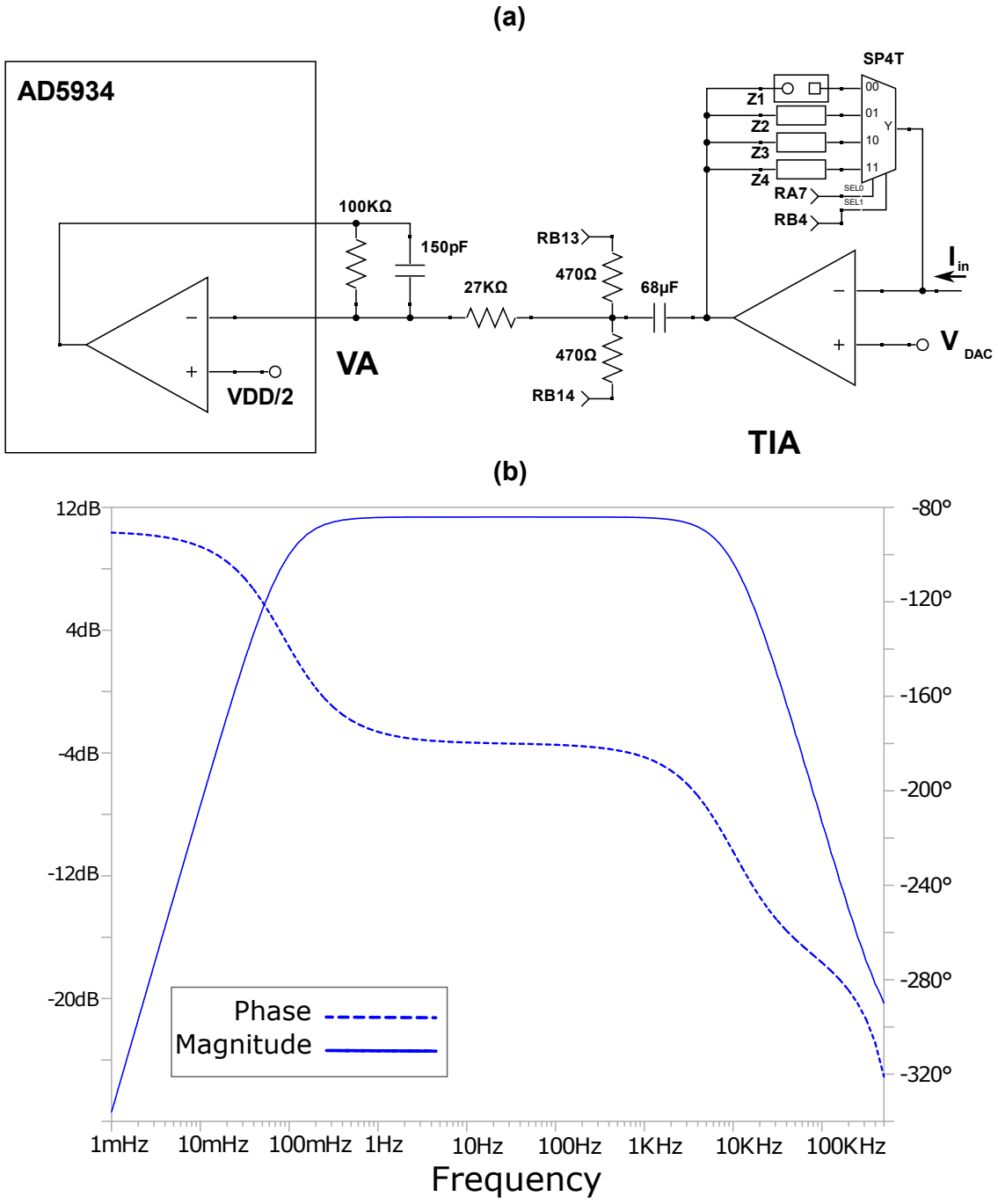

Figure 3.6: Receive stage consisting of a TIA and a internal voltage amplifier (VA). (a) Schematics (b) LTSpice simulation of the VA's frequency response when RB13 and RB14 are high-impedance.

to 30 mV_{p-p} and a DC level of 2.0 V. The WE is connected to the TIA's inverting input which is biased at 2.17 V. Therefore, the WE voltage with reference to the RE is a 30 mV_{p-p} sine wave with an offset of 170 mV. The resulting current flowing through the working electrode is measured by the TIA.

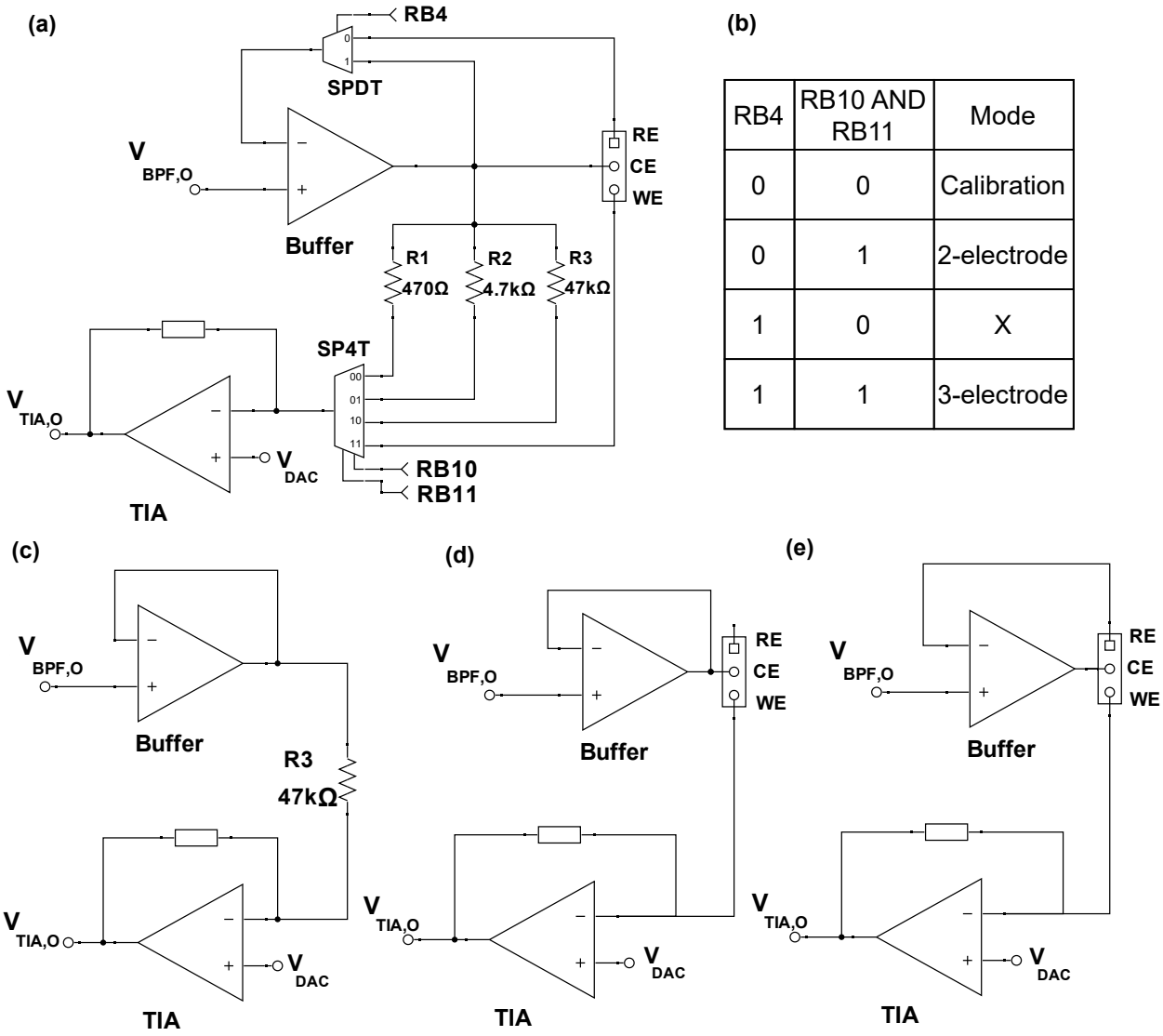

RB4	RB10 AND RB11	Mode
0	0	Calibration
0	1	2-electrode
1	0	X
1	1	3-electrode

Figure 3.7: Sensor interface. (a) Schematics (b) The interface's function in different states (c) The interface circuit in calibration mode with the 47 kΩresistor (RB4=1, RB10=1, RB11=0), (d) in 2-terminal mode (RB4=1, RB10=1, RB11=1), (e) in 3-terminal mode (RB4=0, RB10=1, RB11=1). In the 2-terminal mode, the DUT is placed between the CE and WE connections.

3.3.2.5 Error Detection and Adaptive Gain

If the amplitude of the voltage input to the AD5934's ADC is below a certain threshold, the impedance cannot be accurately measured. Moreover, if the gain is too large, the signal may be clipped. This results in invalid data. These thresholds are discussed in Section 3.3.2.8. In these cases, the TIA gain should be adjusted in order to bring the TIA output voltage to the desired range. Therefore, the voltage must be monitored and its amplitude should be determined.

The TIA output voltage is low-pass filtered and input to the microcontroller's ADC. After the AD5934

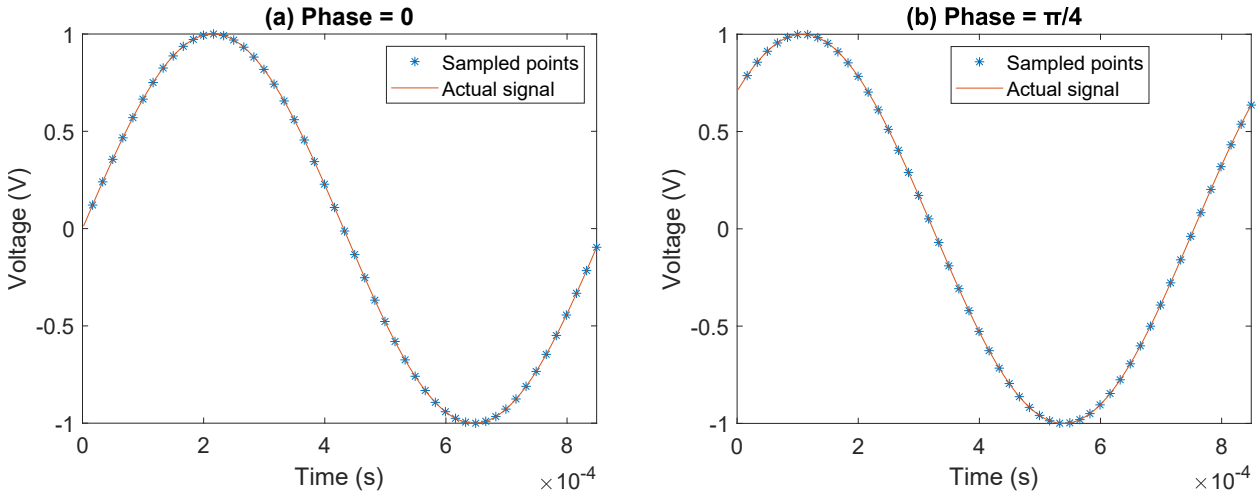

Figure 3.8: One period of a 1160 Hz sine wave sampled at 60 kSPS. While the sine wave's phase was swept from 0 to 2π in 1000 steps, only two examples with a phase of 0 and $\frac{\pi}{4}$ are shown here.

Exc. Frequency (Hz)	4880	1160	291	65.5	16.4	4.1	0.91
No. of samples	12.3	51.8	206	917	3663	14689	66094

Table 3.2: Number of samples that the microcontroller ADC can capture in one period of the excitation frequency.

buffer is full, the excitation continues for a period of time leading to a valid TIA output. During this time, the ADC continuously samples this voltage for a minimum duration of one period of the excitation signal. The sampling rate is approximately 60 kSPS. This means that the number of samples per period of the excitation frequency is between 12 and 66000 (Table 3.2). To determine the amplitude of the signal, the lowest voltage measured by the ADC is subtracted from the highest one. To get a good estimate of the amplitude, we must ensure that the signal's peaks are being captured by the ADC.

For 1160 Hz and below, during one period of the excitation signal at least 51 samples are taken. To ensure that this number is enough to capture the amplitude, MATLAB simulations were done. Figure 3.8 shows one period of a sine wave sampled at 51 points. with 1000 different phase values between 0 and 2π, the amplitude of this wave was calculated by detecting the peaks. A maximum error of 0.23% was observed. Therefore, 51 samples is sufficient for measuring the amplitude. A higher number of samples increases the accuracy.

For 4880 Hz however, only 12 points per period are sampled (Figure 3.9). According to simulations, this can cause an error of 9.0%. Therefore, 200 samples (approximately 16 periods) were taken instead (Figure 3.10). Similar to before, MATLAB simulations were done with this number of samples and a maximum error of 0.007% was observed in the amplitude. Therefore, 200 samples are sufficient.

By default, the first feedback branch (plug-in impedance, Z_1) is used. If at any point the measured

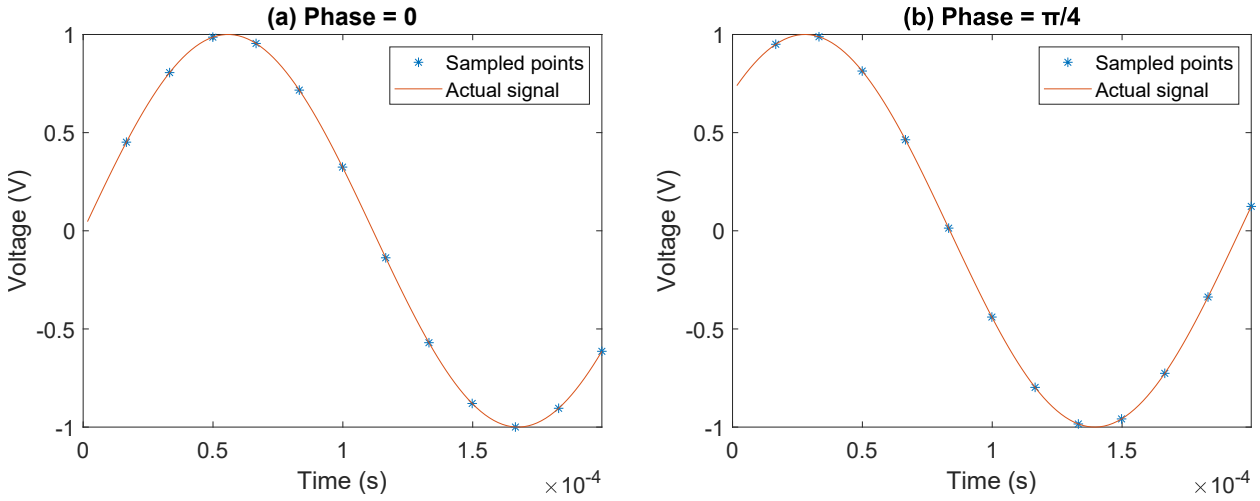

Figure 3.9: One period of a 4880 Hz sine wave sampled at 60 kSPS.

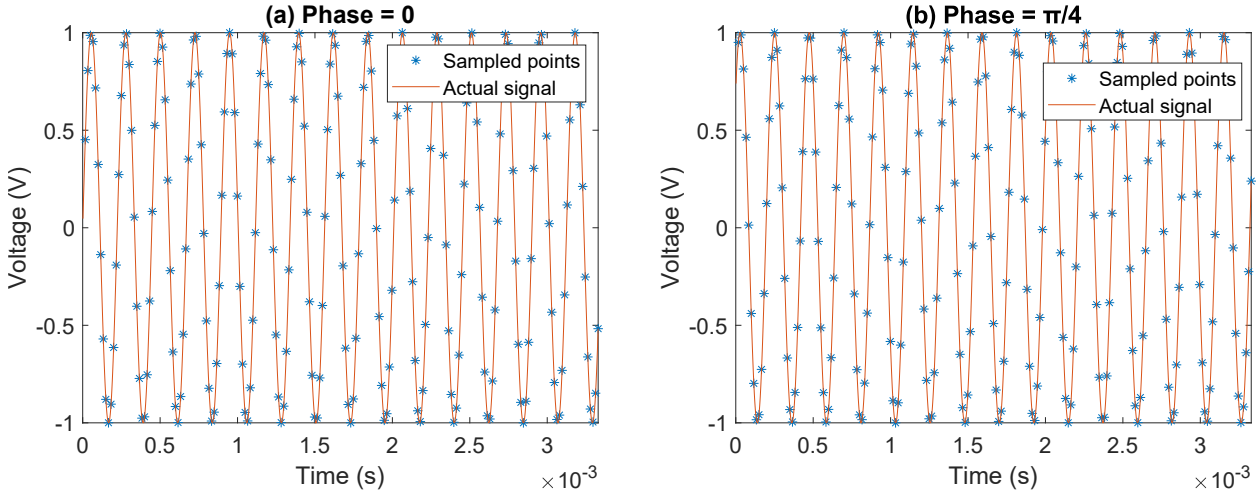

Figure 3.10: Approximately 16 periods of a 4880 Hz sine wave sampled at 60 kSPS.

voltage is above a certain threshold, indicating saturation, a high gain error is detected. If the peak-to-peak voltage measured by the ADC is below or above the desired range, a low gain or a high gain error is detected, respectively. In case of a gain error, the measurement at the current frequency is restarted using a different feedback branch. The feedback branch is chosen based on the previous feedback branch and the error type. In the case of a high gain error, the gain is decreased and vice versa. Figure 3.11 illustrates how the feedback branch is selected. In case valid data cannot be obtained and the impedance is outside the device's range, this information is stored the microcontroller's EEPROM. 7 bits in the memory are used, each corresponding to a frequency. At the start of each scan, zero is written to the register. If measurement at a frequency ends in a gain error, the corresponding bit is set. Additionally, the branch number used for each measurement is stored in the memory.

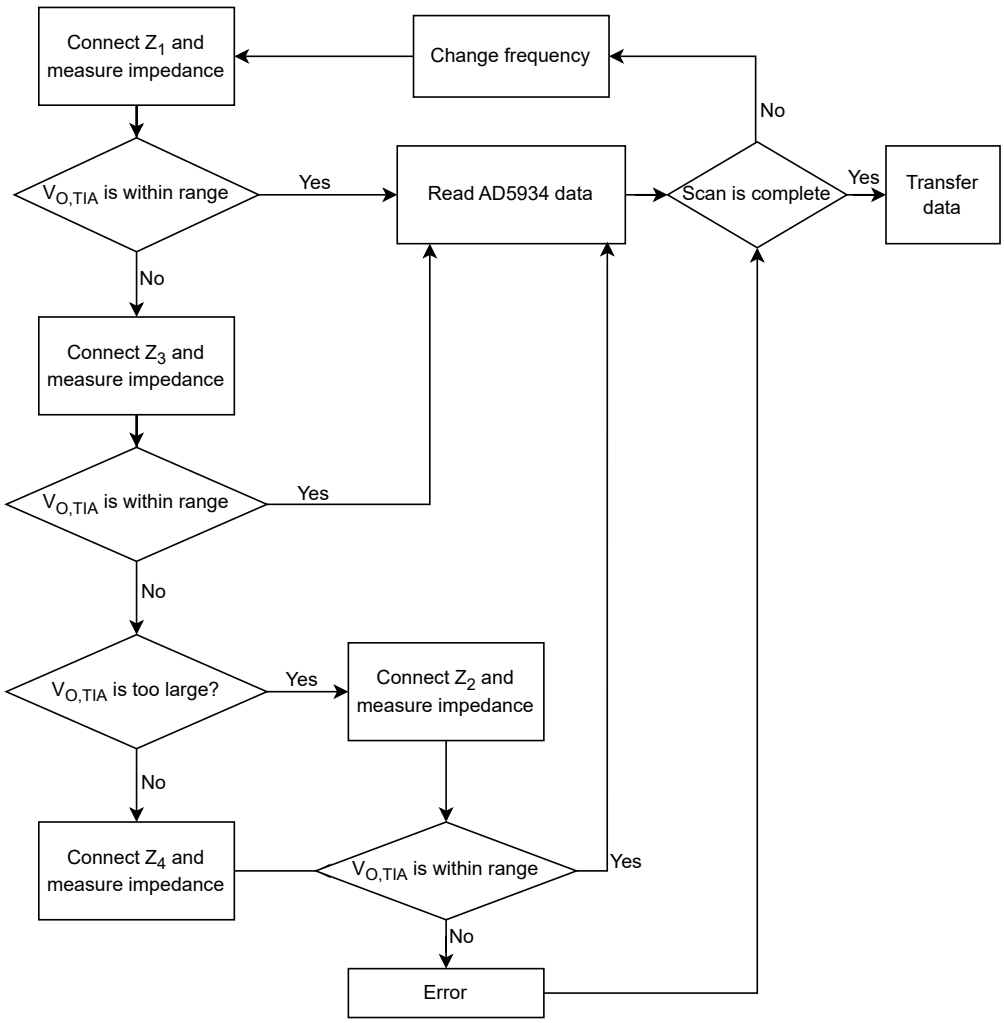

Figure 3.11: Gain selection process.

3.3.2.6 Wireless Communication

Wireless communication between the circuit and the user's personal device relies on the RN4871 BLE module. When measurement for all seven frequencies is completed, the module powers on and starts advertising, awaiting a paired device to establish a connection. A status pin from the BLE module is monitored by the PIC microcontroller to detect a successful connection. Since the digital high levels for the BLE module and the microcontroller are 3 V and 5 V, respectively, a MOSFET is used as a level-translator for this pin. Once linked, the microcontroller employs a UART to transmit impedance data to the BLE module. The TX signal from the microcontroller is stepped down by a resistor divider (Figure 3.12). This module functions as a transparent UART pipe, forwarding data to the connected device. The data consists of 32 bytes: 28 bytes for seven measurements at different frequencies, 3 bytes indicating the TIA gain and error information, and 1 byte indicating the transfer completion to the user. Upon data transfer completion, the PIC microcontroller

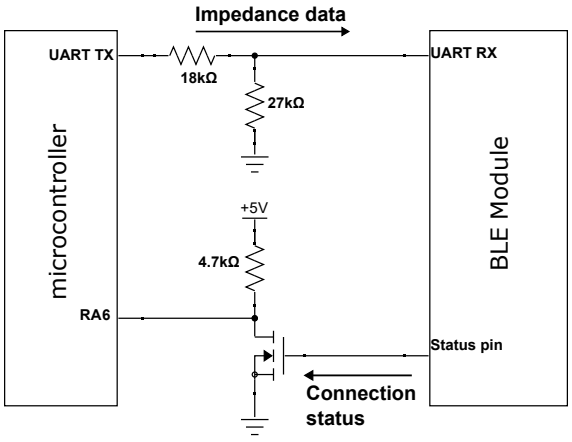

Figure 3.12: The BLE-microcontroller interface.

promptly powers down the BLE module and enters sleep mode to reserve power.

3.3.2.7 Power Management

The board is powered by two 3-Volt 2025 Lithium coin cells in series. When the power switch is on, two regulators are powered up by the batteries. A 5-Volt linear regulator supplies power to all components except the BLE module, which employs a separate 3-Volt linear regulator with an enable pin. The PIC microcontroller enables the 3-volt regulator only when transmitting data over BLE.

3.3.2.8 Dynamic Range

There are three factors limiting the dynamic range: clipping at the TIA output, clipping at the AD5934 internal amplifier, and the ADC resolution.

The TIA op-amp's (LMV551) positive output swing is limited [93]. This makes the maximum possible voltage at the TIA output 4.845 V ($V_{\max}$). In equation 3.6, $V_{\mathrm{TIA},O}$ and V_{DAC} are the TIA output voltage and the TIA's DC bias voltage as shown in Figure 3.7. $\max(V_{\mathrm{TIA},o})$ is the maximum permissible TIA output voltage that can be detected by the microcontroller. V_{bias} and v_{exc} refers to the DC voltage and the excitation peak-to-peak voltage amplitude applied to the S/DUT through the transmit stage amplifier. A_{DC} and A_{AC} are the DC and AC voltage gain from the CE connection node to the TIA output (Figure 3.7).

$$V_{\max} > \max(V_{\mathrm{TIA},O}) = A_{\mathrm{DC}} \cdot V_{\mathrm{bias}} + V_{\mathrm{DAC}} + A_{\mathrm{AC}} \cdot \frac{v_{\mathrm{exc}}}{2} \tag{3.6}$$

The internal amplifier has a nominal gain of 3.70, and a nominal bias point of 2.5 V. However, an output bias point as high as 2.8 V was measured. A maximum peak-to-peak amplitude of 1.1 V was selected for

the TIA output, setting the valid peak-to-peak output swing of the internal amplifier to approximately 4 V and allowing for a ±500 mV error on the bias point.

$$A_{\mathrm{AC}} \cdot v_{\mathrm{exc}} < 1.1 \tag{3.7}$$

From Section 1.2.4.2, according to MATLAB simulations, a peak-to-peak amplitude of 7.2 mV should be sufficient to obtain admittance magnitude errors of less than 5%. However, in experiments, for peak-to-peak amplitudes below 45 mV, the impedance converter generated invalid data. That is, the measured admittance was close to zero, and the calculated impedance was infinite or significantly larger than the actual impedance. This is in agreement with the findings of Chabowski et al. who reported that with a supply voltage of 3.3 V, a minimum voltage amplitude of 30 mV_{pp} was required [16]. Therefore, a higher limit was selected based on experimental results. Based on noise measurements in Section 3.4.1, the threshold was adjusted, and the minimum amplitude was set to 60 mV_{pp}. Therefore, the minimum valid amplitude at the TIA output was set to 60/3.7 =16.2 mV_{pp}.

$$A_{\mathrm{AC}} \cdot v_{\mathrm{exc}} > 0.0162 \tag{3.8}$$

While the circuit was designed for a V_{bias} of 170 mV, the actual V_{bias} was measured to be 176 mV. Substituting V_{bias} = 176 mV, v_{exc} = 30 mV, V_{DAC} = 2.17 V, and the thresholds in equations 3.6, 3.7 and 3.8:

$$4.845 - 2.17 = 2.675 > A_{DC} \cdot 0.176 + A_{AC} \cdot 0.015 \tag{3.9}$$

$$A_{AC} > 0.540 \tag{3.10}$$

$$A_{AC} < 36.7 \tag{3.11}$$

The impedance under test can be represented as $Z = R + jX$. If the TIA feedback consists of resistor (R_f) in parallel capacitor (C_f), with a pole larger than the excitation frequency, the AC and DC gain are:

$$A_{AC} = \frac{R_f}{|Z|} \tag{3.12}$$

$$A_{DC} = \frac{R_f}{R} \tag{3.13}$$

The three on-board feedback options (Z_2, Z_3, Z_4) meet this criteria. Therefore, for these feedback

impedances, the range of impedances that can be measured is defined by:

$$\frac{R_f}{36.7} < |Z| < \frac{R_f}{0.540} \tag{3.14}$$

$$2.675 > \frac{R_f}{|Z|} \cdot 0.015 + \frac{R_f}{R} \cdot 0.176 \tag{3.15}$$

Since $|Z| = \sqrt{R^2 + X^2}$,

$$\frac{R_f}{R} \cdot 0.015 + \frac{R_f}{R} \cdot 0.176 > \frac{R_f}{|Z|} \cdot 0.015 + \frac{R_f}{R} \cdot 0.176 \tag{3.16}$$

Therefore, for equation 3.15 to be satisfied, it is sufficient that:

$$2.675 > \frac{R_f}{R} \cdot 0.015 + \frac{R_f}{R} \cdot 0.176 \tag{3.17}$$

Or equivalently,

$$R > 0.071 R_f \tag{3.18}$$

This condition ensures that the left-hand equality in equation 3.14 is satisfied. Therefore, the dynamic range can be represented as:

$$R > 0.071 R_f \quad \text{and} \quad |Z| < \frac{R_f}{0.540} = 1.85 \cdot R_f \tag{3.19}$$

Note that for a purely resistive load, equations 3.15 and 3.17 are equivalent. For a highly capacitive load however, the first term in the right-hand side of inequality 3.15 is significantly smaller than the second term and can be ignored. This marginally changes the boundary for R (from $0.071 \cdot R_f$ to $0.067 \cdot R_f$). This means that the range in equation 3.19, which was found based on the boundary calculated from equation 3.17 is fairly accurate, and only leaves out an insignificant range of measurable impedances. The range defined by equation 3.19 is shown in Figure 3.13.

With three on-board feedback branches, the dynamic range of the system consists of sections of three circles with radii of 1.85 kΩ, 18.5 kΩ, and 185 kΩ on the Nyquist plot. The plugged-in TIA feedback can extend this range.

In this work, the plugged-in impedance was selected to cover all the cortisol samples of interest. The range of interest could not be covered by a TIA feedback with a fixed impedance magnitude in the 0.8 Hz to 4.88 kHz range. The range of impedance is different at each frequency, which would require a different R_f. Therefore, an impedance with varying magnitude in this frequency range was selected. Based on the

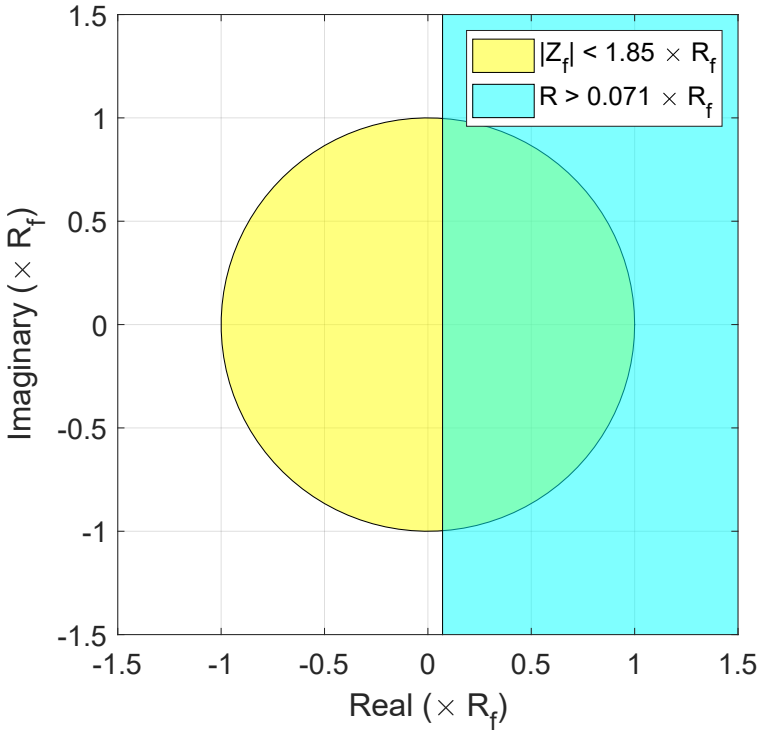

Figure 3.13: Nyquist plot showing the dynamic range of the EIS device, when using R_f as the feedback of the TIA. The intersection of the two areas is the dynamic range, shown in green.

range of sample impedances at each frequency, an R(RC) cell (similar to Figure 3.20) consisting of a 47 kΩ resistor in parallel with a 4.7 nF capacitor, in series with a 10 kΩ was used. This impedance has a pole at 721 Hz. Therefore, the AC gain cannot be expressed with no frequency dependence as it was in equation 3.12. Instead, the radius associated with the dynamic range changes with frequency to match the requirements of the samples.

3.3.3 Data Processing

Each measurement cycle generates 7 pairs of numbers corresponding to the real and imaginary admittance values across 7 frequencies (G_i and B_i, $i = \{0, 1, ..., 6\}$). Additionally, three 7-bit blocks of data consisting of a gain error indicator (E) and two feedback branch designations (F_{LO} and F_{HI}) for the TIA are included. Each bit of these arrays corresponds to its respective frequency.

During calibration, admittances are recorded across the 7 frequencies for different combinations for calibration resistors and feedback branches. For the three fixed TIA feedback branches, a calibration resistor is preselected. For the plug-in feedback however, since the gain is variable and unknown to the circuit, an appropriate calibration resistor must be selected. Therefore, three scans using each of the three calibration resistors are performed. With three scans for the fixed feedback branches and three for the plug-in one, in

total, six scans are completed during calibration, providing 42 real and imaginary pairs of numbers ($G_{cj,i}$ and $B_{cj,i}$, $j = \{0, 1, ..., 6\}$, $i = \{0, 1, ..., 5\}$). Each of the six combinations also include three blocks of data for feedback branch designations and gain error indication.

When processing data from measurements in measurement mode, for each frequency, the system identifies the relevant feedback branch using the respective F_{HI} (MSB) and F_{LO} (LSB) bits. The calibration data corresponding to the identified branch is then selected. For fixed feedback branches, the calibration resistor value is predetermined. For the adjustable branch, at each frequency, three calibration data pairs corresponding to each calibration resistor are available, some of which may be invalid. Validity can be confirmed using the gain error indicator (E) bits. Based on the gain error indicator, a valid pair is selected. Through this process, a 2×7 array of calibration data is constructed (G_{ci} and B_{ci}, $0 < i < 7$).

If measurement at a particular frequency results in a gain error, the corresponding data is discarded. Magnitude and phase of the valid calibration and measurement data are calculated. Calibration magnitudes and phases are used to find the gain factor and phase offset. These parameters are used to calculate impedance based on the measurement data.

In EIS for measuring cortisol concentration, Reaction Charge Transfer Resistance (R_{ct}), must be extracted from the impedance's Nyquist plot. To determine R_{ct}, first the Warburg tail must be detected and excluded. This is done by detecting changes in the slope in the Nyquist plot. The data point at which the plot's slope changes from negative to positive, is detected as the beginning of the Warburg tail. This data point and the ones following it (lower frequencies), are excluded from the data. The remaining data is then fitted with a circle. This circle's diameter is the R_{ct}.

3.4 Characterization

The device was assessed in terms of signal quality and its performance when measuring the impedance of resistor and capacitor combinations. The results are included in the following sections.

3.4.1 Noise

With no S/DUT connected, the excitation signal at seven frequencies was sampled at 82500 SPS by a DAQ device for a duration of 10 periods of each signal. The DFT was calculated with a spectral resolution of 0.1 times the signal's frequency and highest frequency of 41250 Hz. A representative Fourier transform magnitude with the excitation at 291 Hz is shown in Figure 3.14 with the fundamental and harmonics annotated. Across all frequencies, peak-to peak excitation amplitudes ranging between 28 mV and 30 mV were observed. The SNR, excluding six harmonics of the excitation frequency, and THD including six

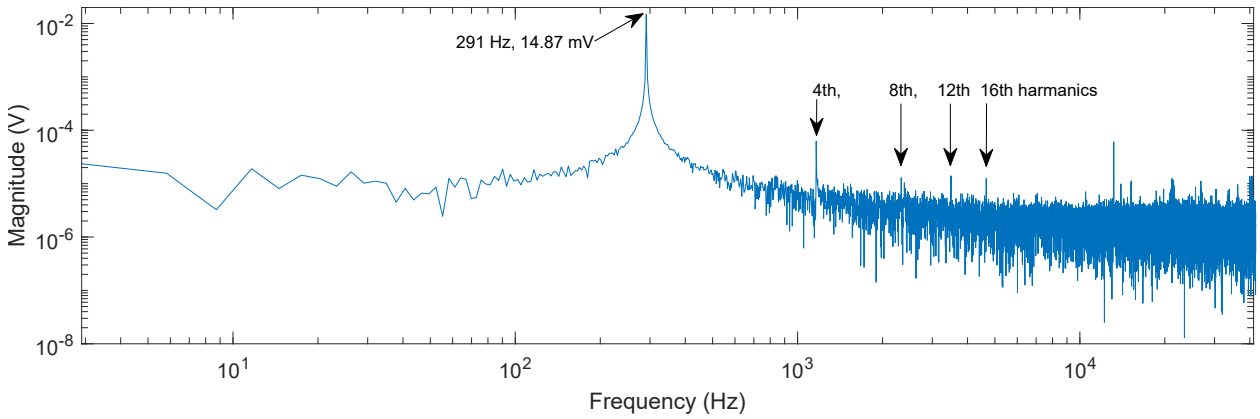

Figure 3.14: The 291 Hz excitation signal amplitude in frequency domain. The fundamental frequency and its significant harmonics are marked on the plot.

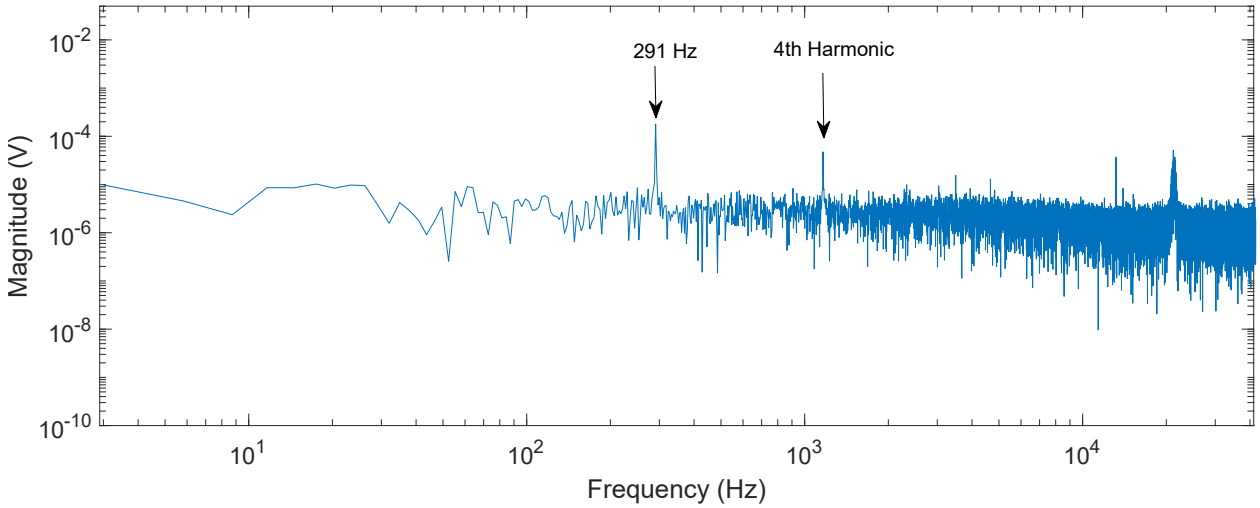

Figure 3.15: The TIA output in frequency domain with no S/DUT, with the first TIA feedback branch connected, with an excitation frequency of 291 Hz.

Table 3.3: Amplitude, noise, and distortion in the excitation signal. These values were averaged over four measurements.

Frequency (Hz)	4880	1160	291	65.5	16.4	4.09	0.91
Exc. Voltage (mV_{pp})	29.75	29.90	29.61	29.68	29.68	29.78	29.39
SNR	3761	3736	3041	1433	715	2051	2457
THD ($\times 10^{-5}$)	5.66	1.41	2.72	2.79	2.97	2.90	3.58

harmonics were calculated. The results are included in Table 3.3.

With no S/DUT connected, the TIA and the internal amplifier's output were similarly measured once with each TIA feedback impedance connected. Representative Fourier transform magnitudes with the excitation at 291 Hz and the first feedback impedance are shown in Figures 3.15 (TIA output) and 3.16 (internal amplifier output). RMS noise was calculated at both nodes. These values are included in tables 3.4 and 3.5.

In the worst case, the TIA output noise was 4.6 mV_{RMS}. This affects the voltage monitored for gain

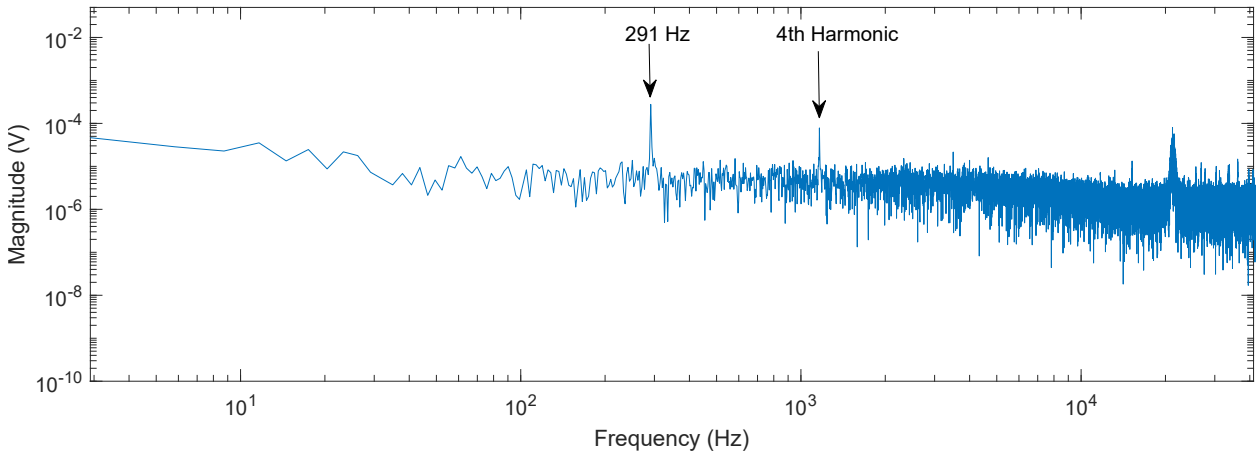

Figure 3.16: The internal amplifier's output in frequency domain with no S/DUT, with the first TIA feedback branch connected with an excitation frequency of 291 Hz.

Table 3.4: Noise at the TIA output in mV_{rms} measured at different excitation frequencies and feedback gains.

	Noise (mV_{rms})						
TIA Feedback \f (Hz)	**4880**	**1160**	**291**	**65.5**	**16.4**	**4.09**	**0.91**
$(47\ k\Omega \parallel 4.7\ nF) + 10\ k\Omega$	0.484	0.693	0.452	3.417	4.088	4.017	2.858
1 kΩ	0.279	1.659	0.996	2.335	4.602	4.037	2.894
10 kΩ	0.415	1.439	0.429	2.557	3.903	3.960	2.589
100 kΩ	0.764	0.431	0.906	2.359	4.230	4.317	2.982

Table 3.5: Noise at the internal amplifier's output in mV_{rms} measured at different excitation frequencies and feedback gains.

	Noise (mV_{rms})						
TIA Feedback \f (Hz)	**4880**	**1160**	**291**	**65.5**	**16.4**	**4.09**	**0.909**
$(47\ k\Omega \parallel 4.7\ nF) + 10\ k\Omega$	0.374	0.387	0.540	4.281	4.318	3.098	2.010
1 kΩ	0.202	0.217	0.296	1.226	1.435	0.745	0.422
10 kΩ	0.200	0.214	0.299	1.291	1.469	0.766	0.434
100 kΩ	0.239	0.226	0.297	1.786	2.380	1.194	0.623

switching. To account for this noise, the lower and upper amplitude threshold for gain switching was increased and decreased by approximately 6 mV ($\sqrt{2 \times 4.6^2} = 6.5$), respectively. The threshold for detecting saturation was also decreased by approximately 4 mV_{RMS}.

As shown in Table 3.5, noise at the AD5934 ADC input can be as high as 4.3 mV_{RMS}. This can cause significant error since the 12-bit ADC's resolution is approximately 1.2 mV. Since the device's dynamic range covers well beyond the impedance of the target samples, the error thresholds were simply modified to limit the dynamic range so that a 4.3 mV noise would not cause a significant error. As mentioned in Section 3.3.2.8, a minimum voltage amplitude of 30 mV (60 mV peak-to-peak) was selected.

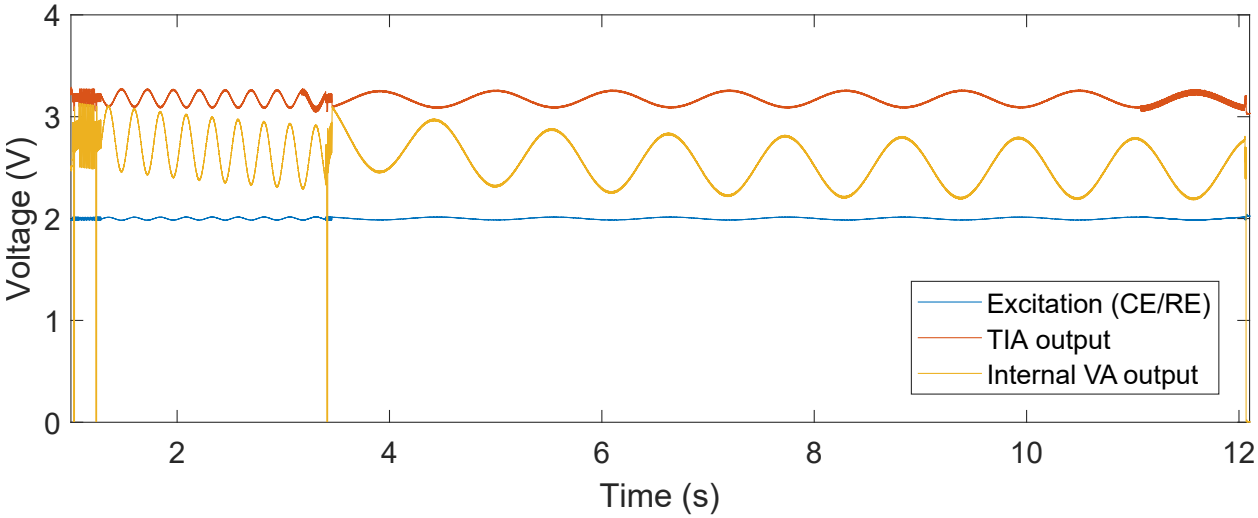

Figure 3.17: Critical signals during measurement of a resistor.

3.4.2 Impedance Measurement Characterization

The impedance of various resistors and RC cells were measured by the device in two-terminal mode. The results of these tests are included in this section.

3.4.2.1 Resistors

Figure 3.17 shows three critical signals during a typical resistance measurement for a 10 kΩ resistor. In this measurement, the circuit was configured for 2-terminal measurement and a resistor was placed between the WE and CE connector (Figure 3.7 (d)). As illustrated in the plot, the excitation signal has an amplitude of 15 mV and offset of 2 V. The scan starts from 4880 Hz and ends with 0.91 Hz. The TIA output is an amplified version of this signal. The breaks in the AD5934's internal voltage amplifier's output are between measurements at two frequencies when the internal op-amp is disabled.

To test the dynamic range, accuracy, and precision of the device, eleven resistors with nominal values from 68 Ω to 470 kΩ were measured. Each scan was repeated ten times. The device was able to calculate an impedance for the 100 Ω to 180 kΩ resistors while testing the selected resistors outside this range resulted in a gain error. For the 180 kΩ resistor, an impedance could be measured only at the four lowest frequencies, with errors at the higher ones. Note that 180 kΩ is close to the upper limit of the dynamic range, and a slight decrease in the nominal system gain due to parasitics can cause a gain error. Measurements with gain errors were discarded in the following statistics.

Figure 3.18 shows the results of one scan on each of the resistors. Disregarding parasitic effects, the resistance measured at different frequencies should be the same. For each scan, we calculated the coefficient

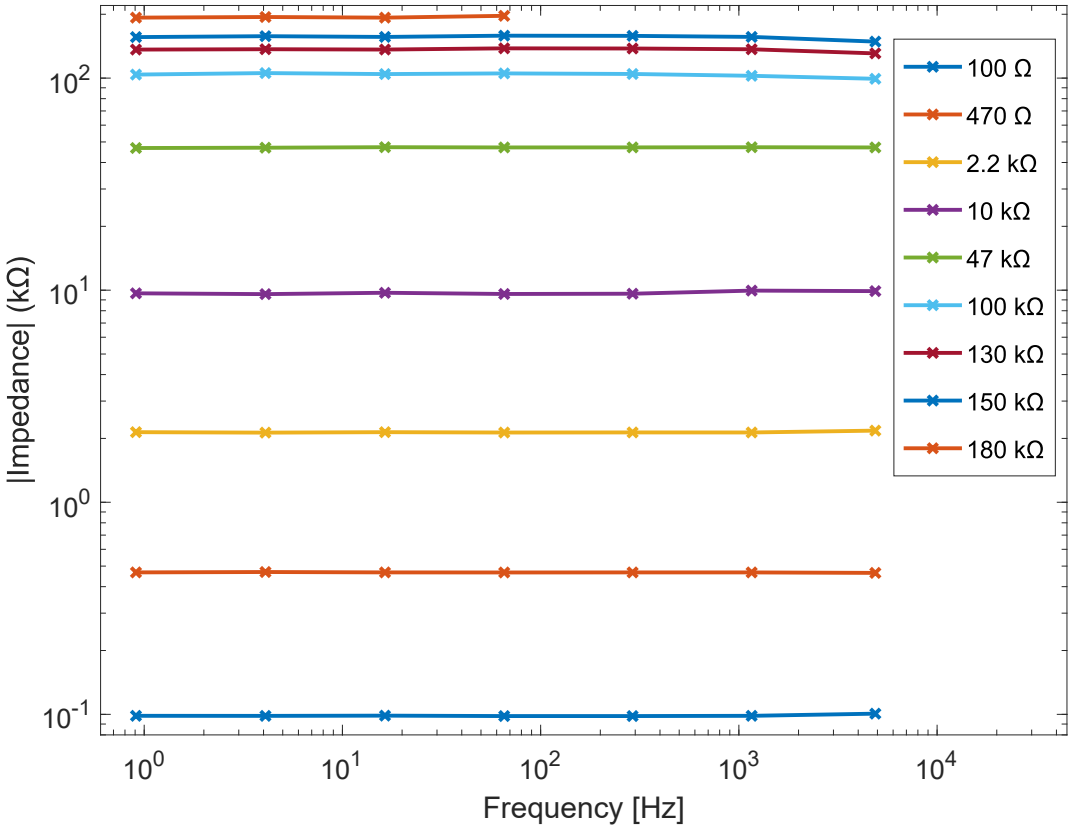

Figure 3.18: Nine resistors measured by the EIS device in two-terminal mode.

of variation of the resistances measured at the ten frequencies. The frequency-dependent variation ranged between 0.16% and 2.38%. This variation was larger when different TIA feedbacks were used at different frequencies. For instance, the 100 kΩ resistor is near the upper limit of the dynamic range covered by TIA feedback branch one ($Z_1 = (47\ k\Omega \parallel 4.7\ nF) + 10\ k\Omega$) at 291 Hz. At this frequency, the magnitude of the impedance is approximately 57 kΩ. Therefore, theoretically it can be used to measure resistors up to $1.85 \times 57\ k\Omega = 105\ k\Omega$. Due to noise triggering the adaptive gain control, in some cases, impedance at 291 Hz was measured by TIA feedback branch one, and in others by feedback branch four (Z_4 =100 kΩ). Because the magnitude of Z_1 decreases as frequency increases, at lower and higher frequencies TIA feedbacks one and four were used, respectively. Since different feedback branches were used for measurements at different frequencies, the frequency-dependent variation was higher (1.42%), comparing to 0.21% and 0.34% for the adjacent resistor (47 kΩ and 130 kΩ) values. For the 47 kΩ and 130 kΩ resistors, the device used TIA feedback branches one and four at all frequencies, respectively.

To evaluate repeatability, for all nine resistors within the dynamic range, the coefficient of variation over the ten measurements was calculated at each frequency, yielding up to seven values for each of the nine resistors. The maximum and minimum variation among the values associated with each resistor are included

Table 3.6: Accuracy and variation in resistance measurements by the custom EIS device. Measured (R) resistance is the average impedance magnitude calculated at seven frequencies and ten repetitions. Lowest and highest CoV (coefficient of variation) indicate the variation across ten measurements (averaged over seven frequencies) by the custom device.

Nominal R (kΩ)	**0.1**	**0.47**	**2.2**	**10**	**47**	**100**	**130**	**150**	**180**
Measured R (EIS device)	0.10	0.47	2.14	9.66	47.00	104.65	136.49	156.68	193.23
Measured R (DMM)	0.10	0.47	2.16	9.93	46.94	99.42	131.12	149.04	181.27
Error (%)	-0.24	0.36	-1.05	-2.71	0.12	5.27	4.09	5.13	6.60
Lowest CoV (%)	0.04	0.03	0.04	0.03	0.00	0.02	0.18	0.18	0.17
Highest CoV (%)	0.05	0.01	0.11	0.40	0.41	1.43	0.63	0.95	1.32

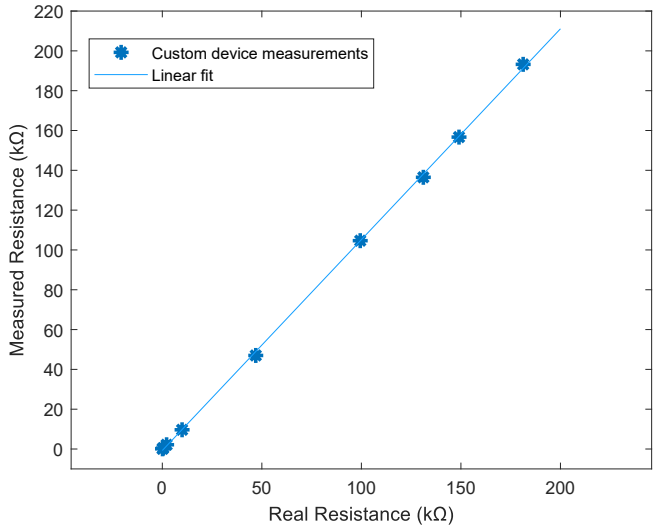

Figure 3.19: Measured resistances plotted against the actual resistor values. DMM measurements were used as a reference.

in Table 3.6. The magnitude of the impedance of the cortisol samples of interest fall within the 0.47 kΩ to 47 kΩ range where the results are highly repeatable.

Considering the marginal variation, to evaluate accuracy, the measured impedances were averaged over the seven frequencies and ten repetitions. These averaged values were compared against resistances measured by a digital multimeter (DMM). As shown in Table 3.6, the absolute errors are within 7%. In the 0.47 kΩ to 47 kΩ range, the error is less than 3%. Therefore, in the 100 Ω to 180 kΩ, with the exception of gain errors at higher frequencies for 180 kΩ, the device works as expected. This matches the calculated dynamic range for the system described in Section 3.3.2.8.

The measured resistances were plotted against the DMM measurements to showcase linearity (Figure 3.19). A linear regression model was fitted to the data, resulting a slope of 1.06 and a root mean square error of 1.32 and R-squared of 0.9997.

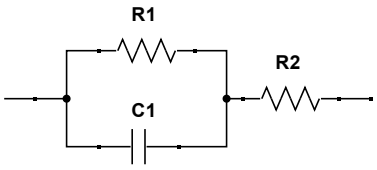

	R1 (kΩ)	C1 (nF)	R2 (kΩ)
Z1	1	1000	1
Z2	10	100	1
Z3	10.1	100	1
Z4	68	22	1.8

Figure 3.20: Four tested RC cells, with values within the device's dynamic range. The table includes the nominal component values.

Table 3.7: The custom device's measured phase and magnitude variations in R(RC) cells.

R(RC) Cell #	1	2	3	4
Lowest STD (degree) in phase	0.02	0.04	0.05	0.09
Highest STD (degree) in phase	0.22	0.41	0.25	0.74
Lowest CoV (%) in magnitude	0.06	0.09	0.06	0.20
Highest CoV (%) in magnitude	0.50	0.37	0.77	1.00

3.4.2.2 R(RC) Cells

The impedance of four R(RC) cells (Figure 3.20) was measured by the custom device and a commercial potentiostat from Metrohm (Switzerland). These cells were designed to mimic the behavior of electrochemical samples. In these cells, R1 corresponds to R_{ct} in an electrochemical sample. We set up two cells with R_1 values close to the impedance range found in cortisol samples of our interest; one with R_1 of 10 kΩ and the other with 10.1 kΩ. Additionally, we included a cell with a smaller R_1 value of 1 kΩ. To further test the device's dynamic range, we included a cell with a significantly larger R_1 value of 68 kΩ. This setup allowed us to showcase the device's ability in distinguishing between cells with close values of R_1, or equivalently samples with close R_{ct}s, as well as covering a wide range of samples. Similar to the resistor tests, the impedance of each was measured 10 times. Variation in the measured impedance magnitude and phase, obtained by the custom device and the Metrohm potentiostat are shown in Tables 3.7 and 3.8, respectively. Each number represents the variation over 10 measurements of a certain RC cell. The lowest and highest variations correspond to variation in measurements at a certain frequency. As shown in Table 3.7, our device's measurements are highly repeatable. The variation in the Metrohm potentiostat's measurements were lower however (Table 3.8).

The measured magnitudes and phases were averaged over ten measurements and compared to the same measurements by the Metrohm potentiostat. The magnitude, phase, and R_1 corresponding to both devices are illustrated in Figures 3.21 to 3.23. Table 3.9 shows the magnitude and phase comparison at all frequencies,

Table 3.8: The Metrohm device's measured phase and magnitude variations in R(RC) cells.

R(RC) Cell #	1	2	3	4
Lowest STD (degree) in phase	0.00	0.01	0.01	0.02
Highest STD (degree) in phase	0.05	0.14	0.14	0.56
Lowest CoV (%) in magnitude	0.01	0.02	0.04	0.03
Highest CoV (%) in magnitude	0.16	0.34	0.42	0.63

and Table 3.10 compares the calculated R_1 values. In error calculations, Metrohm potentiostat measurements were used as the reference to evaluate the custom device's accuracy.

The error in magnitude ranged from 0.49% to 10.58%, and the error in phase was between 0.11 and 5.81 degrees. After fitting a circle to the impedance data represented in a Nyquist plot, R1 was extracted. The worst-case variation in the calculated R1 in 10 measurements of four R(RC) cells, performed by the custom device was 0.28% comparing to 0.26% for the potentiostat. For cell 2 and 3 which are similar to cortisol samples, this variation was higher in the custom circuit measurements (0.11% comparing to 0.06% in the potentiostat). The error in R1 was between -3.03% and 2.28%. The results indicate that R1 is underestimated for smaller impedance magnitudes and overestimated in higher ones. This is consistent with resistor measurements included in Table 3.6.

Cohen's distance (d) can be used as a measure of the device's ability to distinguish between two values of R_1. In equation 3.20, d and σ are the Cohen's distance and the pooled standard deviation. μ_i, σ_i, and n_i are mean, standard deviation, and sample size of the i^{th} group. Equation 3.21 shows the Cohen's distance when sample sizes are equal. The numerator represents the difference between the means of the two groups and the denominator represents an average uncertainty. Thus, the ratio is a measure of how well the groups can be separated, with larger numbers being better.

$$d = \frac{\mu_1 - \mu_2}{\sigma}, \quad \sigma = \sqrt{\frac{(n_1 - 1)\sigma_1^2 + (n_2 - 1)\sigma_2^2}{n_1 + n_2 - 2}} \tag{3.20}$$

$$n_1 = n_2 \Longrightarrow \quad d = \frac{\mu_1 - \mu_2}{\sqrt{\frac{1}{2} \cdot (\sigma_1^2 + \sigma_2^2)}} \tag{3.21}$$

The average R_1 calculated for cell 3 was 140 Ω larger than cell 2. The standard deviation in the 10 trials were 10.6 Ω and 12.0 Ω respectively, indicating a Cohen's distance of 12.60. Therefore, R_1 in cell 2 and cell 3 can be easily distinguished by our device.

3.4.3 Power Consumption

Power consumption in a complete scan and data transmission cycle depends on the D/SUT and how the user interacts with the device. For instance, if gain switching is required, the measurement may take up

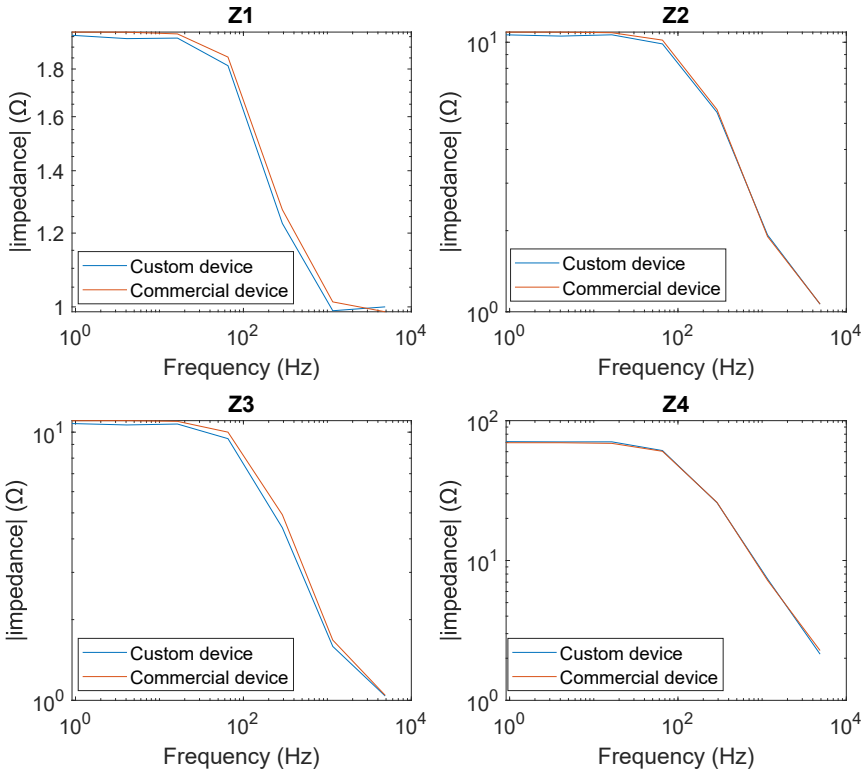

Figure 3.21: Average measured impedance magnitudes in four R(RC) cells, acquired by the custom and Metrohm devices.

to 60 s, compared to 15 s for a different D/SUT that does not require gain switching. Since the user is responsible for initiating a BLE connection with the device and disconnecting afterwards, the BLE module's energy consumption is highly affected by the user.

When powered by a 6 V supply, during measurement, the device draws an average current of 19.5 mA. Approximately, 17 mA is consumed by the AD5934, 1.5 mA by the microcontroller, and 1 mA by the analog front-end and the regulator. While the BLE module is advertising and transmitting data, the average current is 6.0 mA and 17.0 mA respectively. Since the AD5934 is in power-down mode, the majority of this current is consumed by the BLE module. In a typical measurement where the complete cycle takes approximately 23 seconds, the total energy consumed is 0.50 mWh.

3.4.4 Discussion

In this section, we discussed the performance of our EIS device. We initially evaluated noise levels and signal quality, confirming stable excitation amplitudes between 28 mV and 30 mV. SNR and THD calculations provided insights into signal quality. We also examined noise at the TIA output and the AD5934 ADC's

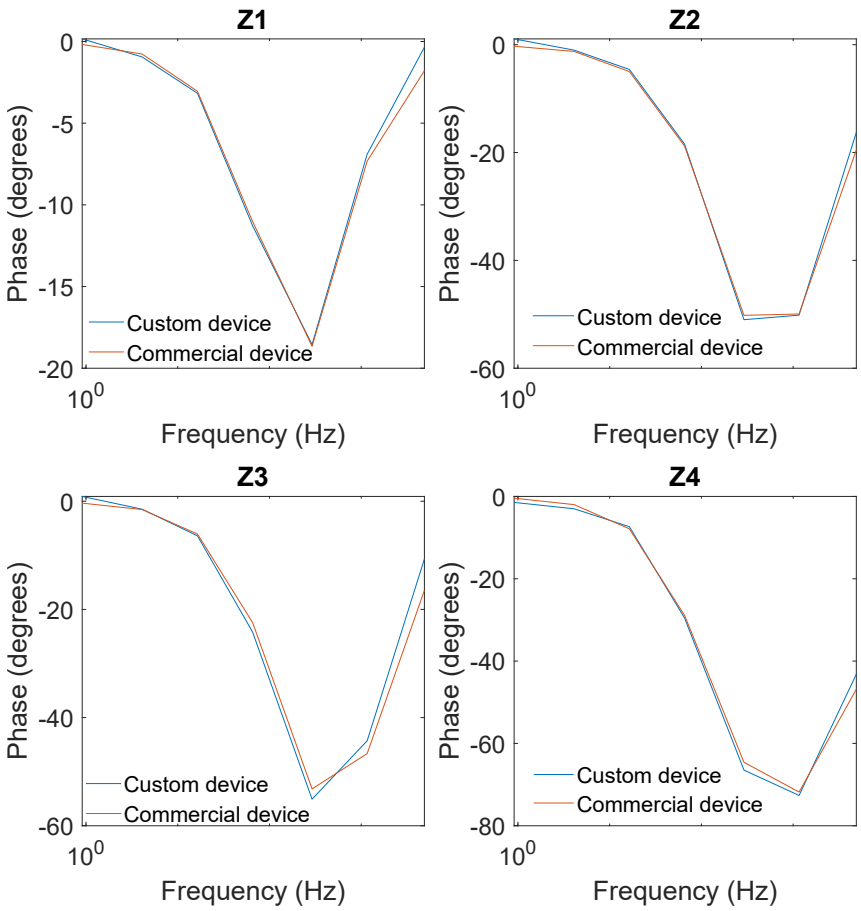

Figure 3.22: Average impedance phases in four R(RC) cells, acquired by the custom and Metrohm devices.

input at different excitation frequencies and TIA feedback settings. Adjustments to gain switching thresholds were made to account for the effect of noise.

For adjusting the gain switching thresholds, the RMS noise was considered. The noise spectrum at the TIA output and the AD5934 ADC's input are not uniform. The distribution of noise affects the Fourier transform calculated by the AD5934 as well as the voltage that is being monitored by the microcontroller. Further characterization of noise and studying its effect on the measurements can provide a way to accurately determine the thresholds for achieving a specified level of accuracy.

The device demonstrated a dynamic range covering resistors from 100 Ωto 180 kΩ, with good accuracy and precision. Impedance measurements on R(RC) cells exhibited repeatability and accuracy, with minor variations compared to a Metrohm potentiostat. Measurements on R(RC) cells with impedances close to cortisol samples show promise that our device will be able to accurately measure impedance in the intended range and distinguish between samples with different R_{ct}s.

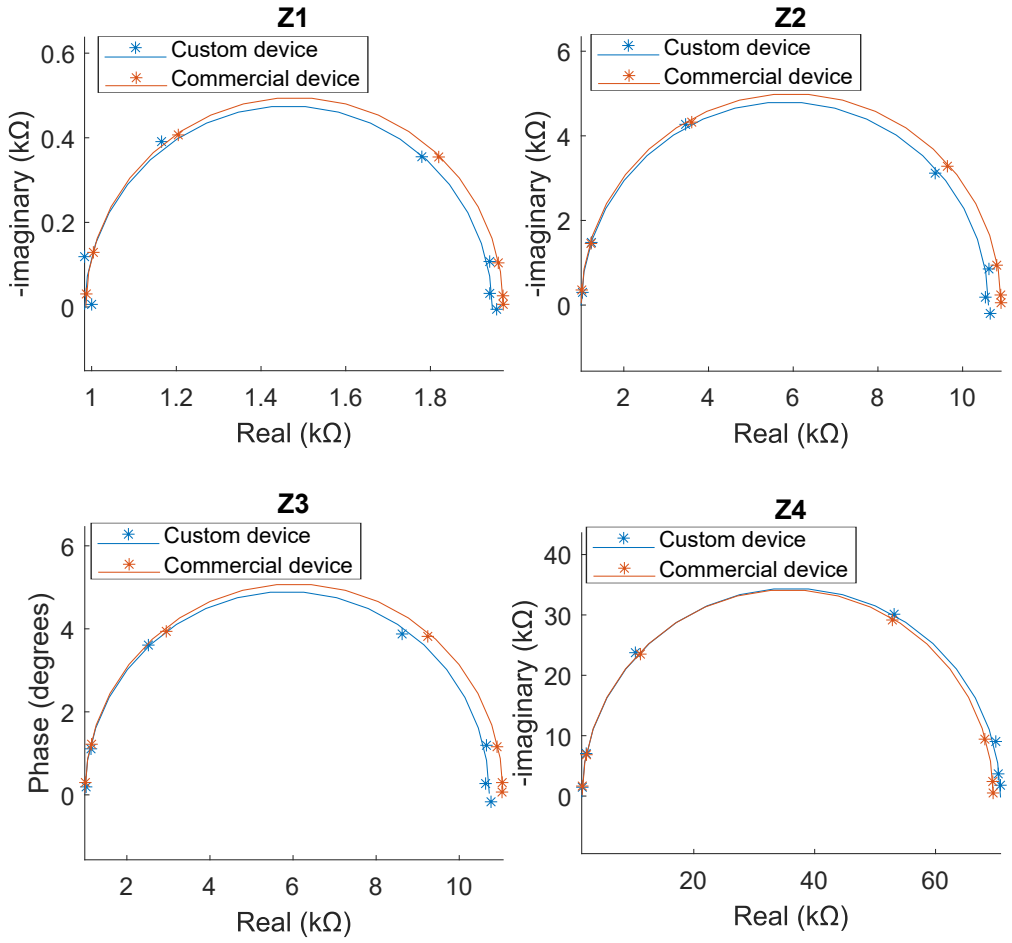

Figure 3.23: Nyquist plots for averaged impedance measurements in four R(RC) cells, acquired by the custom and Metrohm devices. Markers show measured data points, while traces show a circular fit to the data.

The results point to a minor systematic error that can potentially be rectified through calibration. The impedance magnitude is consistently overestimated for higher impedances within the dynamic range and underestimated for the lower ones. However, this error did not affect the system's ability to differentiate resistors and R(RC) cells. The main purpose of the device is to differentiate between samples rather than accurately quantifying the impedance. Also, as it will be revealed in section 3.5, the electrochemical sensors' variability is higher than the errors observed in the characterization measurements. Therefore, we will retain this level of accuracy for the present study.

3.5 Experiments

Experiments were conducted on electrochemical samples to validate the functionality of our custom-designed EIS circuit for 3-electrode impedance measurements. The primary objective is comparing the circuit's performance to a commercial potentiostat, in terms of its capability to differentiate between various electrochemical

Table 3.9: Errors in measured impedance magnitude and phase for four RC cells at each frequency. Potentiostat measurements were used as a reference.

	Magnitude Error (%)				**Phase Error (degrees)**			
f (Hz) \RC cell #	1	2	3	4	1	2	3	4
4880	1.22	-0.19	-0.62	-5.77	1.44	3.26	5.81	3.67
1160	-2.16	1.37	-5.27	2.37	0.43	-0.21	2.37	-0.83
291	-3.34	-2.37	-10.58	-0.49	0.11	-0.81	-1.90	-1.89
65.5	-2.11	-3.19	-5.44	1.2	-0.26	0.36	-1.75	-0.65
16.4	-1.03	-1.76	-2.28	2.54	-0.13	0.39	-0.33	0.51
4.09	-1.58	-3.33	-3.63	1.39	-0.18	0.24	0.07	-1.01
0.909	-0.79	-2.33	-2.39	1.79	0.34	1.36	1.24	-1.04

Table 3.10: Comparison of R1 (equivalent to R_{ct}) measurements between the Metrohm potentiostat and the custom device for R(RC) cells.

	Metrohm			**Custom Device**			
R(RC) Cell #	**Mean (kΩ)**	**STD (Ω)**	**CoV (%)**	**Mean (kΩ)**	**STD (Ω)**	**CoV (%)**	**Error (%)**
1	0.99	0.49	0.05	0.96	3.36	0.35	-3.03
2	9.91	5.95	0.06	9.64	11.6	0.12	-2.77
3	10.07	6.04	0.06	9.78	10.7	0.11	-2.82
4	68.03	176	0.26	69.58	195	0.28	2.28

samples. The following sections present the results of two experiments. In the first experiment samples with varying redox solution concentrations were studied. In the second one, samples had various concentrations of cortisol antigens.

3.5.1 Experimental Setup

The electrochemical sensors used in these experiments were custom-made disposable screen-printed electrodes (SPE) that were developed by the BioMEMS and Bioinspired Microfluidic Laboratory. The SPE consists of a plastic strip with three electrodes. The working and counter electrodes are composed of a hybrid material containing Graphene poly(3,4-ethylenedioxythiophene) polystyrene sulfonate (PEDOT:PSS) and carbon, and the reference is made of silver and silver chloride (Ag/AgCl). During measurement, the SPE's sensing area was covered by a solution containing a redox probe. The redox probe, which was a solution of a Ferrocene/Ferrocyanide couple in phosphate-buffered saline (PBS), allows for current flow and measuring impedance.

In the first experiment, bare SPEs with no antibodies and antigens were used. In each measurement, 15 µL of the redox solution was added on the sensing area of a bare SPE, and EIS was performed. In the second experiment, the SPEs were functionalized with cortisol antibodies and antigens. The SPEs' sensing area was covered with cortisol antibodies. Different concentrations of antigens were applied to some of the electrodes. 7 µL of the 4 mM redox probe was placed on the sensing area during EIS measurements.

3.5.2 Redox Solution Experiments

The impedance of 30 bare SPEs covered with the redox solution was measured. Six concentrations of the redox solution ranging between 0.5 mM to 5 mM were used. Five SPEs were tested for each concentration. EIS measurements on each SPE were done using our custom circuit and a MultiAutolab M204 commercial potentiostat (Metrohm, Switzerland).

To make a fair comparison between the two systems, each disposable SPE was reused and the measurements by the two devices on the same SPE were compared. This approach was adopted due to fabrication-related variations in the SPEs. Even when using the same sensor, the two devices' readings are expected to be different. This is due to electrode reactions caused by the measurement and extended exposure to ambient conditions. Ideally, the impedance change observed when switching between devices should be comparable to the change observed in one device's repeated measurements. To evaluate this, measurement with each device was repeated three times. This means that overall, six EIS scans were carried out on each SPE. To minimize the effect of repeated measurements on the comparison of the systems, the order in which the systems were used was alternated. In three out of five sensors with each concentration, the commercial potentiostat was used first, while in the other two the custom circuit measurements were completed first.

Figure 3.24 illustrates how the experiment was carried out at a specific concentration. In these experiments, an SPE was plugged into the electrode connector of one device. The redox solution was added to the sensor. Then, three measurements were made. Then, the SPE was removed and plugged into the other system's connector, and three more EIS scans were performed. When comparing readings from the two systems, the third and fourth measurements on each sensor (highlighted in the same color in Figure 3.24 (a)) were used. These measurements will be referred to as the sensor's representative measurements. For evaluating variability in one sensor's response, back-to-back readings using the same device were compared.

3.5.2.1 Experiment Results

Figure 3.25 illustrates Nyquist plots of the measured impedances in the redox solution experiment. For each concentration, five sensors' representative measurements (third and fourth scan) by both devices are included. In the two plots corresponding to each concentration, each color represents measurements from one of the five sensors. Plots marked M (left column) are using the Metrohm potentiostat, while plots marked C (right column) are from the custom circuit. The same color was used for each sensor in both plots. The R_{ct} for the five scans shown in each subplot was calculated, and the one with the median R_{ct} was selected to represent the data in each subplot, i.e. a representative Nyquist plot for a given concentration measured by either the Metrohm or custom potentiostat. This leads to two sets of data: six measurements by the custom

(a)

Sensor Index	Measurements
1	$M_{1,1}$ $M_{1,2}$ $M_{1,3}$ $C_{1,4}$ $C_{1,5}$ $C_{1,6}$
2	$C_{2,1}$ $C_{2,2}$ $C_{2,3}$ $M_{2,4}$ $M_{2,5}$ $M_{2,6}$
3	$M_{3,1}$ $M_{3,2}$ $M_{3,3}$ $C_{3,4}$ $C_{3,5}$ $C_{3,6}$
4	$C_{4,1}$ $C_{4,2}$ $C_{4,3}$ $M_{4,4}$ $M_{4,5}$ $M_{4,6}$
5	$M_{5,1}$ $M_{5,2}$ $M_{5,3}$ $C_{5,4}$ $C_{5,5}$ $C_{5,6}$

(b)

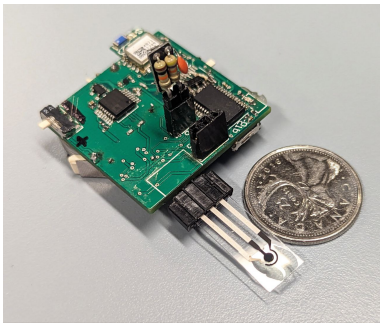

Figure 3.24: EIS experiment setup. (a) Order of measurements of a specific redox solution concentration in 5 sensors. $M_{i,j}$ and $C_{i,j}$ represent one measurement made by the Metrohm potentiostat and our custom circuit respectively. i is the sensor index number, and j is the measurement number. The measurements that are highlighted by the same color were used as the representative measurement for the sensor by each device. (b) EIS experiment setup using the custom circuit.

circuit, one for each of the six concentrations, and six measurements by the commercial potentiostat, one for each of the six concentrations. Nyquist plots for this data are shown in figure 3.26.

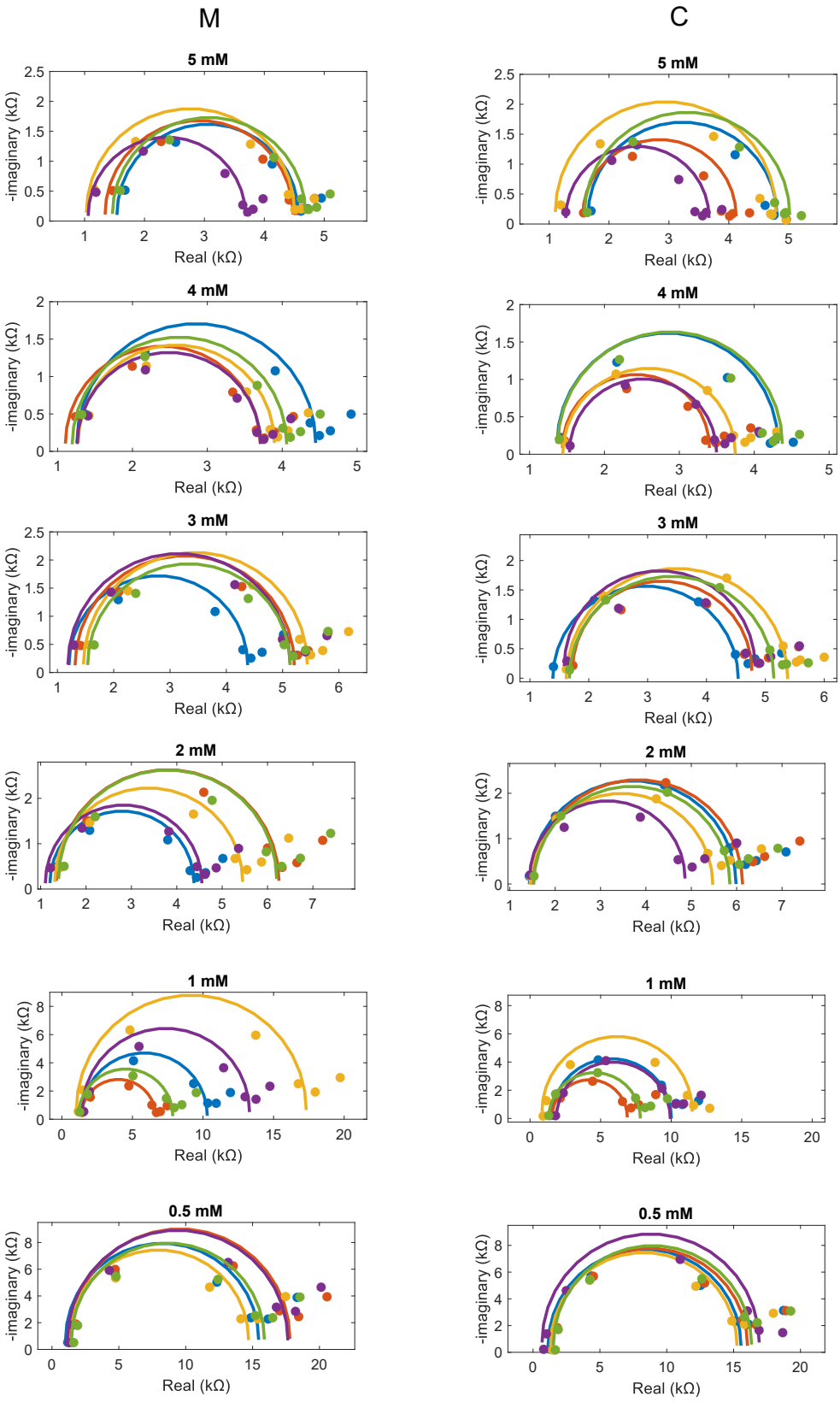

Figure 3.25: Nyquist plots for the representative measurements (third and fourth scan) of the impedance of six redox solutions with concentrations of 0.5 mM to 5 mM, each measured with 5 sensors, each shown in a different color. M and C columns include Metrohm potentiostat's and our custom circuit's measurements respectively.

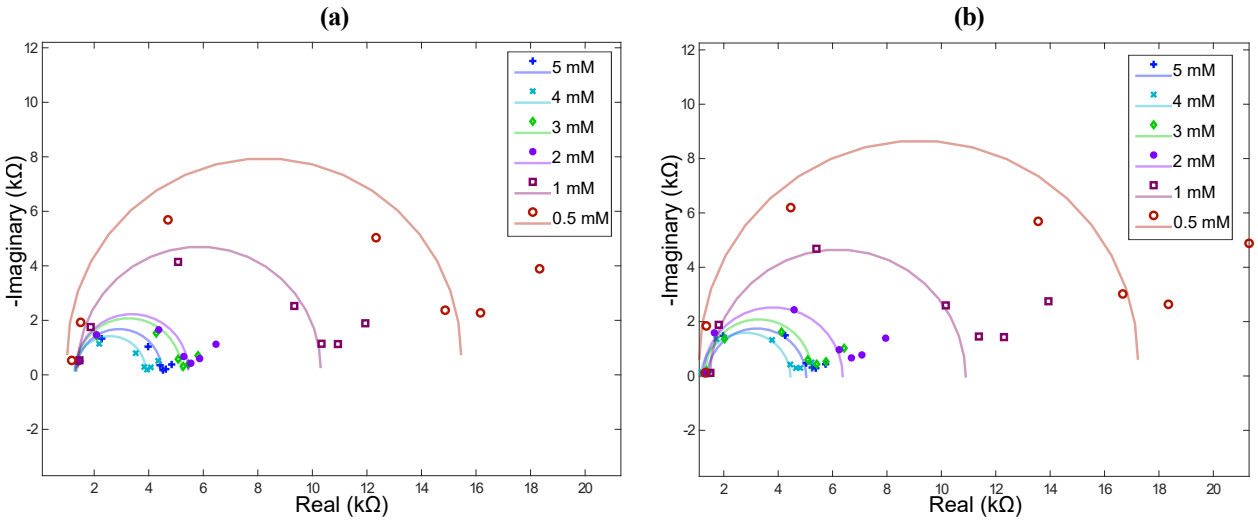

Figure 3.26: Nyquist plots for the impedance of six redox solutions with concentrations of 0.5 mM to 5 mM, (a) measured by the commercial potentiostat, (b) measured by our EIS circuit. The sample with the median R_{ct} over the five trials was chosen as the representative for each concentration. The markers show the measured impedances while the curves are the semicircles fitted to the data.

Figure 3.27 (a) and (b) show R_{ct} against concentration for all five sensors' representative measurements by the Metrohm potentiostat and our EIS device. Figure 3.27 (c) shows the R_{CT} measured by the custom circuit, against the commercial potentiostat's measurement where each data point corresponds to one sensor. A linear regression model was fitted to the data. A slope of 1.06 and intercept of 0.087 with a coefficient of determination (R^2) of 0.97 indicate that the two device's measurements are very similar.

To provide a more clear comparison between the two systems' measurements, Figure 3.28 (a) illustrates the fitted data from Figure 3.26 on the same plot. In Figure 3.28 (b), the relative changes in R_{ct} measured by the two systems are plotted against concentration on a logarithmic scale. Since 4 mM samples were indistinguishable from 5 mM samples, the mean R_{ct} in samples with a concentration of 4 mM or 5 mM was selected as the reference. To obtain a calibration curve, linear regression models were fitted to the logarithm transformed data. That is:

$$\ln \Delta R_{ct} = a \cdot \ln C + b \tag{3.22}$$

Where C is the concentration, and a and b are constant. For the custom device and the commercial potentiostat, R^2 was 0.912 and 0.832 respectively. This shows that this model can effectively explain the relation between concentration and the R_{ct}. The slopes were -1.7154 and -1.674, showing a similar trend in the two systems' measurements.

Table 3.11 shows a comparison of the two device's performance in this experiment. Cohen's distance (d)

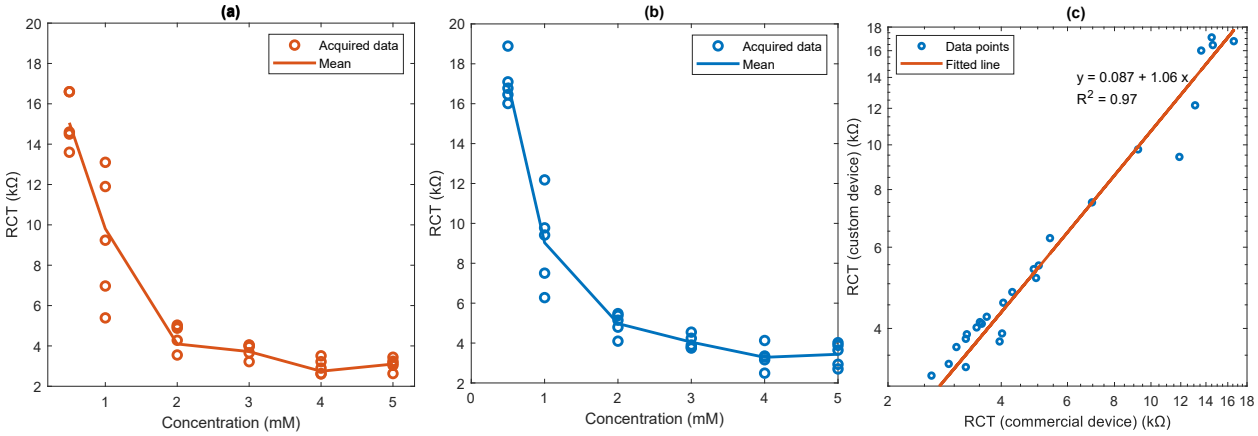

Figure 3.27: (a) The R_{ct} of six concentrations of redox solutions each measured in five sensors (a) by the commercial potentiostat, and (b) by our EIS circuit. (c) The circuit's R_{ct} measurements plotted against the commercial potentiostat measurements.

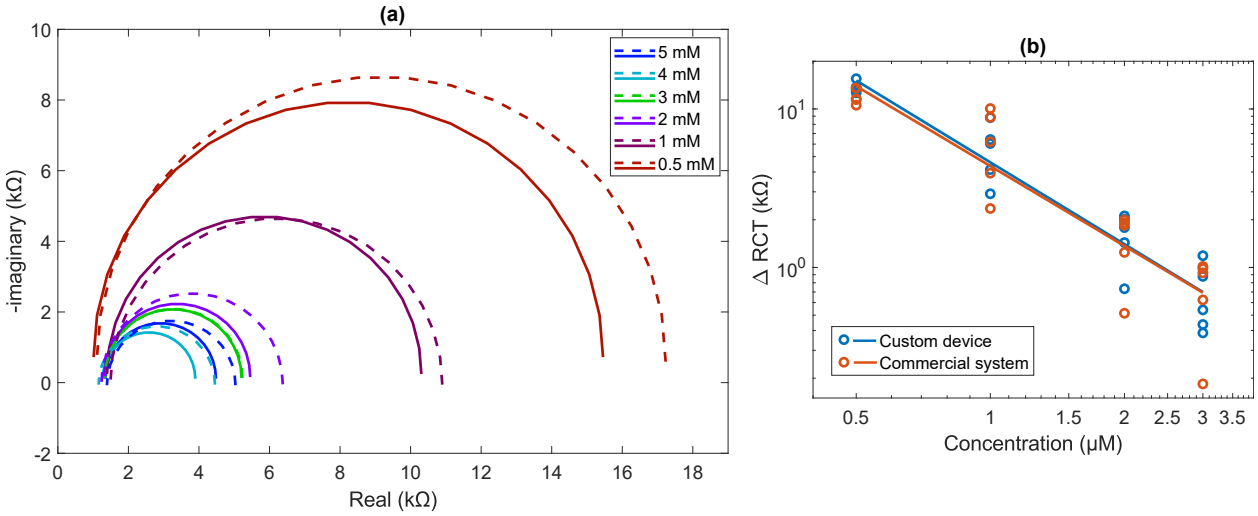

Figure 3.28: (a) Nyquist plots of semicircles fitted to impedance data from sensors with the median R_{ct} for each concentration of redox solution. Solid lines and dashed line show the measurements by the commercial potentiostat and the custom device respectively. (b) Relative R_{ct} of four concentrations each measured in five sensors by both systems. ΔR_{ct} indicates the change in R_{ct} relative to the mean R_{ct} of sensors with a 4 or 5 mM redox solution.

was used as a measure for the systems' ability to distinguish the concentrations. The distance was calculated between adjacent concentrations. Thus, Cohen's distance here shows how different the impedance for the concentration in a given column is comparing to the impedance for the higher concentration in the adjacent column. The negative Cohen's distances in the 4 mM columns show that neither device was able to detect an increase in impedance. For concentrations with a positive Cohen's d, the custom circuit had a better performance with an average distance of 2.64 comparing to 1.91 for the Metrohm potentiostat.However, to account for uncontrolled variation of experimental conditions, more experiments are required to make a statistically significant comparison. Despite this limitation, this experiment provides preliminary evidence

of the custom circuit's ability to perform EIS on these samples with a similar performance to the commercial potentiostat.

Table 3.11: Comparison of measurement of redox solutions' R_{ct} using the Metrohm potentionstat (M) and our custom circuit (C). Conc., STD, CoV, and Cohen's d are concentration, standard deviation, coefficient of variation, and Cohen's distance respectively.

Conc.	5 mM		4 mM		3 mM		2 mM		1 mM		0.5 mM	
Mevice	M	C	M	C	M	C	M	C	M	C	M	C
Mean(kΩ)	3.14	3.44	2.62	3.29	3.90	4.05	4.14	4.98	8.91	9.03	14.44	17.04
STD (kΩ)	0.31	0.59	0.29	0.58	0.34	0.34	0.78	0.56	4.39	2.27	1.34	1.11
CoV	9.9%	17.1%	11.0%	17.75%	8.7%	8.4%	18.8%	11.2%	49.3%	25.1%	9.3%	6.5%
Cohen's d	-	-	-1.72	-0.26	4.04	1.59	0.41	2.01	1.51	2.46	1.70	4.49

As mentioned earlier, the sensor response changes as the measurement is repeated. To evaluate this variation, for each SPE, the percentage change in R_{ct} in back-to-back measurements with the same device were calculated based on equation 3.23 (Refer to Figure 3.24 (a)). This change (Δ), was calculated in all adjacent measurements on the same device ($0 < i < 6$, $0 < j < 3$).

$$\begin{aligned} \Delta_{M_{i,j+1}} &= \frac{R_{ct_{M_{i,j+1}}} - R_{ct_{M_{i,j}}}}{R_{ct_{M_{i,j}}}} \cdot 100 \\ \Delta_{C_{i,j+1}} &= \frac{R_{ct_{C_{i,j+1}}} - R_{ct_{C_{i,j}}}}{R_{ct_{C_{i,j}}}} \cdot 100 \end{aligned} \tag{3.23}$$

In the custom device's measurements, the change in the calculated R_{ct} fell within the range of -14.1% to 13.3% (1.7% on average, with STD of 5.2%). Meanwhile, in Metrohm potentiostat measurements, this variation spanned from -24.9% to 16.3% (2.0% on average, with STD of 6.9%). This difference may be attributed to the custom circuit's shorter excitation period (23 s vs 77 s), which may have less impact on the samples during each measurement. Additional data is required for a statistically significant comparison.

As evident in Figure 3.27, the R_{ct} for sensors' representative measurements by the two devices are somewhat different. This difference could be due to the effect of repeated measurements on one sensor. If that is the case, this variation should be comparable to the variation observed in each device's back-to-back measurements. To evaluate this, the R_{ct} for each sensor's representative measurements by the two devices were compared. Excluding two cases with an unusually high difference of approximately 68%, the remaining comparisons showed differences ranging from -25.2% to 20.6% (9.0% on average, with STD of 12.3%). This variation is larger than the change observed in one device's measurements (1.7% average, 5.2% STD for the custom device, and 2.0% average, 6.9% for Metrohm potentiostat). This difference may be due to the experimental conditions affecting the sensor impedance when switching between devices.

3.5.3 Cortisol

The impedance of blank SPEs and SPEs functionalized with three concentrations of cortisol antigens (5, 10 and 20 ng/mL) were measured by the commercial and custom systems. A blank SPE refers to an SPE with cortisol antibodies, but no antigens. To measure impedance, the redox solution was 'pipetted on to the sensing area. Similar to the redox solution experiment, impedance was measured for a total of six times on three electrodes of each concentration: three times with the commercial potentiostat, and three times with the custom circuit.

3.5.3.1 Experiment Results

The representative data, 3rd and 4th measurements, as defined earlier, on each of the 12 SPEs are included in Figures 3.29, 3.30, and 3.31.

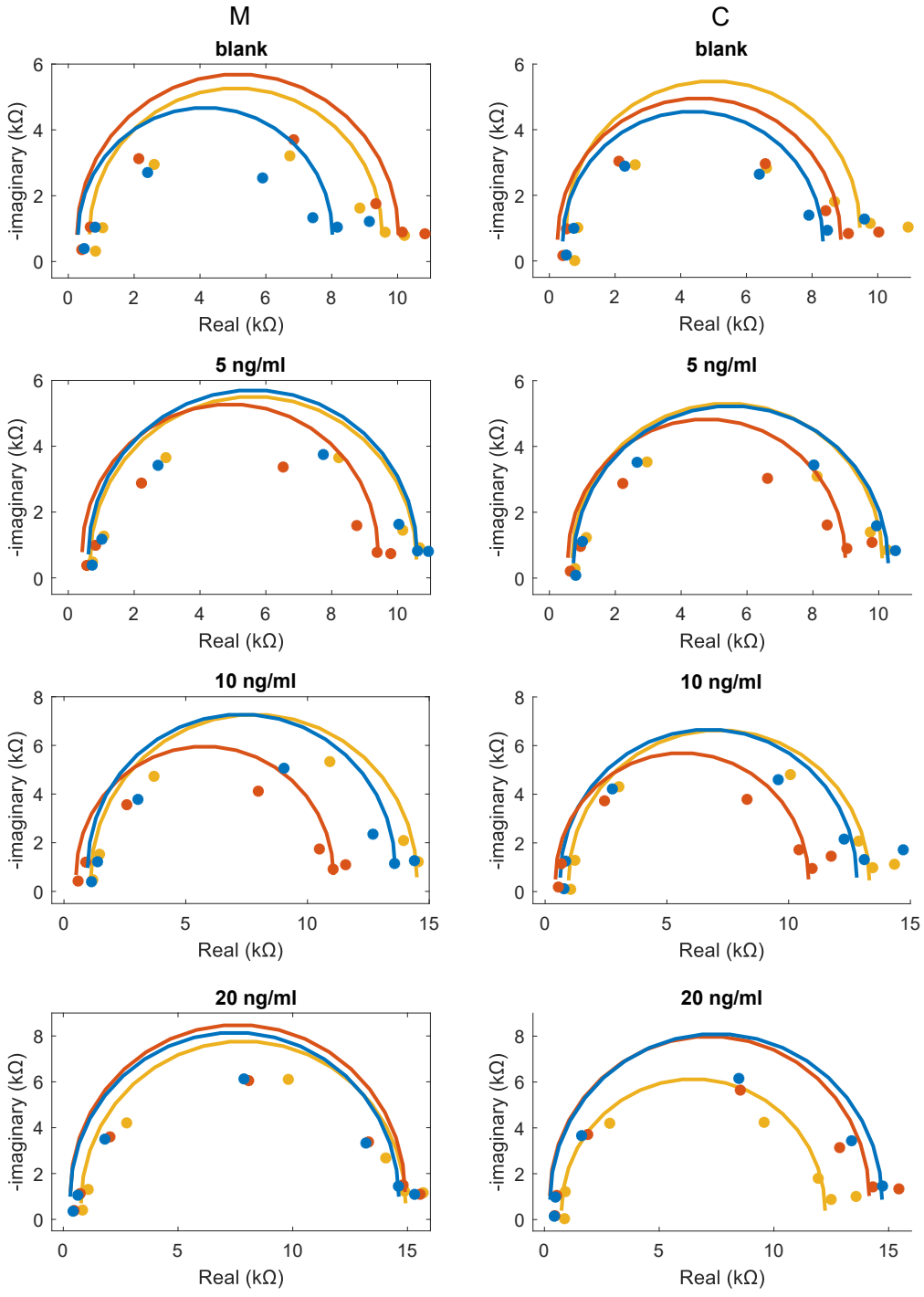

Figure 3.29: Nyquist plots for the representative measurements (third and fourth scan) of the impedance of samples with four concentrations of cortisol antigens between 0 and 20 ng/ml, each measured with 3 sensors, each shown in a different color. M and C represent Metrohm potentiostat's and our custom circuit's measurements respectively.

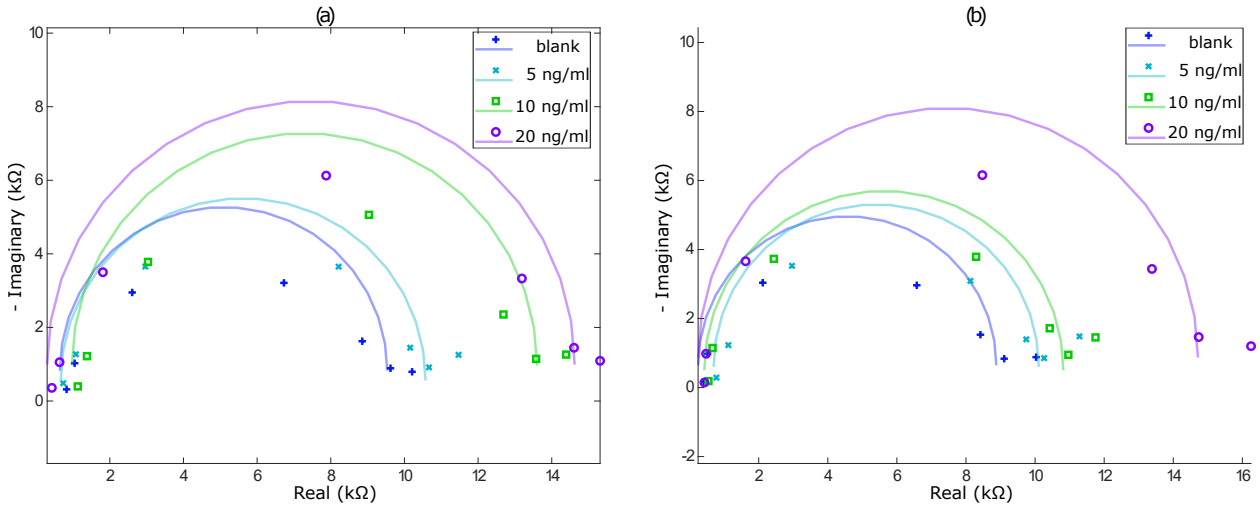

Figure 3.30: Nyquist plots for the impedance of samples with four concentrations of cortisol antigens between 0 and 20 ng/ml, (a) measured by the commercial potentiostat, (b) measured by our EIS circuit. The sample with the median R_{ct} over the three trials was chosen as the representative for each concentration. The markers show the measured impedances while the curves are the semicircles fitted to the data.

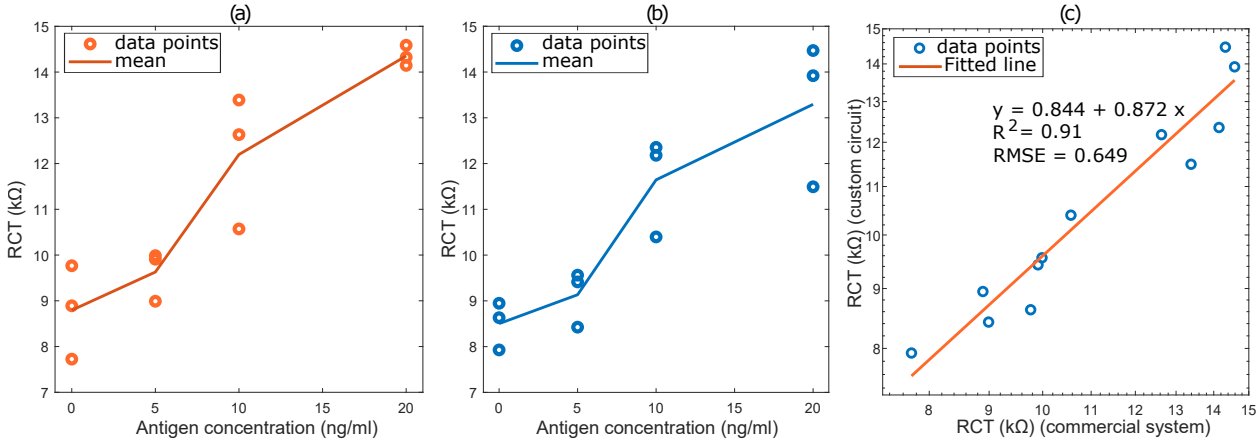

Figure 3.31: (a) R_{ct} of four samples (blank and three concentrations of cortisol antigens) each measured in three sensors (a) by the commercial potentiostat, and (b) by our EIS circuit. (c) EIS circuit R_{ct} measurements plotted against the commercial circuit measurements.

Similar to Figure 3.28, Figure 3.32 shows a comparison between the two systems' fitted Nyquist plots. In Figure 3.32 (b), the measured change in R_{ct} with reference to blank samples measured by the two systems are plotted against concentration on a logarithmic scale. To obtain a calibration curve, linear regression models were fitted to the logarithm transformed data, with the an relative R_{ct} and logarithm of the concentration as the dependent and independent variables respectively. That is:

$$\Delta R_{ct} = a \cdot \ln C + b \tag{3.24}$$

Where C is the concentration, and a and b are constants. For the custom device and the commercial

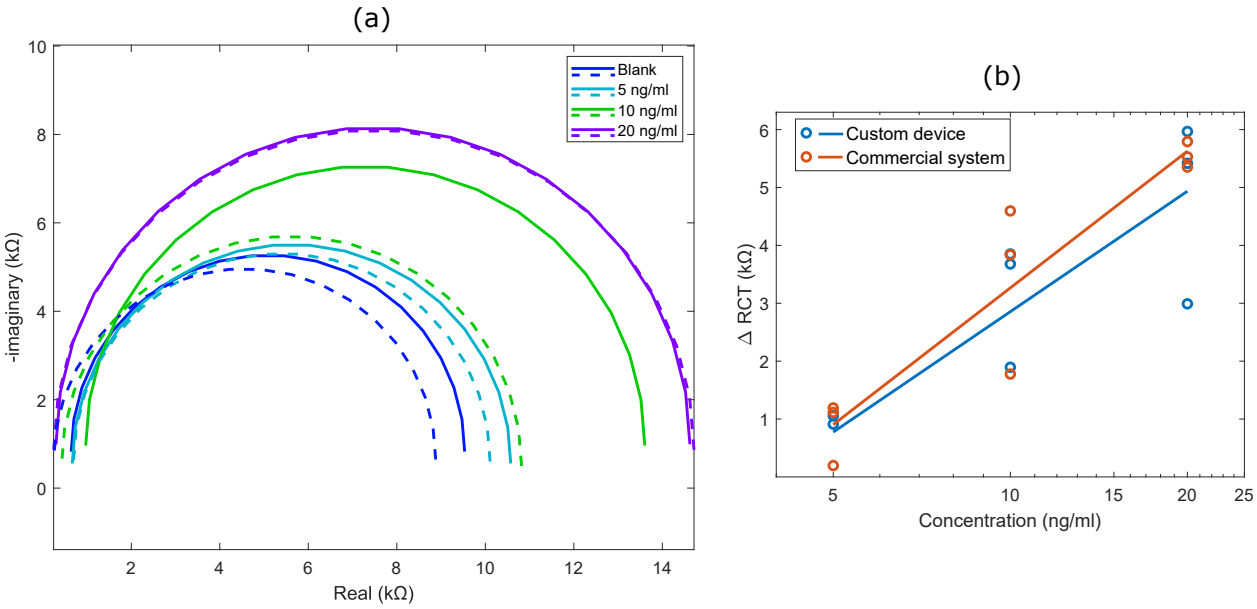

Figure 3.32: (a) Nyquist plots of semicircles fitted to impedance data from sensors with the median R_{ct} for each concentration of cortisol antigens. Solid lines and dashed line show the measurements by the commercial potentiostat and the custom device respectively. (b) Relative R_{ct} of three concentrations each measured in three sensors by both systems. ΔR_{ct} indicates the change in R_{ct} relavtive to the mean R_{ct} of a blank sensor.

potentiostat the R^2 was 0.753 and 0.869 respectively. In comparison to the redox solution experiment, R^2 was lower for our device, and there was a larger difference between the slopes (3.0012 and 3.4075). This may be due to the limited dataset, and the samples being more prone to deterioration. Note that this logarithmic relation is often observed in EIS for immunosensing [94–96].

For each of the four samples, only data for three sensors are available. Due to the limited data set, conventional statistics like mean and standard deviation may not provide a reliable assessment of the data's properties. However, even with this constraint, a trend in impedance can be observed. The data suggests that as the concentrations of antigens increase, there is a noticeable rise in impedance, and this increase was detectable by both the commercial and custom systems. However, additional data is required in order to quantify cortisol samples' impedance dependency on its concentration, and to make a statistically significant comparison between the two systems.

Similar to the previous experiment, a linear regression model was fitted to the R_{ct}s to relate the devices' measurements to each other (Figure 3.31 (c)). The model had a slope of 0.87 and R^2 of 0.91. This demonstrates that a linear model effectively captures the relationship between the measurements obtained from the two devices, with the custom device's R_{ct}s being slightly lower. Compared to the redox solution experiments, the sample size in this experiment is smaller. Also, antibodies and antigens are more prone to deterioration which changes the samples' impedance. This can explain the smaller R^2. The slope in the

model is 0.87 with a 95% confidence interval of 0.69 to 1.05. This means that a slope of 1.00 falls within the plausible true slope range for the population.

Similar to the redox solution experiments, the R_{ct}'s change (Δ) in back-to-back measurements from the same sensor by the same device were calculated (See equation 3.23). In back-to-back measurements using the Metrohm potentiostat, on average, the calculated R_{ct} changed by -1.6% (STD of 6.0%), and by -1.3% on average (STD of 4.8%) for the custom circuit. The change when switching to a different device was -1.7% on average (STD of 6.0%), which is similar to the average changes observed within each devices' measurements.

3.5.4 Discussion

In this section, two sets of experiments with bare and functionalized SPEs were carried out. The data was analyzed to evaluate the system's ability to differentiate between different concentrations or cortisol antigens or redox probes. The measurements' repeatability was also studied. The performance of our custom EIS device was compared to a commercial Metrohm potentiostat.

In both experiments, noticeable variation was present in measurements from different SPEs with the same concentration of the analyte. One reason is the variation in the electrode manufacturing process. Additionally, during the experiments, the sensors can be exposed to air and room temperature for different durations of time. In the second experiment, functionalizing SPEs was done manually, and variations in the process are possible. And finally, The redox solution's placement on the sensor was manual and varied.

In the experiments with bare SPEs (only containing redox probe), the two devices' measurements were closely matched. This was shown by a linear regression model with a slope of 1.06 and R^2 of 0.97, relating the custom device's calculated R_{ct}s the the commercial potentiostat's. Both systems were able to differentiate between concentrations of 0.5 mM to 4 mM. However, the increase in concentration from 4 mM to 5 mM was indistinguishable. Disregarding the 5 mM measurements, the custom device showed better differentiation with the higher average Cohen's distance in calculated R_{ct}s of adjacent concentrations (2.64 comparing to 1.91).

The calibration curve obtained from the two devices' measurement were also comparable. For both devices, relative R_{ct} with reference to a 5 mM to 4 mM baseline (ΔR_{ct}) increased exponentially with decreasing concentration. There was a 2% difference between the exponent terms in the models for the two devices (-1.71 comparing to -1.67). Large R^2 of 0.91 for our device and 0.83 for the commercial system showed that the exponential model effectively explains the relationship between ΔR_{ct} and concentration.

The R_{ct} change in back-to-back measurements of the same sensor was comparable for the two devices, with the custom device showing slightly less variation, potentially due to its shorter measurement time (23 s

comparing to 77 s). However, this change was considerably larger when switching devices for measuring the same electrode. A portion of this between-device change can be attributed to the inherent variability observed in multiple measurements on the same sensor. Some variability may be attributed to factors such as the physical handling of electrodes during transitions between devices, potential sample displacement, or extended exposure to ambient conditions. Results of the characterization tests with R(RC) cell support this claim, as they showed a marginal difference between the two devices' measurements.

Overall, despite the small sample size, findings from this experiment suggest that our custom EIS device can perform EIS on these samples, with a similar performance to the commercial potentiostat.

Similar experiments with functionalized SPEs were carried out. An increase in impedance was observed with increasing cortisol concentration. However, due to the small sample size (three for each concentration), Cohen's distance was not deemed a suitable metric for a fair representation of samples' differentiation.

A linear model could relate our custom device's R_{ct}s to the commercial potentiost's with an R^2 of 0.91. The linear model's slope of 0.87 with a 95% confidence interval of 0.69 to 1.05 suggests the two device's measurements are similar.

The calibration curves were obtained from this experement. For both devices, relative R_{ct} with reference to blank SPEs (ΔR_{ct}) increased with increasing concentration on a logarithmic scale. The logarithm coefficient (a in equation **??**) was 3.00 for our device and 3.41 for the commercial one (12% difference). Comparing to the redox solution experiments, R^2 was smaller for our device (0.75), and slightly larger for the commercial potentiostat (0.87). Note that in this experiment, only three concentrations of cortisol antigens were tested, and for each concentration, three samples were measured. Therefore, more experiments are required to reliably determine the relationship between concentration and ΔR_{ct}. However, these experimental results provide evidence of this relationship and suggest that our device is able to detect it.

Unlike the redox solution experiments, in back-to-back measurements using the Metrohm potentiostat, on average, the calculated R_{ct}'s changes within both devices' measurements was similar to the changes observed when switching devices. This shows no evidence of an inherent difference between the devices, and implies that the differences between measurements can be mostly due to the properties of the samples and sensors rather than the devices' performance.

Overall, the results of these experiments show evidence that our custom EIS device has a similar performance to a commercial one when measuring the R_{ct} of the electrochemical samples of our interest.

3.6 Summary and Conclusion

This chapter presented the design, characterization, and validation of an electrochemical impedance spectroscopy system for measuring cortisol concentration. The impedance measurement circuit was designed as a compact PCB with three operating modes including calibration, 2-terminal impedance, measurement, and 3-electrode EIS.

The circuit utilizes an AD5934 impedance converter for measuring impedance at seven frequencies ranging from 0.9 Hz to 4880 Hz. Amplifiers and filters using commercially available op-amps were used to condition the excitation voltage and response current. A microcontroller was used to control the impedance converter, control the circuit gain, and handle communication. Adaptive gain was implemented to increase the device's dynamic range. To select the appropriate gain, the response signal was monitored to confirm that it is within the detectable range for the impedance converter. In case the response signal was too small, the gain was increased and vice versa.

The device is battery powered and wireless. The impedance converter's data and gain settings are transmitted to a connected device via Bluetooth Low Energy. The data is processed in MATLAB to determine impedance at each frequency. Additionally, in electrochemical measurements, the charge transfer resistance is calculated in MATLAB as an indication of the sample's composition.

Characterization tests on resistors and RC cells demonstrated that device's dynamic range, accuracy, and precision were appropriate for detecting measurement of cortisol concentration. Our device's EIS capabilities were also validated in experiments on electrochemical samples containing various redox solution concentrations as well as various cortisol concentrations. The experiments were also done by using a commercial potentiostat, and compared to our custom EIS system. These experiments demonstrated that our device has a performance similar to that of a commercial potentiostat. These experimental results reveal the device's potential for long-term semi-continuous cortisol monitoring.

The objective of this project was to develop a compact wireless electronic circuit that could perform EIS in order to measure cortisol concentration. This research successfully achieved its objectives. The excitation signal characteristics and gain were optimized for cortisol sample analysis. The device has a compact and potentially wearable form factor, and is powered by a battery suitable for semi-continuous daily use. Furthermore, the system supports wireless data transfer and ensures quick measurements, which are completed well within the intended two minutes.

3.6.1 Future Work

Future work can involve expanding and enhancing the capabilities of the impedance measurement system. Several key areas can be explored:

Data Collection and Statistical Testing: A calibration curve can be created to relate impedance measurements to cortisol concentrations. However, this requires a larger data set. With a larger dataset, statistical tests can be used to better evaluate the device's performance in terms of accuracy and precision of cortisol measurements.

Microfluidic Integration: Integration with microfluidic chips would help minimize exposure to air, ensuring more consistent and reliable measurements. Microfluidic devices can also enable automated sample collection and handling. Comparing to pipetting samples in sensors, microfluidics can lead to less experimental variations.

Optimization for Specific Ranges: Depending on the target application, the system can be optimized for specific impedance ranges. This optimization may allow removing multiple gain and calibration options, leading to a simplified and more compact design. Focusing on a narrower impedance range can lead to higher measurement precision and sensitivity.

Form Factor Adaptation: The design can be adapted to different form factors, such as wearable devices that can be placed on various parts of the body or portable units for point-of-care measurements.

Mobile App Development: A mobile application can be developed to collect, process, store, and visualize the device's data, making the system more user-friendly and accessible for non-experts.

Adaptation for Other Analytes: The system may be adapted for the detection of other analytes beyond cortisol. This expansion could open up opportunities for broader applications in healthcare monitoring.

Chapter 4

Conclusion

In this thesis, we developed two distinct biomedical measurement systems, both utilizing the AD5934 impedance converter — a chip that can generate sinusoidal excitation signals, measure system responses, and calculate the Fourier transform to determine the system response signal's amplitude. While this chip is designed for impedance spectroscopy, we demonstrated its versatility by using it in a fiber photometry system in addition to an impedance spectroscopy device.

In the fiber photometry project, the AD5934 was used in order to enable amplitude modulation. By using sinusoidally modulated excitation light, driven by the AD5934's conditioned excitation voltage, it is possible to distinguish between signals corresponding to different excitation sources based on their modulation frequency. In this project, two AD5934s operating at their distinct modulation frequencies were used. One for the main neural activity-dependent signal, and one for an isosbestic control signal. The AD5934 has a DSP module that calculates the single-point DFT of its input signal. This simplified the process of calculating the amplitude of the signals corresponding to the fluorescent emission.

In *in vivo* footshock experiments, the AD5934-based electronics successfully generated excitation signals for causing fluorescent emission in mouse brains, and quantified the resulting fluorescent emission. The calculated $\Delta F/F$ was mostly in agreement with measurement results using a commercial fiber photometry system. In GCaMP experiments, there was a noticable difference between the second channel's response. For our setup, there were peaks in the second channel corresponding to footshocks. This was likey due to the cross-talk between the channels as the two excitation frequencies were close to eachother. Although after correcting the frequencies, this cross-talk wasn't observed in the FITC experiment, more experiments are required to confirm that this issue has been eliminated.

Overall, despite the afformentioned limitation, this project successfully met its primary aim, which was

designing a fiber photometry system, powered by a 6 V voltage source, that is capable of recording neural activity in mice using optical excitation powers below 10 μW, while mitigating motion artifacts and correcting for the photodetector's gain variations. Compared to previous photometry systems employing either low optical excitation powers or low supply voltages, our setup combines both advantages with relatively low optical and electrical power requirements.

In the EIS project, the impedance converter was used in its original intended application. The impedance converter's generated signal was conditioned and applied to a sample or device. The resulting current was converted to voltage and conditioned and then sampled by the chip. The impedance at a range of frequencies was calculated based on the chip's data. While the AD5934's datasheet shows the application as measuring impedance between two terminals, we interfaced the chip with a three-electrode electrochemical sensor by an analog front-end. This enabled the device to make three-electrode potentiostatic measurements on electrochemical samples. The device's dynamic range was extended by using adaptive gain. The frequency range of the chip was extended by configuring the chip's input clock frequency.

In electrochemical measurements, the device's performance was similar to a commercial potentiostat. However, the the difference between the two devices' measurements was significanly larger than the measurements with resistor-capacitor cells. This difference was more pronounced in the cortisol experiments. Multiple sources of error contribute to this variation. First of all, unlike electronics elements, exciting electrochemical samples changes their properties. Reactions at the electrode surface continuesly affect the sensors' impedance. Therefore, it is expected to observe different values for the impedance on repeated meaurements on the same sensor.

Additionally, the SPEs used in this experiment must be vacuum sealed and kept at sub-zero temperatures to maintain their properties. During the experiment, these SPEs were exposed to air and ambient temperatures for different periods of time. Also, because of the small volume of the analyte added, evaporation can have a significant affect on the samples. Moreover, cortisol samples are biologically active and more likely to deteriorate when exposed to ambient temperatures. Overall, as the experiment progressed, the sensors' and samples' properties were affected. Physical handling of the sensors can also affect the impedance. As the SPE is removed from one connector and plugged into the other one to switch between the two systems, the redox sample can move on the sensor surface. Also, the printed contacts of the sensor may be scratched.

There is also significant variation between different sensors' impedance. In part, this is due to exposure to ambient conditions for different durations of time and physical handling of the sensors. In this experiment, no mask was placed on the sensor, and samples were drop-cast on the sensing area. This process was done manually and there were variations in the sample placement on the sensor. In fact, the entire sensor functionalization process was manual and variations in the process are expected. Finally, the SPE

manufacturing process can introduce variations in the sensor properties.

Despite these limitations, our EIS device successfully met its aims. It was compact, battery-powered, and wireless, and was capable of distinguishing between samples containing different concentrations of cortisol. Table 4.1 shows a comparison between our device and previous standalone wearable cortisol sensing devices mentioned in Section 3.2.2. Our wireless device has a comparable size and requires similar sample volumes as state-of-the-art devices. However, there is need for additional experiments with broader concentration ranges of cortisol in sweat samples as opposed to in phosphate buffered saline (PBS).

Table 4.1: Comparison of different cortisol sensing platforms. Conc. is short for concentration. Note that the concentration does not necessarily indicate the dynamic range of the systems, but rather the cortisol concentration of samples in the study.

Year, Author	**Sensor**	**Method**	**Sample Volume**	**Conc. Range**	**Wireless**	**Recognition Element**	**Sample**
Rice et al., 2019 [87]	Interdigitated Electrode	EIS and CA	5 μL	1-151 ng/mL	No	Cortisol Antibody	Human Sweat
Torrente-Rodriguez et al., 2020 [88]	Flexible Graphene Electrodes	EIS	10 μL	0-5 ng/mL	Yes	Cortisol Antibody	Human Sweat
Churcher et al., 2020 [89]	Flexible Porous Gold Sensors	EIS	2 μL	1-256 ng/mL	No	Aptamers	Human Sweat
Wang et al., 2022 [90]	Flexible Field-Effect Transistor (FET) Biosensor Array	FET-based	Not specified	1 pM to 1 μM	Yes	Aptamers	Artificial and Human Sweat
This Work	Flexible Carbon SPEs	EIS	7 μL	5-20 ng/mL	Yes	Cortisol Antibody	Cortisol in PBS

In conclusion, these projects highlight the adaptability and effectiveness of the AD5934, in applications involving measurement of a system's response to sinusoidal excitation.

Bibliography

[1] "Texas Instruments AD5934 impedance converter datasheet." https://www.analog.com/media/en/technical-documentation/data-sheets/AD5934.pdf.

[2] B. Stadnyk and Y. Khoma, "Improving the accuracy of the single chip impedance analyzer for sensor applications," *Sensors & Transducers*, vol. 150, pp. 27–31, 03 2013.

[3] P. Ibba, M. Crepaldi, G. Cantarella, G. Zini, A. Barcellona, M. Rivola, M. Petrelli, L. Petti, and P. Lugli, "Design and validation of a portable ad5933–based impedance analyzer for smart agriculture," *IEEE Access*, vol. 9, pp. 63656–63675, 2021.

[4] P. Ibba, M. Crepaldi, G. Cantarella, G. Zini, A. Barcellona, M. Petrelli, B. D. Abera, B. Shkodra, L. Petti, and P. Lugli, "Fruitmeter: An ad5933-based portable impedance analyzer for fruit quality characterization," in *2020 IEEE International Symposium on Circuits and Systems (ISCAS)*, pp. 1–5, 2020.

[5] J. M. M. Luna, A. M. Luna, and R. E. H. Fernández, "Characterization and differentiation between olive varieties through electrical impedance spectroscopy, neural networks and iot," *Sensors*, vol. 20, no. 20, 2020.

[6] M. Simić, G. M. Stojanović, L. Manjakkal, and K. Zaraska, "Multi-sensor system for remote environmental (air and water) quality monitoring," in *2016 24th Telecommunications Forum (TELFOR)*, pp. 1–4, 2016.

[7] Y. Liang, Y. Chen, Z. Zhang, and Q. Feng, "Experimental evaluation of miniature impedance board for loosening monitoring of the threaded pipe connection," *Frontiers in Physics*, vol. 9, 2021.

[8] N. Kaur, S. Bhalla, R. Shanker, and R. Panigrahi, "Experimental evaluation of miniature impedance chip for structural health monitoring of prototype steel/rc structures," *Experimental Techniques*, vol. 40, no. 3, p. 981–992, 2016.

[9] D. J. I. Seunghee Park, Benjamin L. Grisso and C.-B. Yun, "Mfc-based structural health monitoring using a miniaturized impedance measuring chip for corrosion detection," *Research in Nondestructive Evaluation*, vol. 18, no. 2, pp. 139–150, 2007.

[10] M. Snajdarova, S. Borik, and I. Cap, "Design of measurement device for impedance cardiography," in *2017 18th International Conference on Computational Problems of Electrical Engineering (CPEE)*, pp. 1–4, 2017.

[11] P. S. H. Jose, K. Rajasekaran, P. Rajalakshmy, and B. Jebastina, "A non-invasive method for measurement of blood glucose using bio impedance technique," in *2019 2nd International Conference on Signal Processing and Communication (ICSPC)*, pp. 138–142, 2019.

[12] C. Qiu, F. Wu, W. Han, and M. R. Yuce, "A wearable bioimpedance chest patch for real-time ambulatory respiratory monitoring," *IEEE Transactions on Biomedical Engineering*, vol. 69, no. 9, pp. 2970–2981, 2022.

[13] Y. Liu, M. Xia, Z. Nie, J. Li, Y. Zeng, and L. Wang, "In vivo wearable non-invasive glucose monitoring based on dielectric spectroscopy," in *2016 IEEE 13th International Conference on Signal Processing (ICSP)*, pp. 1388–1391, 2016.

[14] S. B. Rieger, J. Pfau, T. Stieglitz, M. Asplund, and J. S. Ordonez, "Concept and development of an electronic framework intended for electrode and surrounding environment characterization in vivo," *Sensors*, vol. 17, no. 1, 2017.

[15] L. Matsiev, "Improving performance and versatility of systems based on single-frequency dft detectors such as ad5933," *Electronics*, vol. 4, no. 1, pp. 1–34, 2015.

[16] K. Chabowski, T. Piasecki, A. Dzierka, and K. Nitsch, "Simple wide frequency range impedance meter based on ad5933 integrated circuit," *Metrology and Measurement Systems*, vol. vol. 22, no. No 1, pp. 13–24, 2015.

[17] J. Hoja and G. Lentka, "A family of new generation miniaturized impedance analyzers for technical object diagnostics," *Metrology and Measurement Systems*, vol. 20, 03 2013.

[18] P. Ibba, M. Crepaldi, G. Cantarella, G. Zini, A. Barcellona, M. Petrelli, B. D. Abera, B. Shkodra, L. Petti, and P. Lugli, "Fruitmeter: An ad5933-based portable impedance analyzer for fruit quality characterization," in *2020 IEEE International Symposium on Circuits and Systems (ISCAS)*, pp. 1–5, 2020.

[19] I. Zhivkov, I. Todorov, M. Hrabal, R. Yordanov, and M. Vala, "Measurement of impedance with computer controlled setup," in *2018 IEEE XXVII International Scientific Conference Electronics - ET*, pp. 1–4, 2018.

[20] X. Chen, S. Li, F. Han, and M. Du, "Research of impedance measurement system based on adaptive feedback calibration method," in *2019 IEEE 3rd Information Technology, Networking, Electronic and Automation Control Conference (ITNEC)*, pp. 1521–1525, 2019.

[21] J. Schneider, M. Schroth, M. Holzhey, T. Blöcher, and W. Stork, "An approach to improve impedance plethysmography on the wrist by using adaptive feedback control," in *2017 IEEE Sensors Applications Symposium (SAS)*, pp. 1–6, 2017.

[22] E. Martianova, S. Aronson, and C. D. Proulx, "Multi-fiber photometry to record neural activity in freely-moving animals," *Journal of Visualized Experiments*, no. 152, 2019.

[23] K. Simone, T. Füzesi, D. Rosenegger, J. S. Bains, and K. Murari, "Open-source, cost-effective system for low-light in vivo fiber photometry," *Neurophotonics*, vol. 5, no. 2, p. 025006, 2018.

[24] H. Dana, Y. Sun, B. Mohar, B. K. Hulse, A. M. Kerlin, J. P. Hasseman, G. Tsegaye, A. Tsang, A. Wong, R. Patel, J. J. Macklin, Y. Chen, A. Konnerth, V. Jayaraman, L. L. Looger, E. R. Schreiter, K. Svoboda, and D. S. Kim, "High-performance calcium sensors for imaging activity in neuronal populations and microcompartments," *Nature Methods*, vol. 16, p. 649–657, July 2019.

[25] "Doric photometry system." `https://neuro.doriclenses.com/collections/fluorescence-mini-cubes/products/fiber-photometry-system-basic`.

[26] M. N. Khiarak, E. Martianova, C. Bories, S. Martel, C. D. Proulx, Y. De Koninck, and B. Gosselin, "A wireless fiber photometry system based on a high-precision cmos biosensor with embedded continuous-time $\sigma\delta$ modulation," *IEEE Transactions on Biomedical Circuits and Systems*, vol. 12, no. 3, pp. 495–509, 2018.

[27] T. Akam and M. E. Walton, "pyphotometry: Open source python based hardware and software for fiber photometry data acquisition," *Scientific Reports*, vol. 9, p. 3521, Mar. 2019.

[28] C. A. Bruno, C. O'Brien, S. Bryant, J. I. Mejaes, D. J. Estrin, C. Pizzano, and D. J. Barker, "Pmat: An open-source software suite for the analysis of fiber photometry data," *Pharmacology Biochemistry and Behavior*, vol. 201, p. 173093, 2021.

[29] "Newport visible femtowatt photoreceiver module." `www.newport.com/f/femtowatt-photoreceivers`.

[30] J. Owens-French, S.-B. Li, M. Francois, R. Leigh Townsend, M. Daniel, H. Soulier, A. Turner, L. de Lecea, H. Münzberg, C. Morrison, and E. Qualls-Creekmore, "Lateral hypothalamic galanin neurons are activated by stress and blunt anxiety-like behavior in mice," *Behavioural Brain Research*, vol. 423, p. 113773, 2022.

[31] A. Sengupta, J. O. Yau, P. Jean-Richard-Dit-Bressel, Y. Liu, E. Z. Millan, J. M. Power, and G. P. McNally, "Basolateral amygdala neurons maintain aversive emotional salience," *Journal of Neuroscience*, vol. 38, no. 12, pp. 3001–3012, 2018.

[32] L. Yang, K. Lee, J. Villagracia, and S. C. Masmanidis, "Open source silicon microprobes for high throughput neural recording," *Journal of Neural Engineering*, vol. 17, p. 016036, Jan. 2020.

[33] M. G. Spring, A. Caccamise, E. A. Panther, B. M. Windsor, K. R. Soni, J. R. McReynolds, D. S. Wheeler, J. R. Mantsch, and R. A. Wheeler, "Chronic stress prevents cortico-accumbens cue encoding and alters conditioned approach," *Journal of Neuroscience*, vol. 41, no. 11, pp. 2428–2436, 2021.

[34] J. Muir, Z. S. Lorsch, C. Ramakrishnan, K. Deisseroth, E. J. Nestler, E. S. Calipari, and R. C. Bagot, "In vivo fiber photometry reveals signature of future stress susceptibility in nucleus accumbens," *Neuropsychopharmacology*, vol. 43, p. 255–263, Jan. 2018.

[35] A. A. Patel, N. McAlinden, K. Mathieson, and S. Sakata, "Simultaneous electrophysiology and fiber photometry in freely behaving mice," *Frontiers in Neuroscience*, vol. 14, 2020.

[36] Z. Liang, Y. Ma, G. D. R. Watson, and N. Zhang, "Simultaneous gcamp6-based fiber photometry and fmri in rats," *Journal of Neuroscience Methods*, vol. 289, p. 31–38, Sept. 2017.

[37] A. Natsubori, T. Tsunematsu, A. Karashima, H. Imamura, N. Kabe, A. Trevisiol, J. Hirrlinger, T. Kodama, T. Sanagi, K. Masamoto, N. Takata, K.-A. Nave, K. Matsui, K. F. Tanaka, and M. Honda, "Intracellular atp levels in mouse cortical excitatory neurons varies with sleep–wake states," *Communications Biology*, vol. 3, p. 1–11, Sept. 2020.

[38] F. Pisano, M. Pisanello, S. J. Lee, J. Lee, E. Maglie, A. Balena, L. Sileo, B. Spagnolo, M. Bianco, M. Hyun, M. De Vittorio, B. L. Sabatini, and F. Pisanello, "Depth-resolved fiber photometry with a single tapered optical fiber implant," *Nature Methods*, vol. 16, p. 1185–1192, Nov. 2019.

[39] J. Jones-Tabah, H. Mohammad, S. Hadj-Youssef, L. E. H. Kim, R. D. Martin, F. Benaliouad, J. C. Tanny, P. B. S. Clarke, and T. E. Hébert, "Dopamine d1 receptor signalling in dyskinetic parkinsonian rats revealed by fiber photometry using fret-based biosensors," *Scientific Reports*, vol. 10, p. 14426, Sept. 2020.

[40] A. A. Legaria, B. A. Matikainen-Ankney, B. Yang, B. Ahanonu, J. A. Licholai, J. G. Parker, and A. V. Kravitz, "Fiber photometry in striatum reflects primarily nonsomatic changes in calcium," *Nature Neuroscience*, vol. 25, p. 1124–1128, Sept. 2022.

[41] F. Acerbi and S. Gundacker, "Understanding and simulating sipms," *Nuclear Instruments and Methods in Physics Research Section A: Accelerators, Spectrometers, Detectors and Associated Equipment*, vol. 926, pp. 16–35, 2019. Silicon Photomultipliers: Technology, Characterisation and Applications.

[42] B. Dolgoshein, V. Balagura, P. Buzhan, M. Danilov, L. Filatov, E. Garutti, M. Groll, A. Ilyin, V. Kantserov, V. Kaplin, A. Karakash, F. Kayumov, S. Klemin, V. Korbel, H. Meyer, R. Mizuk, V. Morgunov, E. Novikov, P. Pakhlov, E. Popova, V. Rusinov, F. Sefkow, E. Tarkovsky, and I. Tikhomirov, "Status report on silicon photomultiplier development and its applications," *Nuclear Instruments and Methods in Physics Research Section A: Accelerators, Spectrometers, Detectors and Associated Equipment*, vol. 563, p. 368–376, July 2006.

[43] P. S. Marrocchesi, M. G. Bagliesi, K. Batkov, G. Bigongiari, M. Y. Kim, T. Lomtadze, P. Maestro, F. Morsani, and R. Zei, "Active control of the gain of a 3mm×3mm silicon photomultiplier," *Nuclear Instruments and Methods in Physics Research Section A: Accelerators, Spectrometers, Detectors and Associated Equipment*, vol. 602, p. 391–395, Apr. 2009.

[44] D. Zhang, X. Li, X. Wen, S. Xiong, Z. An, Y. Xu, X. Sun, R. Qiao, Z. Li, K. Gong, D. Guo, D. Hou, Y. Li, X. Liang, X. Liu, Y. Liu, W. Peng, S. Yang, F. Zhang, X. Zhao, C. Zheng, C. Li, Q. Yi, J. Liu, S. Xiao, C. Cai, and C. Wang, "Gain stabilization and consistency correction approach for multiple sipm-based gamma-ray detectors on gecam," *Nuclear Instruments and Methods in Physics Research Section A: Accelerators, Spectrometers, Detectors and Associated Equipment*, vol. 1027, p. 166222, Mar. 2022.

[45] I. Polák, "Gain stabilization of sipms," in *2016 IEEE Nuclear Science Symposium, Medical Imaging Conference and Room-Temperature Semiconductor Detector Workshop (NSS/MIC/RTSD)*, pp. 1–3, 2016.

[46] F. Sefkow, F. Simon, and o. b. o. t. C. Collaboration, "A highly granular sipm-on-tile calorimeter prototype," *Journal of Physics: Conference Series*, vol. 1162, p. 012012, Jan. 2019.

[47] G. Adamo and A. Busacca, "Time of flight measurements via two lidar systems with sipm and apd," in *2016 AEIT International Annual Conference (AEIT)*, pp. 1–5, 2016.

[48] P. Lecoq and S. Gundacker, "Sipm applications in positron emission tomography: toward ultimate pet time-of-flight resolution," *The European Physical Journal Plus*, vol. 136, p. 292, Mar. 2021.

[49] P. P. Calò, F. Ciciriello, S. Petrignani, and C. Marzocca, "Sipm readout electronics," *Nuclear Instruments and Methods in Physics Research Section A: Accelerators, Spectrometers, Detectors and Associated Equipment*, vol. 926, p. 57–68, May 2019.

[50] H. Xu, M. Perenzoni, N. Massari, A. Gola, A. Ferri, and D. Stoppa, "A 30-ns recovery time, 11.5-nc input charge range, 16-channel read-out asic for pet application," in *ESSCIRC Conference 2015 - 41st European Solid-State Circuits Conference (ESSCIRC)*, pp. 360–363, 2015.

[51] F. Ciciriello, F. Corsi, F. Licciulli, C. Marzocca, G. Matarrese, E. Chesi, E. Nappi, A. Rudge, J. Seguinot, and A. Del Guerra, "BASIC32_ADC, a front-end ASIC for SiPM detectors," in *2013 IEEE Nuclear Science Symposium and Medical Imaging Conference (2013 NSS/MIC)*, pp. 1–6, 2013.

[52] M. Wang, Y. Wang, Q. Cao, L. Wang, J. Kuang, and Y. Xiao, "Comparison of three pre-amplifier circuits for time readout of sipm in tof-pet detectors," in *2019 IEEE International Symposium on Circuits and Systems (ISCAS)*, pp. 1–5, 2019.

[53] A. Siminfar and O. Shoaei, "Development of a passive quenching sipm-based detection system for quantification of real time pcr products based on fluorescence lifetime," *Journal of Instrumentation*, vol. 14, p. P05019, may 2019.

[54] F. Licciulli and C. Marzocca, "An active compensation system for the temperature dependence of sipm gain," *IEEE Transactions on Nuclear Science*, vol. 62, no. 1, pp. 228–235, 2015.

[55] A. Gil, J. Rodríguez, V. Álvarez, J. Díaz, J. Gómez-Cadenas, and D. Lorca, "Programmable power supply system for sipm bias," in *2011 IEEE Nuclear Science Symposium Conference Record*, pp. 787–790, 2011.

[56] R. R. Raylman and A. V. Stolin, "Immersion cooling of silicon photomultipliers (sipm) for nuclear medicine imaging applications," *Radiation Measurements*, vol. 85, p. 111–115, Feb. 2016.

[57] B. Lutz and F. the CMS collaboration), "Upgrade of the cms hadron outer calorimeter with sipm sensors," *Journal of Physics: Conference Series*, vol. 404, p. 012018, dec 2012.

[58] R. R. Raylman, A. Stolin, S. Majewski, and J. Proffitt, "A large area, silicon photomultiplier-based pet detector module," *Nuclear Instruments and Methods in Physics Research Section A: Accelerators, Spectrometers, Detectors and Associated Equipment*, vol. 735, p. 602–609, Jan. 2014.

[59] R. Bencardino and J. E. Eberhardt, "Development of a fast-neutron detector with silicon photomultiplier readout," *IEEE Transactions on Nuclear Science*, vol. 56, no. 3, pp. 1129–1134, 2009.

[60] G. Cozzi, P. Busca, M. Carminati, C. Fiorini, G. L. Montagnani, F. Acerbi, A. Gola, G. Paternoster, C. Piemonte, V. Regazzoni, N. Blasi, F. Camera, and B. Million, "High-resolution gamma-ray spectroscopy with a sipm-based detection module for 1" and 2" labr3:ce readout," *IEEE Transactions on Nuclear Science*, vol. 65, no. 1, pp. 645–655, 2018.

[61] P. Dorosz, M. Baszczyk, S. Glab, W. Kucewicz, L. Mik, and M. Sapor, "Silicon photomultiplier's gain stabilization by bias correction for compensation of the temperature fluctuations," *Nuclear Instruments and Methods in Physics Research Section A: Accelerators, Spectrometers, Detectors and Associated Equipment*, vol. 718, p. 202–204, Aug. 2013.

[62] G. Eigen, "Gain stabilization of sipms and afterpulsing," *Journal of Physics: Conference Series*, vol. 1162, p. 012013, Jan. 2019.

[63] P. Gong, Z. Han, L. Gao, P. Wang, J. Zhang, and X. Tang, "Development of a sipm-based csi(tl) spectrometer with gain stabilization designs for rapid temperature variations," *Nuclear Instruments and Methods in Physics Research Section A: Accelerators, Spectrometers, Detectors and Associated Equipment*, vol. 927, p. 301–305, May 2019.

[64] "Chroma spectraviewer." `https://www.chroma.com/spectra-viewer?fluorochromes=27289`.

[65] M. Namazi, G. Peringod, A. Bisht, J. Bains, G. R. Gordon, and K. Murari, "Silicon photomultiplier-based low-light in vivo fiber photometry," in *2023 IEEE Biomedical Circuits and Systems Conference (BioCAS)*, p. in press, 2023.

[66] M. Sekar, R. Sriramprabha, P. K. Sekhar, S. Bhansali, N. Ponpandian, M. Pandiaraj, and C. Viswanathan, "Review—towards wearable sensor platforms for the electrochemical detection of cortisol," *Journal of The Electrochemical Society*, vol. 167, p. 067508, mar 2020.

[67] P. Batista and A. Pereira, "Biomarkers in neurodegenerative diseases: Cortisol," *Journal of Molecular Biomarkers & Diagnosis*, vol. 07, 01 2016.

[68] N. M. Soares, G. M. Pereira, V. Altmann, R. M. M. de Almeida, and C. R. M. Rieder, "Cortisol levels, motor, cognitive and behavioral symptoms in parkinson's disease: a systematic review," *Journal of Neural Transmission*, vol. 126, p. 219–232, Mar. 2019.

[69] A. J. Bard and L. R. Faulkner, *Electrochemical methods: fundamentals and applications*. New York: Wiley, 2nd ed ed., 2001.

[70] C. I. L. Justino, A. C. Freitas, R. Pereira, A. C. Duarte, and T. A. P. Rocha Santos, "Recent developments in recognition elements for chemical sensors and biosensors," *TrAC Trends in Analytical Chemistry*, vol. 68, p. 2–17, May 2015.

[71] A. C. Lazanas and M. I. Prodromidis, "Electrochemical impedance spectroscopy - a tutorial," *ACS Measurement Science Au*, vol. 3, p. 162–193, June 2023.

[72] "Palmsens knowledge base article - purpose of a sense lead." `www.palmsens.com/knowledgebase-article/purpose-of-a-sense-lead`.

[73] A. A. A. Al-Ali, *Design and Implementation of a Magnitude Only Bio-Impedance Analyzer*. PhD thesis, University of Calgary, Apr. 2018.

[74] F. Mollarasouli, S. Kurbanoglu, and S. A. Ozkan, "The role of electrochemical immunosensors in clinical analysis," *Biosensors*, vol. 9, p. 86, Sept. 2019.

[75] M. Zea, F. G. Bellagambi, H. Ben Halima, N. Zine, N. Jaffrezic-Renault, R. Villa, G. Gabriel, and A. Errachid, "Electrochemical sensors for cortisol detections: Almost there," *TrAC Trends in Analytical Chemistry*, vol. 132, p. 116058, Nov. 2020.

[76] X. Weng, Z. Fu, C. Zhang, W. Jiang, and H. Jiang, "A portable 3d microfluidic origami biosensor for cortisol detection in human sweat," *Analytical Chemistry*, vol. 94, p. 3526–3534, Mar. 2022.

[77] J. Shin, S. Kim, T. Yoon, C. Joo, and H.-I. Jung, "Smart fatigue phone: Real-time estimation of driver fatigue using smartphone-based cortisol detection," *Biosensors and Bioelectronics*, vol. 136, p. 106–111, July 2019.

[78] Y. Kim, J. Yang, H. Hur, S. Oh, and H. H. Lee, "Highly sensitive colorimetric assay of cortisol using cortisol antibody and aptamer sandwich assay," *Biosensors*, vol. 11, p. 163, May 2021.

[79] E. Tu, P. Pearlmutter, M. Tiangco, G. Derose, L. Begdache, and A. Koh, "Comparison of colorimetric analyses to determine cortisol in human sweat," *ACS Omega*, vol. 5, p. 8211–8218, Apr. 2020.

[80] S. Jo, W. Lee, J. Park, W. Kim, W. Kim, G. Lee, H.-J. Lee, J. Hong, and J. Park, "Localized surface plasmon resonance aptasensor for the highly sensitive direct detection of cortisol in human saliva," *Sensors and Actuators B: Chemical*, vol. 304, p. 127424, Feb. 2020.

[81] S. K. Arya, G. Chornokur, M. Venugopal, and S. Bhansali, "Dithiobis(succinimidyl propionate) modified gold microarray electrode based electrochemical immunosensor for ultrasensitive detection of cortisol," *Biosensors and Bioelectronics*, vol. 25, p. 2296–2301, June 2010.

[82] B. J. Sanghavi, J. A. Moore, J. L. Chávez, J. A. Hagen, N. Kelley-Loughnane, C.-F. Chou, and N. S. Swami, "Aptamer-functionalized nanoparticles for surface immobilization-free electrochemical detection of cortisol in a microfluidic device," *Biosensors and Bioelectronics*, vol. 78, p. 244–252, Apr. 2016.

[83] D. Kinnamon, R. Ghanta, K.-C. Lin, S. Muthukumar, and S. Prasad, "Portable biosensor for monitoring cortisol in low-volume perspired human sweat," *Scientific Reports*, vol. 7, p. 13312, Oct. 2017.

[84] H. D. Ertuğrul Uygun, Z. O. Uygun, E. Canbay, F. Giŕgiń Sağın, and E. Sezer, "Non-invasive cortisol detection in saliva by using molecularly cortisol imprinted fullerene-acrylamide modified screen printed electrodes," *Talanta*, vol. 206, p. 120225, Jan. 2020.

[85] B. A. Cardinell, M. L. Spano, and J. L. Belle, "Toward a label-free electrochemical impedance immunosensor design for quantifying cortisol in tears," *Critical Reviews™ in Biomedical Engineering*, vol. 47, no. 3, 2019.

[86] S. Upasham, A. Tanak, B. Jagannath, and S. Prasad, "Development of ultra-low volume, multi-bio fluid, cortisol sensing platform," *Scientific Reports*, vol. 8, p. 16745, Nov. 2018.

[87] P. Rice, S. Upasham, B. Jagannath, R. Manuel, M. Pali, and S. Prasad, "Cortiwatch: watch-based cortisol tracker," *Future Science OA*, vol. 5, no. 9, p. FSO416, 2019.

[88] R. M. Torrente-Rodríguez, J. Tu, Y. Yang, J. Min, M. Wang, Y. Song, Y. Yu, C. Xu, C. Ye, W. W. IsHak, and W. Gao, "Investigation of cortisol dynamics in human sweat using a graphene-based wireless mhealth system," *Matter*, vol. 2, p. 921–937, Apr. 2020.

[89] N. K. M. Churcher, C. Greyling, S. Upasham, K.-C. Lin, P. Rice, M. Pali, J. Spiro, and S. Prasad, "Aptastrensor (aptamer-based sensor for stress monitoring): The interrelationship between npy and cortisol towards chronic disease monitoring," *Biosensors and Bioelectronics: X*, vol. 10, p. 100145, May 2022.

[90] B. Wang, C. Zhao, Z. Wang, K.-A. Yang, X. Cheng, W. Liu, W. Yu, S. Lin, Y. Zhao, K. M. Cheung, H. Lin, H. Hojaiji, P. S. Weiss, M. N. Stojanović, A. J. Tomiyama, A. M. Andrews, and S. Emaminejad, "Wearable aptamer-field-effect transistor sensing system for noninvasive cortisol monitoring," *Science Advances*, vol. 8, p. eabk0967, Jan. 2022.

[91] S. Shajari, R. Salahandish, A. Zare, M. Hassani, S. Moossavi, E. Munro, R. Rashid, D. Rosenegger, J. S. Bains, and A. Sanati Nezhad, "Microsweat: A wearable microfluidic patch for noninvasive and reliable sweat collection enables human stress monitoring," *Advanced Science*, vol. 10, p. 2204171, Mar. 2023.

[92] R. Salahandish, F. Haghayegh, S. Khetani, M. Hassani, and A. S. Nezhad, "Immuno-affinity potent strip with pre-embedded intermixed pedot:pss conductive polymers and graphene nanosheets for bio-ready electrochemical biosensing of central nervous system injury biomarkers," *ACS Applied Materials & Interfaces*, vol. 14, p. 28651–28662, June 2022.

[93] "Texas Instruments LMV55x amplifier datasheet." `https://www.ti.com/lit/ds/symlink/lmv551.pdf`.

[94] A. Barhoum and R. J. Forster, "Label-free electrochemical immunosensor for picomolar detection of the cervical cancer biomarker mcm5," *Analytica Chimica Acta*, vol. 1225, p. 340226, Sept. 2022.

[95] A. Kaushik, A. Yndart, S. Kumar, R. D. Jayant, A. Vashist, A. N. Brown, C.-Z. Li, and M. Nair, "A sensitive electrochemical immunosensor for label-free detection of zika-virus protein," *Scientific Reports*, vol. 8, p. 9700, June 2018.

[96] A. Pal, S. Biswas, S. P. O Kare, P. Biswas, S. K. Jana, S. Das, and K. Chaudhury, "Development of an impedimetric immunosensor for machine learning-based detection of endometriosis: A proof of concept," *Sensors and Actuators B: Chemical*, vol. 346, p. 130460, 2021.